Dissertation

Observational Studies on Turbulent Convection in the Solar Photosphere

（太陽光球における乱対流の観測的研究）

総合研究大学院大学物理科学研究科天文科学専攻

Ryohtaroh Ishikawa

石川　遼太郎

2022

令和4年

Abstract

The dynamics in the solar photosphere are governed by thermally driven convection. This produces cellular patterns termed granules that are observed in visible-light continuum images. Granules with hot rising flows are surrounded by darker and cooler intergranular lanes. Granules repeat birth and death in a finite lifetime, highlighting their dynamic nature. These dynamics of the granulation inherently create small-scale flow structures that are smaller than the typical size of granules. Since the magnetic flux is concentrated in regions smaller than the granular scale, the interaction between the magnetic field and gas motion occurs on such small scales. Such interaction can amplify the magnetic fields and produce the Poynting flux upward. Therefore, it is important to evaluate not only the magnetic fields but also the 3-dimensional velocity fields on scales smaller than the granules in the solar photosphere.

We can obtain the line-of-sight (LOS) component of the flow velocities by a spectroscopic observation via the Doppler effect. Conversely, to date, there are no direct methods for observing the components perpendicular to the LOS. These components correspond to the horizontal velocity on the solar surface in disk center observations. The most commonly used method for estimating the horizontal velocity field is local correlation tracking (LCT). Although the LCT technique can evaluate the horizontal velocity with good accuracy on a larger scale, its accuracy on a scale smaller than granules is limited. In Chapter 2, we develop a convolutional neural network model with a multi-scale deep learning architecture. The method consists of multiple convolutional kernels with various sizes of receptive fields. Fur-

thermore, we introduce a novel coherence spectrum to assess the horizontal velocity fields that were derived at each spatial scale. The multi-scale deep learning method successfully predicts the horizontal velocities for each convection simulation in terms of the global correlation coefficient, which is often used for evaluating the prediction accuracy of the methods. The coherence spectrum reveals the strong dependence of the correlation coefficients on the spatial scales. Although the coherence spectra are higher than 0.9 for large-scale structures, they drastically decrease to less than 0.3 for small-scale structures wherein the global correlation coefficient indicates a high value of approximately 0.95. By comparing the results of the three convection simulations, we determine that this decrease in the coherence spectra occurs around the energy injection scales, which are characterized by the peak in the power spectra of the vertical velocities.

Spectral line profiles have information of the LOS velocity on scales smaller than the spatial resolution. In Chapter 3, we perform bisector analysis using spectral line profiles of the Fe I 6301.5 Å line obtained with the spectropolarimeter of the solar optical telescope onboard the Hinode satellite (Hinode-SOT/SP) and study how both the spectral line widths and the bisector velocities are related with the granulation. We confirm that the LOS gradient of Doppler velocity causes the spectral line broadening, and there exist two types of velocity gradients: faster downward and upward flows in the lower photosphere. The former ones are preferentially seen in the intergranular downflow lanes, and some of them are associated with strong concentrations of magnetic fields. The latter, on the other hand, has no clear correlation with magnetic fields. By analyzing the temporal evolutions of line profiles, we discover that the line broadening and the velocity gradient with faster upward flows appear during the fading process of granules. The spectral line becomes so wide that the increase of the line widths cannot be explained only by the velocity gradients.

There are multiple possibilities, such as temperature and velocity gradients, in addition to the micro-turbulence to cause the line broadening. It is difficult to investigate the mechanism of the line broadening only by the bisector analysis. In

Chapter 4, we conduct spectral line inversion, which enables us to infer the height dependence of the temperature and the Doppler velocity by fitting the observed spectra by calculating radiative transfer. We find two possible scenarios to explain the observed spectral line broadening in fading granules: one is microturbulence of about 1 km/s and the other is complicated gradients of Doppler velocity along the LOS. Although the height profile of temperature and vertical velocity estimated with and without microturbulence are largely different in fading granules, it is difficult to distinguish them only with Fe I lines observed with Hinode-SOT/SP. We also analyze the spectral line profiles synthesized with 3D MHD simulation data. Spectral line broadening in fading granules is also seen in the synthesized line profiles. We find that this line broadening is caused by the turbulent flows in the lower photosphere associated with the fading process of a granule. The turbulent motions are driven by the shear flow structures located at the boundary between the granule and intergranular lanes. These results show the importance of the spectral line widths as a tracer of small-scale velocity fields.

Acknowledgement

I would like to express the deepest appreciation to Dr. Y. Katsukawa, for leading me to work in solar physics and providing me the opportunity to make a research in National Astronomical Observatory of Japan. Without his persistent help and insightful discussions, this thesis would not have been possible.

I would like to express my deepest thank to Dr. M. Nakata in National Institute for Fusion Science, for his constructive comments and fruitful discussion. My sincere thanks also go to Prof. K. Nagaoka and Dr. T. Kobayashi for their kind support on my stay in NIFS and encouraging my research.

My sincere thanks also go to Dr. M. Kubo and all other staffs in solar science observatory in NAOJ. Special thanks are extended to M. Shoda, T. Oba, Y. Kawabata, T. Matsumoto, Y. Ishizuka, A. Moritsuka, K. Fukumitsu, and S. Ishigami for their support on my research and academic life in NAOJ. I also thank to Y. Kasagi, S. Nakano, R. Kashiwagi, T. Masai, and all the members in the Department of Astronomical Science, School of Physical Sciences, The Graduate University for Advanced Studies, SOKENDAI.

This work is supported by the NINS program for cross-disciplinary study on Turbulence, Transport, and Heating Dynamics in the Laboratory and Astrophysical Plasmas: "SoLaBo-X" (Grant Numbers 01321802 and 01311904) and by JSPS KAKENHI Grant Numbers JP18H05234, JP19J20294, and 20KK0072. Hinode is a Japanese mission developed and launched by ISAS/JAXA, collaborating with NAOJ as a domestic partner, NASA and STFC as international partners. Support for the post-launch operation is provided by JAXA and NAOJ (Japan), STFC (UK),

NASA, ESA, and NSC (Norway).

Finally, I would like to thank to my family for their continuous and cordial supports over the years.

Contents

Chapter 1

Introduction

The Sun is the unique star that can be spatially resolved and affects the geomagnetic environment and is the brightest object for us. Today, the Sun is known as a typical main-sequence star of class G2V and is used for the standard model of the main sequence stars when we are to explain the spectral line profiles of stars. In addition, high spatial, temporal, and spectral resolutions of recent instruments enable us to perform detailed observations of the dynamics of solar plasma and have given us a lot of insights into plasma physics. However, the dynamics in the solar atmosphere and the association with the emergent spectral line profiles still have a lot of puzzles to be solved. In this chapter, we introduce previous studies and issues on the solar atmosphere and spectral line formation.

1.1 Solar Atmosphere

The solar atmosphere is strongly stratified. Figure 1.1 shows a model atmosphere of the Sun. Here, the photospheric surface is defined as the iso-τ surface of $\tau_{500} = 1$, where τ_{500} represents the optical depth at 500 nm visible light. The density decreases exponentially as the height increases. The pressure scale heights are 150 km at the solar surface and a few 10,000 km in the corona. The temperature at the photospheric surface is about 6400 K and it decreases to 4400 K in the

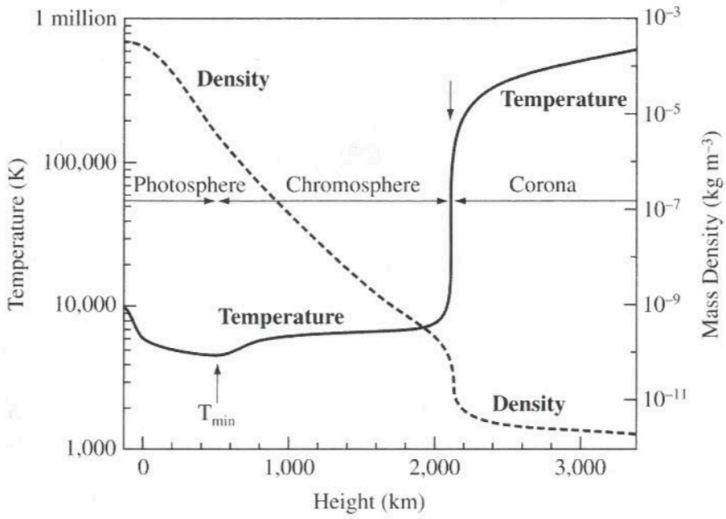

Figure 1.1: The solar atmospheric structure of the VAL3C model (Vernazza, Avrett, and Loeser 1981)

upper photosphere. This temperature minimum layer is the boundary between the photosphere and the chromosphere. The temperature reaches about 10,000 K at the top of the chromosphere and 1 million K at the bottom of the corona. Since the Sun creates energy in the core via the nuclear fusion process, the energy is transported from the interior to the corona through the photosphere. Therefore, it is not obvious how the energy is transported into the hot corona from the cool photosphere. Although this problem is known since the coronal emission spectra of forbidden lines of highly ionized iron are identified in the 20th century (Grotrian, 1939; Edlén, 1943), it is still one of the most important issues to understand the solar atmosphere.

Today, it is widely accepted that magnetic fields play an important role in maintaining the corona (Klimchuk, 2006). The magnetic fields are ubiquitous in the solar atmosphere. Magnetic fluxes are concentrated in localized regions in the photosphere (Lites *et al.*, 2008; Bellot Rubio and Orozco Suárez, 2019), and they expand entire the corona due to the rapid density decrease of the ambient plasma. Since the

photosphere is dominated by the convective motions (see Section 1.2), the small-scale magnetic flux always interacts with the convective motions. This mechanical energy near the solar surface is the only available energy source to heat the corona. MHD wave is one of the prevailing processes to transport energy (Van Doorsselaere *et al.* 2020 and references therein). Thanks to the improvement of the spatial, temporal, and spectral resolution of instruments, MHD waves are observed in the solar photosphere (Dorotovič, Erdélyi, and Karlovský 2008; Fujimura and Tsuneta 2009; Morton *et al.* 2011), in the chromosphere (De Pontieu *et al.* 2007; Jess *et al.* 2009; Kanoh, Shimizu, and Imada 2016), and in the corona (Tomczyk *et al.* 2007), which subsequently dissipate and generate heat in the corona (Antolin and Shibata 2010; Okamoto *et al.* 2015; Antolin *et al.* 2015).

High-frequency waves have been observed in spicules (Okamoto and De Pontieu, 2011; Shetye *et al.*, 2021). Srivastava *et al.* (2017) observed high-frequency torsional waves in chromospheric jet-like structures and performed an MHD simulation showing that the waves contain enough energy for coronal heating. The driver of MHD waves should be the convective motions. The low-frequency waves are generated by random-walk-like motions induced by granular flows. On the other hand, high-frequency waves and torsional modes can be driven by small-scale turbulent motions in the photosphere. Vortex motion has been reported in the granulation (Brandt *et al.* 1988), in the magnetic bright points (Bonet *et al.* 2008), and in the chromosphere (Wedemeyer-Böhm and Rouppe van der Voort 2009; Wedemeyer-Böhm 2010). There are several MHD simulations trying to reproduce the vortex motion in the photosphere (Stein and Nordlund 1998; Shelyag *et al.* 2011) and in the chromosphere (Iijima and Yokoyama 2017; Yadav, Cameron, and Solanki 2021).

1.2 Solar Surface Convection

1.2.1 Granulation

The photosphere is a weakly-ionized thin layer of about 500 km in height in the Sun. Although the photosphere is convectively stable because of its transparency to the visible lights, dynamics is predominated by convective motions penetrating from convectively unstable layer just below the photosphere. Figure 1.2 shows the solar photosphere observed by solar optical telescope aboard Hinode satellite. The photospheric surface is covered by millions of bright cells and surrounding dark lanes.

The bright cells and the surrounding dark lanes are termed granules and intergranular lanes, respectively. Granules are thought to be convective cells. The bright center of a granule consists of hot plumes ascending from the convection zone. These hot plumes are cooled radiatively near the solar surface, increasing their density. Consequently, the radiatively cooled plasma descends with gravity in the intergranular lanes.

The upward and downward velocities have been religiously investigated by many authors (e.g. Nesis *et al.* 2001; Hirzberger 2002; Janssen and Cauzzi 2006; Jin, Wang, and Zhao 2009; Yu *et al.* 2011; Oba *et al.* 2017) with optical telescopes with high spatial resolutions. Oba *et al.* (2017) derived the root-mean-square velocity of the convective flows of 1.1 km/s, by eliminating the effect of instrumental image degradation by applying a deconvolution technique to spectroscopic data obtained with the Hinode Solar Optical Telescope (Kosugi *et al.*, 2007; Tsuneta *et al.*, 2008). This result shows that the typical velocity on the granular scale ($\sim$ 1 Mm) is 1.1 km/s. Oba, Iida, and Shimizu (2017) found that the upward velocity at the center of granules decreases from 0.65 km/s to 0.40 km/s as it ascends and the downward velocity at the intergranular lane increases from 0.30 km/s to 0.50 km/s as it descends to the lower layer, which indicates that radiative cooling and/or gas pressure gradient let the photosphere achieve the convectively unstable condition and control the photospheric dynamics.

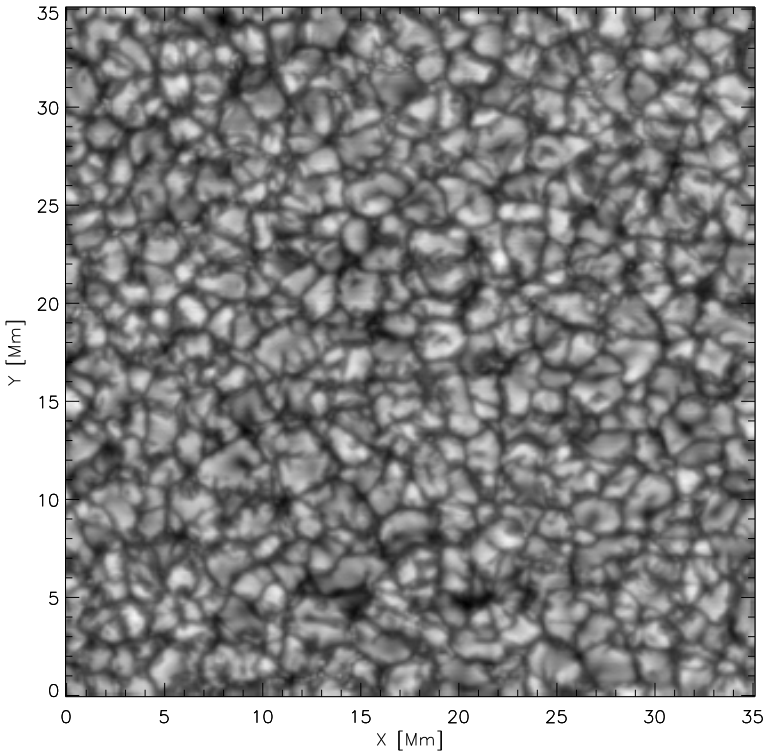

Figure 1.2: Image of granulation in the continuum of 6301 Å obtained with the Hinode-SOT/SP.

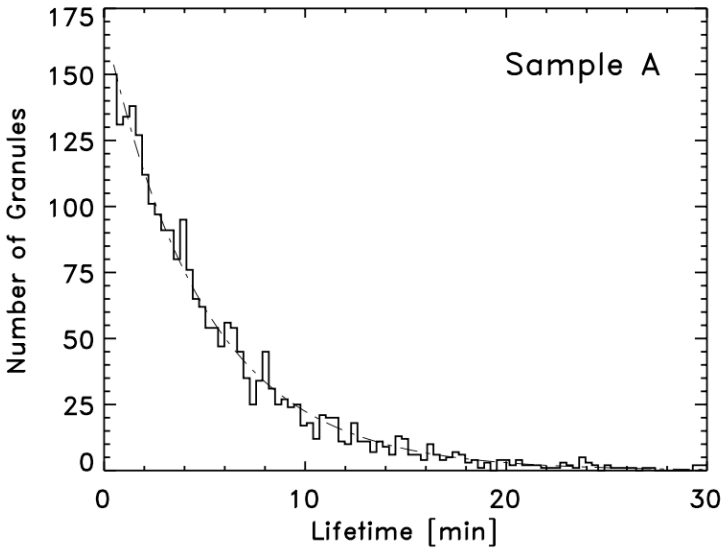

Figure 1.3: The histogram of lifetimes of granules investigated by Hirzberger *et al.* (1999). The histogram is made by an automatic detection of granules, whereas the manual detection also show the same result.

1.2.2 Tenporal and spatial scales of granulation

The granulation is not static but so dynamic that granules repeat birth and death within finite lifetimes. The probability density function of the lifetimes of granules is known to give a good fit to an exponential law:

$$N(t) \propto \exp\left[-\frac{t}{t_0}\right] \tag{1.1}$$

and the average t_0 is estimated 5 minutes (Figure 1.3; Hirzberger *et al.* 1999). Here, the end of the lifetime of a granule is defined by its fragmentation, coalescence with another granule, and fading out (dissolution to the background). The death process of 52.9% of granules is merging and 31.2% of granules end their lifetimes via fragmentation. 15.9% of granules fade away when they end their lives (Hirzberger *et al.*, 1999). By analyzing recent observational data by SUNRISE balloon-borne telescope, Lemmerer *et al.* (2017) found that the 17% of granules disappear without

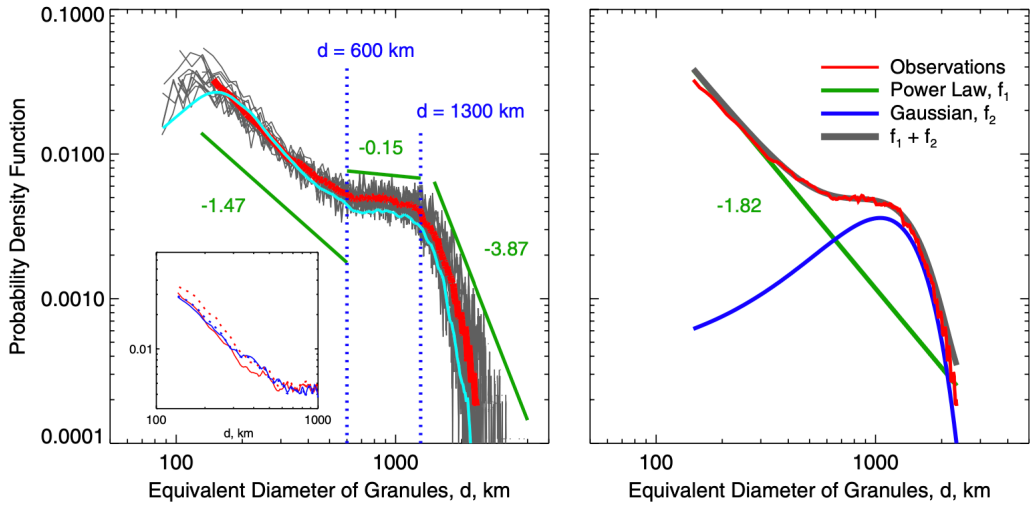

Figure 1.4: Left: The probability density function of the size of the observed granules. The granule detection is done with 15 different conditions (grey lines) and the average of them is shown in red color. Right: The fitting result of the average PDF with a power law component and a Gaussian component. The power law index is -1.82. The mode of the Gaussian is 1050 km and the standard deviation is 480 km (Abramenko *et al.* 2012).

fragmentation. These granules have an average diameter of about 500 km. Other observed granules die via the fragmentation process. They found that larger granules are likely to fragment into a larger number of granules. Note that Lemmerer *et al.* (2017) defined the death process as fragmentation and fading out: granules survive the merging process.

Although the various sizes of granules are observed as shown in Figure 1.2, granules are thought to have a typical spatial scale of ∼1000 km (Bray, Loughhead, and Durrant, 1984; Hirzberger *et al.*, 1999), while the typical width of intergranular lane is ∼300 km (Bray, Loughhead, and Durrant, 1984). The spatial scale of granules may reflect the energy injection scales, since the energy transport is done by the convective motions of ascending hot plumes and descending cool plumes. Theoretically,

the energy injection scale is thought to be related to the pressure scale height near the solar surface (Bolgiano, 1959; Obukhov, 1959; Rincon, 2007), since the spatial scale of the density fluctuation reflects the scale height. The power spectrum analysis can determine the energy injection scale and it is comparable to the granular scale (Rieutord *et al.*, 2010; Katsukawa and Orozco Suárez, 2012).

Figure 1.4 shows the probability density function of the size of granules investigated by Abramenko *et al.* (2012) with New Solar Telescope at Big Bear Solar Observatory. They discovered two populations of granules: one follows a power-law distribution and the other a Gaussian with an average diameter of about 1 Mm, which is also detected by (Lemmerer *et al.*, 2017) with the SUNRISE observation. The power-law component covers half of the total granular area, and they are preferentially confined in broad intergranular lanes, forming clusters and chains of them. The power-law component can be associated with the turbulent plasma flows in the intergranular lanes, where the intensity of turbulence is enhanced. However, due to their small spatial scales, detecting the magnetic fields and the velocity fields is difficult.

The power spectrum analyses have been performed for the observational data. Katsukawa and Orozco Suárez (2012) found that the power spectra of kinetic energy depend on the magnetic flux, which indicates the strong coupling between the magnetic fields and convective motions especially in strongly magnetized regions such as plage region. The power law indices of power spectra of vertical velocity on scales smaller than 1 Mm are down to -3 (Rieutord *et al.*, 2010) or -17/3 (Yelles Chaouche, Moreno-Insertis, and Bonet, 2014) in quiet region, while the power spectra of magnetic energy has shallower slope (Katsukawa and Orozco Suárez, 2012; Danilovic, van Noort, and Rempel, 2016). These difference of slopes are consistent with the small-scale dynamo simulations. On the other hand, Goode *et al.* (2010) found the inverse results: steeper (or similar) slope of the magnetic energy compared to the kinetic energy. They concluded that the equipartition between the kinetic and magnetic energy is achieved in the wide range of spatial scales down to sub-granular scales. Danilovic, van Noort, and Rempel (2016) compared the power spectra with

the numerical simulation (Rempel, 2014) and the observation considering the radiative transfer and the instrument resolution, demonstrating the good agreement of them on scales larger than the spatial resolution of about 200 km that is comparable to the widths of intergranular lanes. Because of the limitation of the spatial resolution of current instruments, it is hard to evaluate the power spectra on the intergranular scales. Therefore, it is still unclear how amount of kinetic and magnetic energy resides on the scales smaller or comparable to the widths of intergranular lanes.

1.2.3 Granulation for maintenance and amplification of magnetic fields

The ubiquitous magnetic fields on the solar surface are found with recent high-resolution observations (Lites *et al.*, 2008; Ishikawa *et al.*, 2008). These magnetic fields are known to be independent of the 11-year solar cycle (Trujillo Bueno, Shchukina, and Asensio Ramos, 2004). One prevailing theory to maintain these ubiquitous fields is small-scale dynamo process, by which the energy transport from the kinetic energy into the magnetic energy happens via the turbulent interactions on scales smaller than the granulation (Petrovay and Szakaly, 1993). Danilovic, Schüssler, and Solanki (2010) compared the observed and the simulated magnetic fields and found that there exists a descrepancy of average unsigned magnetic field strength by a factor of 2 or 3, which was resolved by Rempel (2014) with including the interaction between the photosphere and deep convection zone. Rempel (2014) investigated the power spectra of the kinetic and magnetic energy with high-resolution MHD simulations and found the power spectrum of kinetic energy has steep slope on the scales of about 200 km that is comparable to the width of intergranular lanes. Due to the efficient small-scale dynamo process, the magnetic fields have large energy than the kinetic energy on scales smaller than granular sizes, suppressing the small-scale flows of the turbulent convection. This suppression is also thought to be important to create the large-scale magnetic structures that is related to the 11-year solar cycle

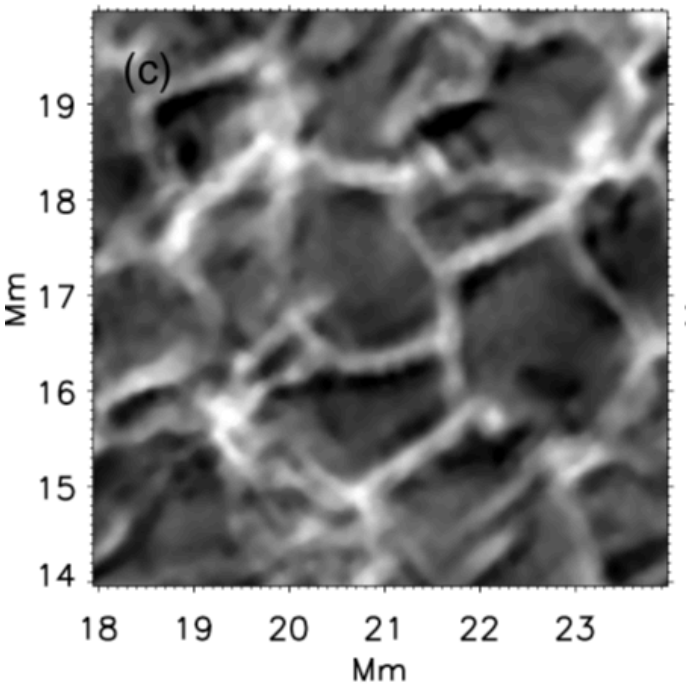

Figure 1.5: The spatial distribution of spectral line widths obtained by SUNRISE/IMaX (Khomenko *et al.* 2010). Spectral line profiles with large FWHM are observed preferentially in intergranular lanes (white lanes) and the those with small FWHM in granules (dark region).

(Hotta, Rempel, and Yokoyama, 2016).

1.2.4 Observation of small-scale structures

The small-scale kinetic and magnetic structures are difficult to be observed when they have significant power at the spatial scale close to the instrument resolution. When we observe polarization signals due to the classical Zeeman effect, the positive and negative Stokes signals cancel out each other. This leads underestimate the magnetic energy on small scales. However, the small-scale magnetic fields could be inferred via the Hanle effect (Trujillo Bueno, Shchukina, and Asensio Ramos,

2004; Trujillo Bueno, Štěpán, and Casini, 2011; Ishikawa *et al.*, 2017), which can overcome this difficulty by observing the modulation of scattering polarization due to magnetic fields. The estimation of LOS velocity fields also suffers from the same problem: redshifts and blueshifts that coexist in a spatial resolution and integration along LOS tend to be cancelled out each other, and cause reduction of net Doppler velocities thus observed.

Since it is still difficult to observe the small-scale velocity fields, there remains a basic question: how turbulent is the granulation? The Reynolds number in the photosphere is approximately 10^{12} (Hirzberger, 2002), which indicates that the granular flows can be highly turbulent. However, Nordlund *et al.* (1997) claimed that the granular flows in the photosphere are laminar due to the strong stratification: the expansion of upflows makes the flows laminar. They argued that only in the downflow regions the flows can be turbulent but most of these turbulent flows cannot be observed since they are rapidly transported below the visible surface (Rast, 1998). The power-law behavior of the power spectra of vertical velocity fields may be an indication of the turbulent nature of the photosphere. However, the power-law indices are not well determined as summarized in the previous section. To clarify the turbulent nature of the photosphere, it is necessary to reveal the physical process that drives turbulent motions. The spatial distributions and the temporal evolutions of small-scale velocity fields may have important signatures of turbulence, while the power spectrum analyses cannot provide them.

One possible approach is observing the spectral line broadening. The spectral line width can be affected by the velocity variation on small scales via the microturbulence term or the macroturbulence effect. In addition, we can investigate both the spatial and temporal variations of line widths. The spatial variations of the full width at half maximum (FWHM) of photospheric spectra are investigated by Holweger and Kneer (1989) and Nesis *et al.* (1992). They found that the FWHM is larger in intergranular lanes than in granules, which is confirmed by recent observations by Khomenko *et al.* (2010) as shown in Figure 1.5. Before I summarize the previous studies on the line broadening of photospheric spectra, I describe the

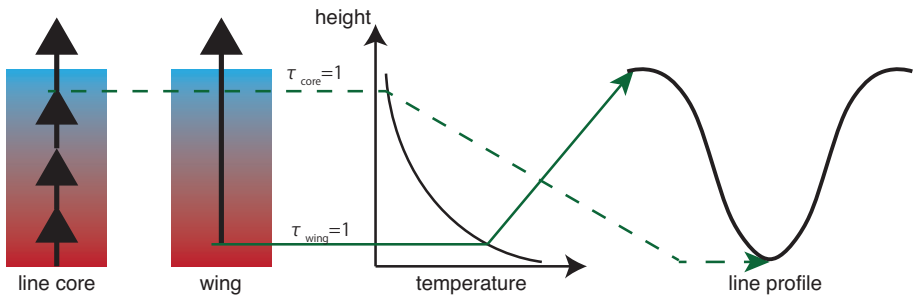

Figure 1.6: A schematic illustration of the formation of photospheric lines. The line core is optically thicker than the wing: the emergent intensity at the line core comes from the upper photosphere, while that at wing from the lower photosphere.

spectral line formation in the next section.

1.3 Radiative Transfer and Spectral Line Formation

In this thesis, we focus on the spectral line profiles especially the line broadening and the asymmetry, because the turbulent motions broaden the spectral profiles and the velocity gradient causes asymmetry. Here we describe the basic theory of spectral line broadening and asymmetry, and the importance of analyzing the detailed profile.

1.3.1 Formation of photospheric lines

The radiative transfer equation of unpolarized light under the local thermodynamic equilibrium (LTE) condition is

$$\frac{dI_\lambda}{d\tau_c} = (1 + \eta_\lambda)\,(I_\lambda - S_\lambda), \tag{1.2}$$

where τ_c is the optical depth of the continuum and η_λ is the ratio between the absorption coefficients of the line and the continuum. The optical depth at each

wavelength is defined as an integration along the line-of-sight (LOS) direction:

$$\tau_\lambda(s) = -\int_\infty^s \alpha_c(1+\eta_\lambda)ds' = -\int_\infty^s \frac{ds'}{\ell_\lambda(s')}, \tag{1.3}$$

where α_c is the absorption coefficient of the continuum and ℓ_λ represents the photon mean free path at a wavelength λ. The ratio η_λ is written with the Voigt function as

$$\eta_\lambda = \eta_0 H(a,u) \tag{1.4}$$

$$= \eta_0 \frac{a}{\pi}\int_{-\infty}^{\infty} \frac{\exp[-y^2]}{a^2+(u-y)^2}dy. \tag{1.5}$$

Here, η_0 denotes a constant value depending on the oscillator strength of the line and the absorption coefficient of continuum. The wavelength $u = (\lambda - \lambda_0)/\lambda_D$ is normalized by the Doppler width

$$\lambda_D \equiv \frac{\lambda_0}{c}\sqrt{\frac{2k_BT}{m} + v_{\rm mic}^2}, \tag{1.6}$$

where λ_0 is the center wavelength at the rest frame and c, k_B, T, m, $v_{\rm mic}$ are the speed of light, the Boltzman constant, temperature, mass of the atom, and the microturbulent velocity, respectively. The Voigt function $H(a,u)$ is defined as the convolution of Gaussian function and Lorentz function, including the thermal broadening and the microturbulent broadening as a Gaussian term and the natural broadening and the pressure broadening as a Lorentz profile. The central wavelength could be shifted by the LOS velocity ($\delta\lambda_0 = \frac{v_{\rm LOS}}{c}\lambda_0$).

Given the LTE condition is satisfied, the emergent intensity at a wavelength reflects the temperature at the layer where the optical depth of the wavelength is unity. As shown above, the absorption coefficient is larger at the line core ($u \sim 0$) than that at the line wing ($|u| >> 1$) due to the difference of η_λ. Therefore, the emergent intensity at the line core comes from the upper photosphere, while that at the wing from the lower photosphere. Moreover, it is known that the temperature decreases as it goes higher in the photosphere. Consequently, the spectral lines formed in the photosphere appear as absorption lines (Figure 1.6).

1.3.2 Microturbulence

The microturbulent velocity $v_{\rm mic}$ is an artificial parameter to describe the small-scale velocity variation, by assuming the probability density function of this small-scale velocity obeys a Gaussian distribution. Under this assumption, similar to the thermal broadening, the small-scale turbulent velocities broaden the spectral line profile via the Doppler effect as shown in Equation (1.6). The microturbulence term was originally introduced to explain the large equivalent widths that cannot be explained only by the thermal broadening.

it is widely accepted that the microturbulence reflects flow fields on scales smaller than the photon mean free path (e.g. Hubeny and Mihalas 2014), although it is still not clear what process determines the microturbulence term. The height from which photons at a specific wavelength come has a certain range that is relevant to the photon mean free path, which determines the resolution along the LOS of observations. Only by analyzing one or a few spectral lines, we cannot resolve the LOS variation of LOS velocity on scales smaller than the photon mean free path, and the velocity variation should be modeled by a microturbulence term. The photon mean free path near the solar photospheric surface is comparable to the density scale height of about 130 km (Judge *et al.*, 2015). On the other hand, the LOS gradient of LOS velocity on scales much larger than the mean free path can be resolved, since it can cause asymmetric profiles of spectral lines (Gadun, Hanslmeier, and Pikalov, 1997).

It is still unclear how large the microturbulence term is necessary to explain the photospheric line profiles, which is relevant to the uncertainty of the small-scale velocities. Socas-Navarro (2011) assumed that the small-scale velocity that corresponds to the microturbulence term is so small that they ccould fit the spectral line profiles observed with Hinode-SOT without microturbulence. Bellot Rubio and Beck (2005) and Quintero Noda *et al.* (2014) also explain the photospheric spectra obtained with Hinode-SOT without the microturbulence term, which demonstrates that the velocity field on scales smaller than the photon mean free path ($\sim$ 100 km) is much smaller than the thermal velocity $\sqrt{2k_BT/m} = 1.3$ km/s at $T = 6000$ K.

Some other studies, however, found that the microturbulence term is necessary in the photosphere (López Ariste, Martínez González, and Ramírez Vélez, 2007; Buehler *et al.*, 2015; Guglielmino *et al.*, 2020). Buehler *et al.* (2015) estimated the average microturbulent velocities of 3.1 km/s at $\log\tau = 0$ and 0.8 km/s at $\log\tau = -0.9$ by performing a spectral line inversion with a deconvolution technique reducing the effect of the spatial resolution of Hinode-SOT. These values are comparable to the root-mean-square velocity related to the granulation of about 1.1 km/s (Oba *et al.*, 2017). This implies that the velocity fields on small scales are comparable to those on granular scales.

1.3.3 Macroturbulence

The spatial resolution on the horizontal direction is determined by the point-spread-function (PSF) of an instrument. The observed spectrum is an average within the PSF. The degradation effect with the PSF can be expressed by a convolution with the PSF at each wavelength:

$$I_\lambda^{(\mathrm{obs})}(x,y) = I_\lambda(x,y) * P, \tag{1.7}$$

$$= \int_{-\infty}^{\infty} I_\lambda(x-\xi, y-\eta) P(\xi,\eta) d\xi d\eta \tag{1.8}$$

where $I_\lambda(x,y)$ is an intensity from (x,y) at wavelength λ without spatial average, P is a point spread function, $*$ represents the convolution, and $I_\lambda^{(obs)}(x,y)$ is an observed intensity. Given a horizontal variation of Doppler velocity within the PSF, the observed spectrum can have a wide profile. By assuming the Gaussian shape of the probability density function of the velocity variation inside the PSF, then we can model the relationship as

$$I_\lambda^{(\mathrm{obs})}(x,y) = I_\lambda(x,y) * \exp\left[-\frac{\lambda^2}{v_{\mathrm{mac}}^2}\right], \tag{1.9}$$

where the parameter v_{mac} is termed macroturbulence which describes the velocity disperssion on the horizontal direction within the PSF. Thanks to this concept of the macroturbulence modeling, the effect of PSF can be treated by one free parameter

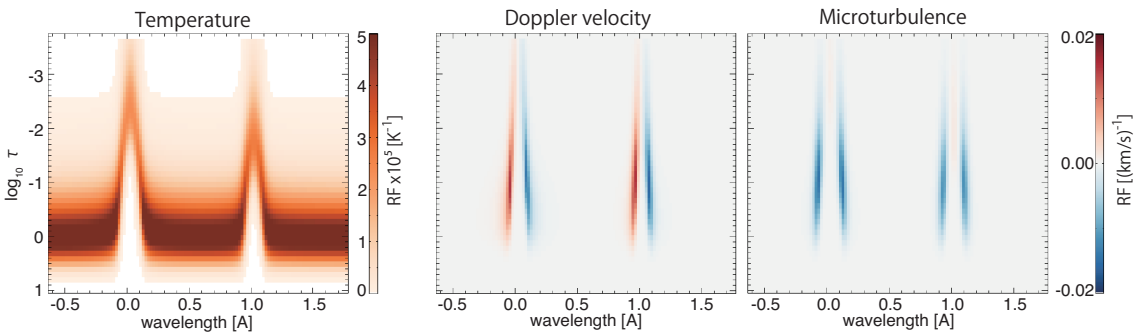

Figure 1.7: Examples of response functions for the temperature (left), Doppler velocity (center), and microturbulence (right) for the Fe I 6301.5 Å and 6302.5 Å lines. The definition is described in Eq (1.10).

$v_{\rm mac}$. The main difference from the microturbulence is that the macroturbulence causes broadening of the spectrum line profiles while it does not change the equivalent width contrary to the microturbulence.

In observations with low spatial resolutions such as Fourier transform spectrometer atlas (Wallace, Hinkle, and Livingston, 1998), the dominant source of the macroturbulent velocity is the granular motions. Recent observational instruments, however, have spatial resolutions of a few 100 km that is much smaller than the average diameter of granules of 1000 km. This is why the corresponding macroturbulent velocity is thought to be small (Socas-Navarro, 2011), whereas the degradation (Equation 1.7) can still lead underestimation of kinetic power on the small spatial scales (Katsukawa and Orozco Suárez, 2012; Oba *et al.*, 2017).

The microturbulence and macroturbulence terms correspond to the velocity fields on scales smaller than the resolution limit of the instrument. Therefore, qualitatively, they are related to the integrated power of the power spectrum of vertical velocity on scales smaller than the small scales. The uncertainty of the microturbulence term is essentially related to the uncertainty of the power-law index.

1.3.4 Analyzing the spectral line profiles

The 1st-order perturbation analysis of the radiative transfer equation provides a relationship between the small perturbation of physical quantity and corresponding change of emergent intensity (Landi Degl'Innocenti and Landi Degl'Innocenti, 1977):

$$\delta I_\lambda = \int_0^\infty R_\xi(\lambda, \tau)\xi(\tau)d\tau, \tag{1.10}$$

where R_ξ is called response funcion for a physical quantity ξ as shown in Figure 1.7 (see also Appendix A). The response function for Doppler velocity perturbation at the wavelength of -60 mÅ from the 6301.5 A. is shown in Figure 1.8. The emergent intensity is largely affected by the Doppler velocity at $\log_{10}\tau \sim -1$, but has a sensitivity from $\log_{10}\tau = 0$ to -3. Since the perturbation of the emergent intensity is written by an integration (Equation 1.10), the emergent line profile reflects the weighted average of the LOS velocity as a Doppler shift of the entire profile. The LOS velocity gradient on the scales larger than the width of the response function along the optical depth tends to cause asymmetry of the emergent spectral line profiles. On the other hand, the LOS velocity gradient on the scales smaller than the width along the optical depth tends to cause broadening of the profiles.

A bisector analysis is a method to retrieve the LOS dependence of the Doppler velocity from one observed spectral line profile without using any atmospheric models. The bisector analysis is based on the fact that the line core reflects the physical condition at a higher layer in the atmosphere whereas the line wing reflects that at a lower layer, owing to the different absorption coefficients. Following the idea of a generalized response function introduced by Ruiz Cobo and del Toro Iniesta (1994), González Manrique *et al.* (2020) calculated the response functions to the bisector velocities (Figure 1.9; see also Appendix B). They demonstrate that the velocity gradient on scales larger than $\Delta(\log_{10}\tau) \gtrsim 1$ can be detected by measuring the difference between the bisector velocities at lower (e.g. 10%) and higher (e.g. 70%) bisector levels. On the other hand, it is difficult to detect small-scale velocity gradient within $\Delta(\log_{10}\tau) \lesssim 1$, since it is comparable to the widths of the response functions along the optical depth: the average value is reflected in the measured

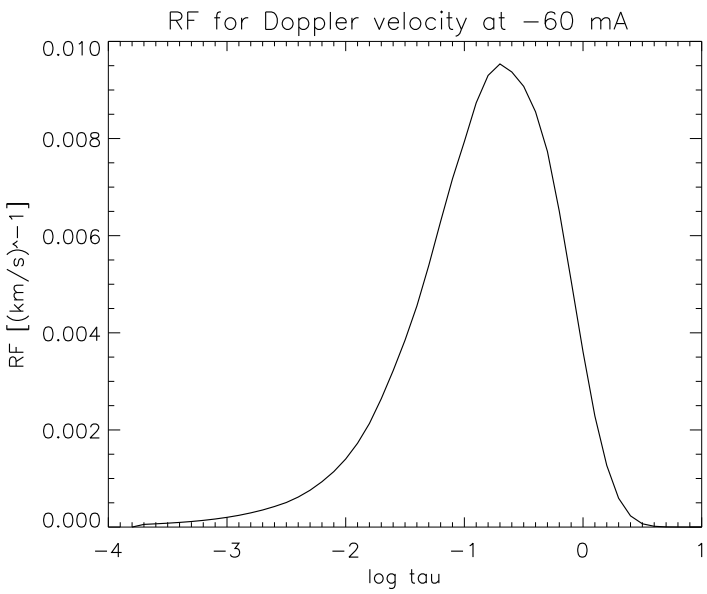

Figure 1.8: The response function of Doppler velocity for Fe I 6301.5 Å line at wavelength of -60 mÅ from the line center.

bisector velocity and the velocity variation on small scales will contribute the line broadening via something like the microturbulence effect.

1.3.5 Line Broadening and Granulation

Small-scale variation of LOS velocity can be measured by analyzing the spectral line broadening as mentioned above. The spatial variations of the FWHM of photospheric spectra are pointed out to be larger in intergranular lanes than in granules using observations barely resolving the granulation scale (Holweger and Kneer, 1989; Nesis *et al.*, 1992). Nesis *et al.* (1992) argued that the line broadening is related to turbulent motions caused by shocks driven by supersonic flows in granulation. However, Solanki *et al.* (1996) and Gadun, Hanslmeier, and Pikalov (1997) performed 2-dimensional hydrodynamic numerical simulations and calculated the photospheric spectral line widths. They concluded that LOS gradients of LOS velocities related to

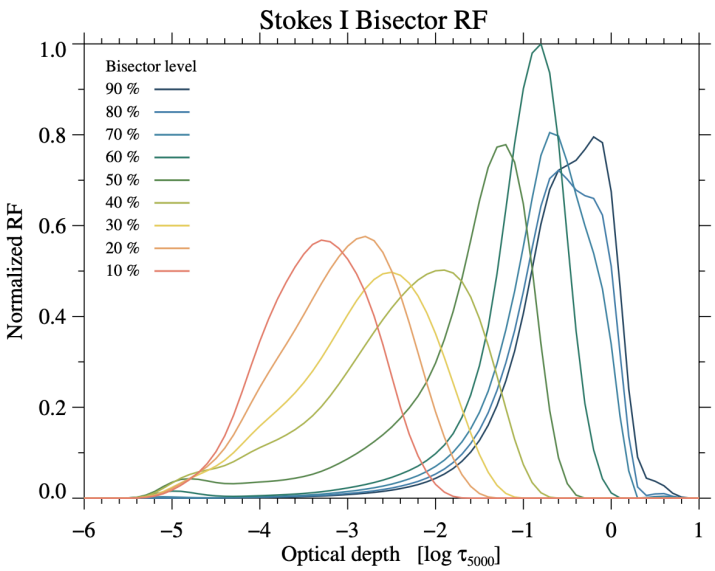

Figure 1.9: Response functions to the bisector velocities of Si I 10827 Å calculated by González Manrique *et al.* (2020).

the granulation can cause the spectral line broadening and the excess line broadening in intergranular lanes can be explained by the strong gradient of vertical velocities. In addition, Solanki *et al.* (1996) and recent numerical simulation (Vitas *et al.*, 2011) found that the supersonic motions are preferentially seen as horizontal flows, which implies that the line broadening that is relevant to shocks can be observed only in a limb observation (Bellot Rubio, 2009).

Khomenko *et al.* (2010) observed the photospheric spectra near the disk center with SUNRISE/IMaX imaging spectropolarimeter using a narrow-band tunable filter (Barthol *et al.* 2011; Solanki *et al.* 2010; Martínez Pillet *et al.* 2011) and derived the spatial distribution of spectral line widths by a single Gaussian fitting that assumes a symmetric spectral line profile. They found that the spectral line widths are wide in the intergranular lanes, which was consistent with the earlier studies mentioned above. They newly found that the line widths were narrow at the boundaries between granules and intergranular lanes (Figure 1.5) and suggested that

the narrow width can be explained by the velocity gradient scenario: the flows are preferentially horizontal at the boundaries so that the vertical gradient of vertical velocity that can cause the line broadening is small. However, they could not obtain asymmetry of the spectral line and argue the origin of the line broadening because of limited wavelength resolution and sampling by the filtergraph instrument. There are studies reporting enhanced line broadening in localized regions near the boundary between granules and intergranular lanes by performing spectroscopic observations (Nesis *et al.*, 1993; Hanslmeier, Nesis, and Mattig, 1994), which seems inconsistent with the results of the filtergraph observation (Khomenko *et al.*, 2010).

1.4 Spectropolarimetric Observation with the Hinode-SOT

We examined spectropolarimetric data obtained with the Solar Optical Telescope (SOT; Tsuneta *et al.* 2008) onboard the Hinode satellite (Kosugi *et al.* 2007). Here, we overview the spectropolarimetry performed by the Hinode-SOT.

1.4.1 The Spectropolarimeter of the Hinode-SOT

The SOT includes a diffraction-limited 50-cm aperture Gregorian telescope. The diffraction limit at 6300 Å is about 0.″32, which is equivalent to about 230 km on the solar photospheric surface. The Hinode-SOT observes the photospheric visible lines with the Broadband Filter Imager (BFI), the Narrowband Filter Imager (NFI), and the Spectropolarimeter (SP). The SP covers two neutral iron lines: Fe I 6301.5 Å and 6302.5 Å, which arise from the same multiplet, having similar formation properties. On the other hand, the effective Lande factors of the lines that indicate sensitivities to the Zeeman effect are 1.67 for 6301.5 Å and 2.5 for 6302.5 Å, which helps to derive magnetic field strength from the spectropolarimetric data. Moreover, the formation height of the two lines are slightly different: the line core of 6301.5 Å line is sensitive to upper layer compared to that of 6302.5 Å as shown in Figure

1.7. The SP measures the four Stokes profiles (I, Q, U, V) through a North-South directed slit and has the slit-scan mechanism which enables us to perform scanning observations with 0.″1476 slit step in the West-East direction.

The line spread function of the SP has a symmetric profile that can be fitted well by a Gaussian function with FWHM of about 24.6 mÅ, which is comparable to the spectral plate scale of 21.6 mÅ/pixel (Lites *et al.*, 2013). This allows us to neglect the spectral asymmetry caused by instrumental effects.

The greatest advantage of the Hinode-SOT is the stability of the image quality: the SOT has high spatial resolution so that we can clearly resolve the granule-scale structures continuously during the entire observation period. Moreover, since the SOT measures polarization, i.e. Stokes vectors, of the Fe I lines, the SOT provides vector magnetic fields with high spatial resolution and stability. These have not been achieved before Hinode.

1.4.2 Slit-Scan Observation

In this thesis, we examine data obtained with slit-scan observation with the SP. There are two types of data: one is a normal map data, which includes a single slit-scan with wide FOV of $160'' \times 160''$ and the 4.8 sec exposure at each scan step. The other is dynamic mode data, which performs repetition of slit scans of narrow FOV with a short time cadence ($\lesssim$ 1 min). The normal map observation provides more accurate data (the noise level is about 0.5 % of the continuum intensity) due to the long exposure time, and includes various structures in a wide range of spatial scales from 0.2 Mm to 120 Mm because of the large FOV. In the contrast, the dynamic mode can detect short-timescale evolutions of spectral line profiles associated with the granular dynamics.

1.5 Purpose of this thesis

Thanks to the development of the telescopes and observational techniques, as realized by Hinode, we have the ability to resolve and evaluate the granular motions

and to detect some signatures of small-scale flows on the solar surface. However, the small-scale flow fields are still difficult to be measured observationally. This is because that the spatial resolutions of the current instruments are comparable to the widths of intergranular lanes where the small-scale flows are thought to be enhanced and such flows strongly interact with magnetic fields.

Since the observing techniques are different depending on the direction of the velocity, we separately study them in the following chapters. We can measure the horizontal velocity fields by analyzing the temporal evolutions of the granular patterns. It is pointed out that such measurements are likely to underestimate the small-scale velocities. We try to overcome this problem and to evaluate the velocity fields on scales close to the resolution limit. On the other hand, the spectral line widths may reflect the LOS component of small-scale velocity fields. But observing them with high spatial, spectral, and temporal resolutions is still challenging. Because of this difficulty, there are remaining issues such as (1) the spatial and temporal associations between the spectral line widths and the granulation are still obscure, (2) the value of the microturbulence term is ambiguous. They are related to the fundamental question: what is the origin of the line broadening? These problems are critical to understand the physical mechanism for driving the turbulent motions and to measure the amount of kinetic energy in the photosphere. In this thesis, we challenge to solve these problems by analyzing the spatial and temporal evolutions of spectral line profiles. Details are given below.

In Chapter 2, we develop a new method to infer the horizontal velocity field in the solar photosphere based on a multi-scale deep learning architecture. Because the horizontal velocity field is preferentially perpendicular to the LOS direction, we cannot measure it using the Doppler effect. Using the spatial and temporal variations of the intensity and vertical velocity obtained by 3D numerical simulations for the surface convection, the multi-scale deep learning provides an estimate of the horizontal velocity. Furthermore, we newly introduce a coherence spectrum to evaluate the dependence of the estimation accuracy on the spatial scales to the argue advantages and limitations of the method. We discuss the advantage of the

multi-scale deep learning architecture to estimate the horizontal velocity.

In Chapter 3, we perform bisector analyses of the Fe I 6301.5 Å spectrum line profiles observed with Hinode-SOT to investigate the spatial variations and temporal evolutions of the line broadening and LOS velocity gradient. We mainly focus on the spatial and temporal variations of FWHM of the line profiles. These variations of the FWHM may be related to the microturbulence and/or macroturbulence term, and their association with the granular patterns and the granular dynamics will provide important information on the physical process. The large FWHM was reported to be seen in intergranular lanes in some studies (Nesis *et al.*, 1992; Khomenko *et al.*, 2010) while other studies reported the large FWHM in local regions between granules and intergranular lanes (Nesis *et al.*, 1993; Hanslmeier, Nesis, and Mattig, 1994). It is important to find where the large FWHM appears associated with the granular structures and to clarify how the broadening is related to the LOS velocity gradient obtained by the bisector analysis. The study provides a clue to assess small-scale flows by evaluating excessive line broadening that cannot be explained only by the LOS velocity gradient.

In Chapter 4, we aim to infer the velocity fields related to the variation of FWHM found in Chapter 3. First, we perform spectral line inversion of both Fe I 6301.5 Å and 6302.5 Å lines to evaluate the turbulent velocities that broaden the spectral line profiles in the fading granules. Although many authors have executed spectral line inversion to fit the photospheric spectra, determining the microturbulence term is still challenging. The average microtubulence terms estimated by spectral line inversions in previous studies range from 0 km/s (e.g. Socas-Navarro 2011) to 3.1 km/s (Buehler *et al.*, 2015) at the solar surface. Since the root-mean-square velocity of granulation is 1.1 km/s, this uncertainty is large and has to be constrained. The difference of the inversion condition such as the different number of free parameters may cause this uncertainty. Therefore, we perform the spectral line inversions both with and without microturbulence term to check the validity of the inversion results. In addition, we aim to identify the physical process that causes the line broadening and the quantitative relation between the velocity and FWHM. For this purpose, we

analyze the MHD simulation results and calculate the radiative transfer to reproduce the spectral line profiles relevant to the granulation.

Chapter 2

Multi-scale deep learning for estimating horizontal velocity fields

2.1 Introduction

The dynamics in the solar photosphere are governed by thermally driven convection. This in turn produces cellular patterns termed as granules that are observed in visible-light continuum images. The bright areas with hot rising flows are surrounded by darker and cooler intergranular lanes. A typical granule has a diameter of approximately 1000 km and lasts for approximately 10 min (Nordlund, Stein, and Asplund 2009 and references therein). The turbulent nature of the granular convection inherently creates small-scale flow structures that are smaller than the typical size of granules (e.g. Matsumoto and Kitai 2010, Katsukawa and Orozco Suárez 2012, Rempel 2018). These types of small-scale flows interact with magnetic fields and can produce the Poyinting flux upward. This in turn can drive various phenomena, such as explosions (Shibata *et al.*, 2007; Toriumi, Katsukawa, and Cheung, 2017), jets (Hollweg, Jackson, and Galloway, 1982; Iijima and Yokoyama, 2017), and heating (van Ballegooijen *et al.*, 2011; De Pontieu *et al.*, 2012), in the upper atmo-

sphere, chromosphere, and corona. Supergranulation is another convective patterns observed on the solar surface, which is characterized by a horizontal flow fields with the large spatial scale of about 30 Mm (Rieutord and Rincon, 2010) and the typical lifetime of about 1.7 days (Hirzberger *et al.*, 2008). Photospheric magnetic fields are passively advected into the edges of supergranules and form network structures (Gošić *et al.*, 2014). Recent observation found that persistent vortex flows exist at supergranular vertices, and magnetic flux can be concentrated in the vortices (Requerey *et al.*, 2018).

We can obtain the line-of-sight (LOS) component of the flow velocities by a spectroscopic observation via the Doppler effect. Conversely, to date, there are no direct methods for observing the components perpendicular to the LOS. These components correspond to the horizontal velocity on the solar surface in disk center observations. The most commonly used method for estimating the horizontal velocity field is local correlation tracking (LCT; November and Simon 1988). This method uses two consecutive images and computes the cross-correlation, and thereby detects the motions of granule patterns. Although the LCT technique can evaluate the horizontal velocity with good accuracy on a larger scale, its accuracy on a scale smaller than granules is limited by as much as factor of three (Verma, Steffen, and Denker, 2013) or more (Malherbe *et al.*, 2018). The errors are preferentially high in the boundaries between granular cells (Louis *et al.*, 2015). This is mainly due to the fact that the window utilized in the LCT method to compute the cross-correlations blurs velocity fields. However, the accuracy on a smaller scale is important for evaluating the interaction between magnetic fields and horizontal flows because the magnetic fields are often concentrated in small regions in the photosphere (e.g., Parnell 2002).

An alternative approach involves identifying features that are observed as bright points in G-band or continuum images and obtaining horizontal velocities by tracking them (Berger *et al.*, 1998; Utz *et al.*, 2010). The method can provide horizontal velocities of small magnetic features in intergranular lanes. Given that such magnetic features appear associated with strong concentrations of magnetic fields, we cannot obtain velocity fields and their spatial distribution across the entire areas by

using this method.

A new method for estimating the horizontal velocity involves a deep learning approach. Asensio Ramos, Requerey, and Vitas (2017) developed a model by using a convolutional neural network (DeepVel), which was trained on a set of velocity fields simulated for the photosphere. DeepVel can estimate the horizontal velocity without averaging at various heights in the solar atmosphere. Tremblay *et al.* (2021a) showed that the Pearson linear correlation between the estimation and the answer is about 0.8. The correlation increases when the horizontal velocity fields are averaged over several granular life times (Tremblay *et al.*, 2018), The increment of the accuracy by taking average is a same trend as the LCT behaves. The results of DeepVel and LCT are similar when they are averaged, whereas DeepVel still have an advantage for reproducing the kinetic power spectra on the scales smaller than supergranules. Tremblay and Attie (2020) developed a new architecture for DeepVel with using the U-NET architecture and found that it is more efective than other tracking methods. However they did not verify their accuracies at various spatial scales.

There are several concerns to estimate the horizontal velocity on the small scales, which shoud be clarified before we use the method to observational data. Motivation of this study is to evaluate the accuracy of the methods on various spatial scales and to reveal weeakness and possible improvements. We developed a new method for estimating the spatial distribution of the horizontal velocity based on a multi-scale deep learning architecture with several sizes of convolutional kernels to capture the multi-scale nature of the solar convection. We adopted the new method to three different numerical simulations of convection and discussed the relationship between the power spectra of the velocities and performance of the network. Furthermore, we suggested a new measure for evaluating scale-by-scale velocity estimation.

2.2 Method

We developed a convolutional neural network that predicts the spatial distribution of the horizontal velocity from the spatial and temporal variations of vertical veloc-

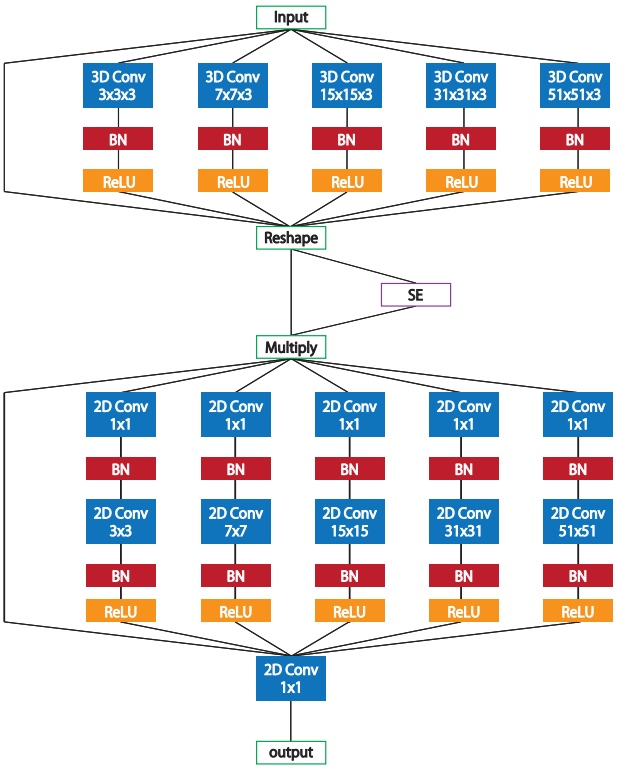

Figure 2.1: Structure of the network. BN and SE denote the batch normalization and squeeze-and-excitation, respectively. The number of kernels in each convolutional layer is presented in Table 2.1.

Table 2.1: Number of kernels in each convolutional layer.

	3×3	7×7	15×15	31×31	51×51
3D Conv	60	40	20	10	10
2D Reduce	20	10	5	5	2
2D Conv	60	40	20	10	10

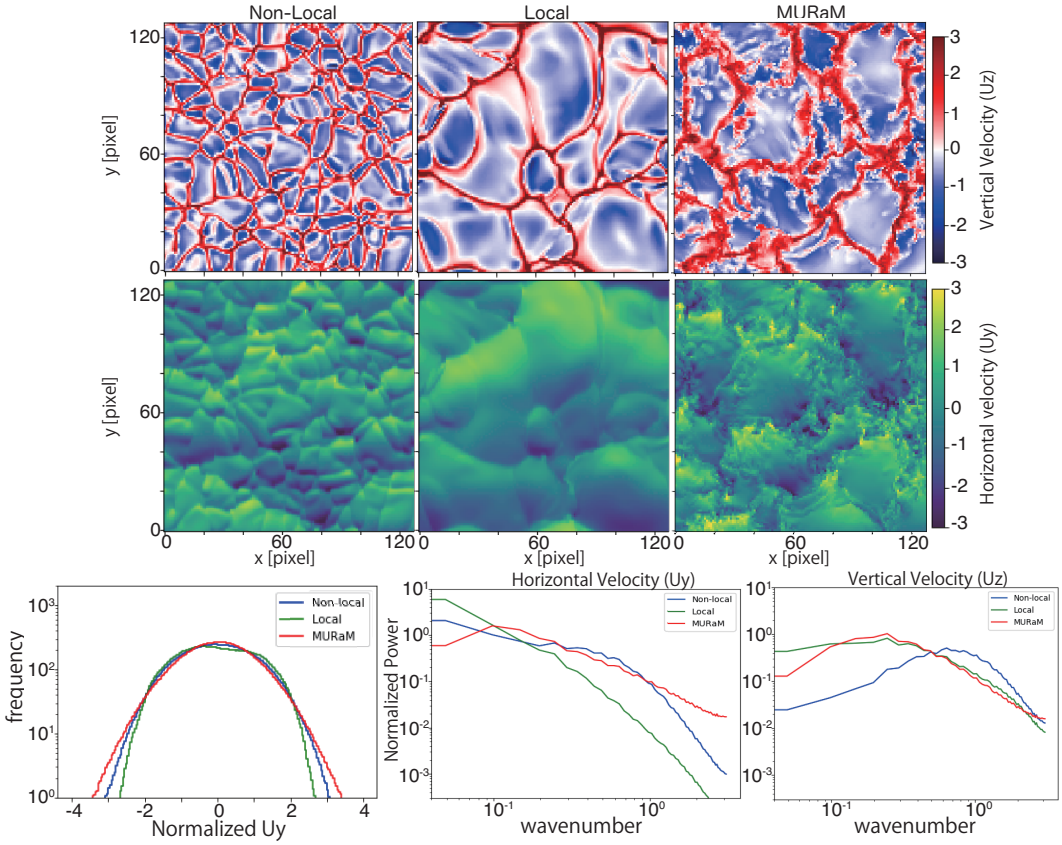

Figure 2.2: Representation of the training data sets. The spatial distributions of the vertical velocities (top panels) and Y component of the horizontal velocities (middle panels) of the non-local (left), local (center), and MURaM (right) simulation data. The bottom panels show the probability density functions (left), power spectra of the horizontal velocities (center), and power spectra of the vertical velocities (right) of the three simulations. The vertical and horizontal velocities in the simulations are normalized with zero and unit dispersion. This satisfies Equation (2.3).

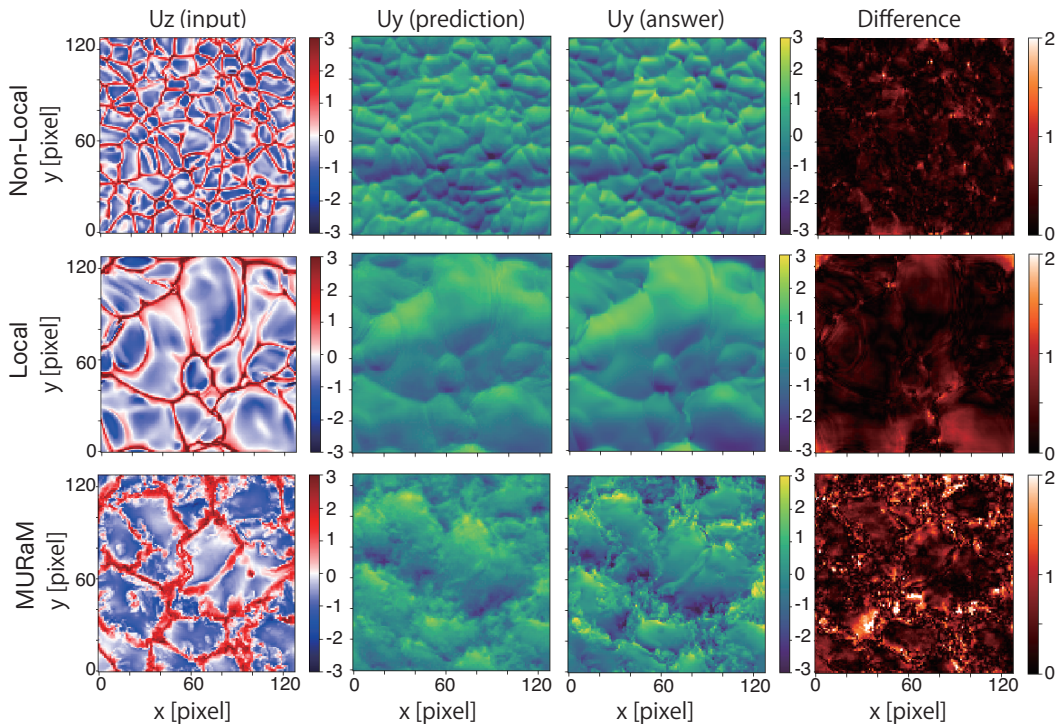

Figure 2.3: Spatial distributions of the vertical velocity, Y component of the horizontal velocities during the prediction and simulation, and the difference between them in the Non-local model (top), the Local model (middle), and the MURaM model (bottom), respectively. The vertical velocity and horizontal velocity in the simulation are normalized as zero mean with unit dispersion. It should be noted that the vertical velocity and temperature are used for the inputs even though only the vertical velocity is shown in this figure.

ity and temperature. This model includes multi-scale deep learning architectures: the convolution layers have various sizes of the receptive fields (Figure 2.1 and Table 2.1). The sizes of the kernels corresponded to 3×3, 7×7, 15×15, 31×31, and 51×51. This type of multi-scale architecture exhibits an advantage in detecting the solar convection motion, which is highly turbulent to the extent that the horizontal velocities exhibit broad power spectra. This architecture is similar to the inception module (Szegedy *et al.*, 2014). The inception module is a network that consists of kernels with various sizes, i.e., 1×1, 3×3, and 5×5, and the pooling layer. By utilizing the kernels with varying sizes, the inception module can not only efficiently detect spatially concentrated structures in a single region but also highly spread structures.

In the first block of the model, 3-dimensional convolutions were conducted along the spatial and temporal axes, and the channels corresponded to the different physical quantities. After the first block, the data was reshaped, and thereby time and physical quantities were converged into the new channels. Then, in the second block, the convolutions were conducted only along the spatial axes. A potential problem corresponds to the large number of parameters due to the large size of kernels corresponding to 31×31 and 51×51. To reduce the number of parameters, we also included 1x1 convolutions before each convolution layer. Furthermore, some of the outputs of the convolutions were highly correlated. This can decrease the efficiency of the optimization. The 1×1 bottle-neck layer can partially resolve this problem. After the 3-dimensional convolutions, the feature maps have 4 dimensions: two spatial sxes, temporal axes, and channels. The reshape layer concatenate the temporal axes and the channels to change the structure of the feature maps into 3 dimensions. The squeeze-and-excitation block (Hu, Shen, and Sun, 2017) can improve the performance of the network by modelling interdependencies between the channels. This squeeze-and-excitation block produces a collection of modulation weights for the channels. These weights are applied to the feature maps by multiplying and the results are fed into the subsequent layers. Additionally, we included the batch normalization (Ioffe and Szegedy, 2015) after all the convolutions. This normalized

the outputs of convolutions into zero mean and unit covariance, and this in turn accelerated the training. All the convolution layers were initialized with a random method (He *et al.*, 2015b). Asensio Ramos, Requerey, and Vitas (2017) developed a deep neural network model (DeepVel) to estimate the horizontal velocity. Their model was based on ResNet (He *et al.*, 2015a), which consists of deeply stacked layers with only 2-dimensional convolutions [1] with a receptive field of 3×3. The total number of trainable parameters of our model corresponded to $\sim 4.0 \times 10^5$, which was less than that of DeepVel by a factor of 4.

2.3 Data

To train the neural network, we used numerical simulation data in three different types of convection models. By comparing several cases with different energy injection scales and spectral properties, we can evaluate and discuss the versatility of the neural network.

The first model is a convection model, in which convection is driven via cooling at the top boundary. We termed this model as *non-local* one. The 3-dimensional compressible MHD turbulence without any rotations was considered in a Cartesian domain by covering the depth of the convection zone (Masada and Sano, 2016). The horizontal sizes of the domain were four times larger than the vertical size. The super-adiabatic condition with the superadiabaticity $\delta \simeq 10^{-5}$ was imposed on only 5% of the region to ensure that the top boundary was convectively unstable, whereas the remaining part of the region remained adiabatic to ensure convective stability. The cool downward plumes produced near the top boundary drove the convection: fast downward motions with the entrainment behavior appeared locally and transiently.

[1] Asensio Ramos, Requerey, and Vitas (2017) that describe the convolution as ‘3-dimensional’. The convolution was performed along spatial axes (x and y axes) and also dealt with the channels. In this paper, we termed this as ‘2-dimensional’ after the procedure name ‘Conv2D’ in Keras. The 3-dimensional convolution in our network represents the convolution along the spatial and time axes as channels.

The second model was termed as *local* model. This is a convection model, in which convection is driven by local entropy-gradient. The entire convective zone was convectively unstable with super-adiabatic conditions. The same Cartesian domain was considered as that in the non-local model. Unlike the non-local model, convective cells were generated over the entire convective zone, in which the spatial scale of cells were dependent on the local scale height in the vertical direction (Cossette and Rast, 2016). Hence, the convective motions with larger cells, which were produced near the bottom region, were more pronounced in the local model when compared to those in the non-local model.

In the numerical simulations for the non-local and local models, a spatial resolution of $256 \times 256 \times 128$ was used. The other physical and numerical parameters were similar to those in an earlier study by Masada and Sano (2016) (see Yokoi, Masada, and Takiwaki 2021 for details.). The apparant convective cells in the non-local and the local simularion roughly correspond to supergranular cells rather than granular ones. The spatio-temporal data of simulated turbulent fields were utilized for training the network, in which the MHD turbulence was fully developed to the statistically steady state after several tens of the turnover time of the convective cells. We used the temperature and vertical velocities at 3.3 Mm below the top boundary as the input data of the network. Furthermore, the horizontal velocities were at the same depth as the that of corresponding ground truth. We performed downsampling for these data by setting their size to 128×128 pixels, which covered the entire region of 748 Mm$\times$748 Mm. Specifically, 1000 snapshots were available for both the models. Because the input data are not representing the parameters on the surface, the network thus trained is not directly applicable to an observation. Instead we compare the characteristics of the network with the ones trained with a realistic simulation described in the following.

We also used a three-dimensional compressible radiation MHD simulation, which was calculated with the MURaM code (Vögler *et al.*, 2005), as the third model. In the code, the radiative energy exchange was solved via a non-gray radiative transfer under the assumption of local thermal equilibrium (LTE) to reproduce

more realistic granular scale flows in the photosphere. Hence, in this study, we used the same simulation setup as that used by Riethmüller *et al.* (2014), in which the simulation box covered 6 Mm in both horizontal directions with a grid size of 10.42 km and 1.4 Mm in the vertical direction with a 14 km grid size. A unipolar homogeneous vertical magnetic field of $B_z = 30$ G was introduced as an initial condition. The simulation used a fully-developed hydro-dynamical simulation as the initial condition and additional calculation for 3 hour of solar time that is enough to reach a statistically stationary state. We obtained more than 1600 snapshots of the data cube with a mean cadence of 35 s. We extracted a small region, which covers 5.4 Mm in both the horizontal directions, and downsampled the region with a grid size of 42 km. Thus, the size of the region corresponded to 128×128 pixels. We used the temperature and vertical velocity at the surface with an optical depth of unity.

The snapshots of the three simulations are shown in Figure 2.2. The top three panels show the spatial distributions of the vertical velocities (U_z), while the middle three panels show those of the horizontal velocities (U_y). The vertical and horizontal velocities of each model were normalized with averages and standard deviations. The bottom left panel shows the probability density functions of the horizontal velocities of the three simulations. The fast velocity component existed in certain localized regions within short lifetimes. This appeared as a non-gaussian distribution in the probability density function. The power spectra of the horizontal and vertical velocities are shown in the bottom center and right panels. Here, the power spectrum of a physical quantity X is defined as follows:

$$E_X(k) = \frac{1}{2\Delta k} \sum_{\sqrt{k_x^2+k_y^2}\in[k-\Delta k/2, k+\Delta k/2)} |\hat{X}(k_x, k_y)|^2, \tag{2.1}$$

where Δk denotes the sampling interval of the wavenumber and $\hat{X}$ denotes the Fourier transform of the spatial distributions of the physical quantity X. The Fourier transform of X is as follows:

$$\hat{X}(k_x, k_y) = \frac{1}{N^2} \sum_{x,y} X(x, y) \exp[-i(k_x x + k_y y)], \tag{2.2}$$

where N^2 denotes the number of pixels in an image, which corresponded to 128×128. Then, the power spectrum was consistent with that defined in a previous study (Rieutord *et al.*, 2010) and satisfied

$$\frac{1}{2}\overline{X^2} = \int_0^\infty E_X(k)dk, \tag{2.3}$$

where the overline denotes the average over the entire FOV. Given the normalization of the vertical and horizontal velocities, the dispersion $\overline{X^2}$ corresponded to unity.

The power spectra of the vertical velocity showed their peaks. These peaks corresponded to the 'typical' scales of the convective cells, while the spectra were broad. The power spectra of the horizontal velocity exhibited high power on large-scales, whereas they did not exhibit clear peaks, especially in the non-local and local models.

2.4 Training process

We used the spatial distributions of temperature and vertical velocity with a size of 128×128 pixels and three consecutive frames as the input data. The output of the network was the spatial distribution of the horizontal velocity (U_x or U_y). We used the mean squared error between the horizontal velocities predicted by the network and those in the original data set for the loss function. The loss function was expected to be minimized in the training. Each physical quantity in the data set was normalized to zero average and unit standard deviation. We prepared 350 sets of data for the training, 40 sets for the cross-validation, and 40 sets for the test. Although the snapshots in the data sets were temporally consecutive, the training, cross-validation, and test data sets were separated sufficiently with an ample time interval that was longer than the turn-over times of the convection in all the simulations. The optimization of the network was performed by using the Adam first-order gradient-based optimization (Kingma and Ba, 2014).

Given the normalization of the training data set, the average and standard deviation of the horizontal velocity predicted by the network were also near zero and

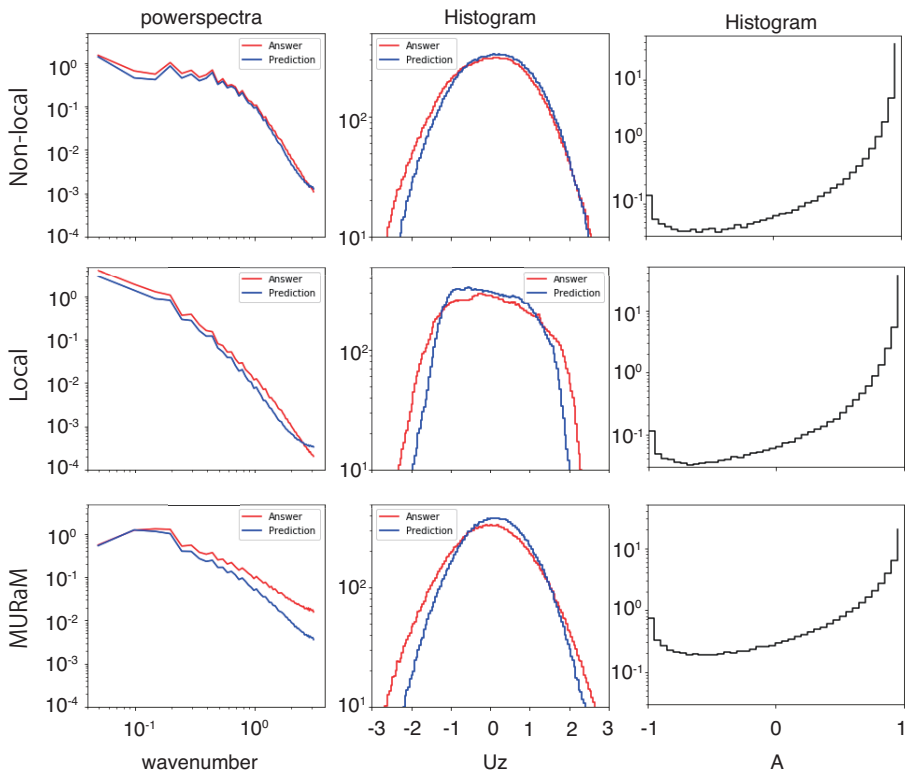

Figure 2.4: Comparison between the simulated velocity field (red) and predicted velocity (blue) in terms of power spectra (left) and histograms (center). The histograms of normalized dot product (see Eq.2.4) are shown in the right column.

unity, respectively. When we develop a network for application to an actual observational data, the network should be supervised by realistic numerical simulations of the photosphere, such as MURaM, with the spectral line synthesis and degradation with respect to the PSF of observational instruments. The network should predict the absolute value of the horizontal velocity without any normalization. Hence, restoration of the velocity from the normalized value after the prediction by multiplying the standard deviation of the horizontal velocity in the simulation or that obtained with recent observations (e.g., Oba, Iida, and Shimizu 2020) can potentially be an option.

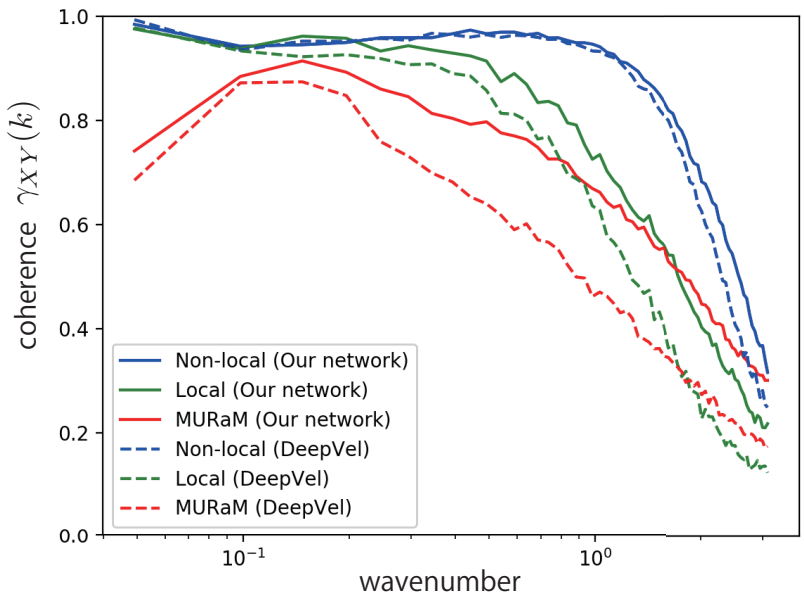

Figure 2.5: Coherence spectra between the simulation and prediction as a function of the wavenumber with our network (solid) and DeepVel (dashed; Asensio Ramos, Requerey, and Vitas 2017). It should be noted that the vertical velocity distribution as opposed to the emergent intensity is used for the input to DeepVel . The coherence spectra show strong scale-dependence.

Table 2.2: global correlation coefficients with different inputs.

	Non-local	Local	MURaM
U_z, T	0.948	0.948	0.771
U_z	0.942	0.950	0.738
T	0.890	0.884	0.668

2.5 Results

In this section, we show the comparison between the original simulation and model prediction of the horizontal velocities for the three convection models. In the LCT and DeepVel, only the emergent intensity distributions were used for the estimation. Furthermore, we used the vertical velocity distributions for the input of the network and examined their benefits. Table 2.2 lists the results with different inputs for each convection model. The results showed that higher accuracy of estimation was realized by using the vertical velocity when compared to the temperature distributions. This result is consistent with Tremblay and Attie (2020) By using vertical velocity and temperature, the network exhibited the highest global correlation coefficient. However, it was slightly smaller than that obtained by using only vertical velocity for the local model. In the rest of this paper, we focus on the network that uses the vertical velocity and temperature as the input.

Figure 2.3 compares the horizontal velocity distributions in the simulation and prediction for each convection model. In the figure, similar cellular patterns are observed in the simulated and predicted distributions. The global correlation coefficients were 0.948, 0.948, and 0.771 for the non-local, local, and MURaM models, respectively. The performance of the network for the MURaM model was worse when compared with those for the non-local and local models in terms of the global correlation coefficients, and the predicted patterns appeared blurred. The right column in Figure 2.3 shows the differences between the simulations and predictions.

The difference was expected to be likely high at the boundaries between the convection cells. This was similar to the trend observed in the case of the LCT method (Louis *et al.*, 2015). Although only the results for the U_y are shown in the Figure, the results for the U_x are similar to those because of the symmetric setup of the simulation and the network.

Figure 2.4 shows the comparisons between the simulated velocity fields and predicted velocity fields in terms of the power spectra and histograms. The power spectra of the predicted horizontal velocity distributions were similar to those of the simulation in the larger scales. However, the power spectra were slightly underestimated in all the scales and noticeable errors were observed in the smaller scales. In the case of the MURaM model, the network significantly underestimated the velocity in small-scales. The occurrence of the fast velocities became less frequent in the predictions. The blur in the images blended the fast velocity components which were preferentially localized in the small regions.

We also investigated dot products between the estimated and the simulated horizontal velocity vectors. The normalized dot product at each pixel is defined as follow:

$$A = \frac{\boldsymbol{v} \cdot \boldsymbol{v}_0}{||\boldsymbol{v}||\ ||\boldsymbol{v}_0||}, \tag{2.4}$$

where $\boldsymbol{v}$ and $\boldsymbol{v}_0$ represent the estimated and the simulated horizontal velocity vectors, respectively. This definition is consistent with Tremblay and Attie (2020) and Tremblay *et al.* (2021b). This dot product indicates the difference of the orientation of the vectors. The histograms shown in the right column of Figure 2.4 have a peak around $A \sim 1$, which indicates that the estimated and the simulated horizontal velocity vectors are well aligned in the most regions. The histograms have tails toward the negative dot products, although the fraction of the tails is small. The tail is relatively large in the histograms for the MURaM model. The average of the normalized dot products are 0.92, 0.91, and 0.70 for the non-local, local and the MURaM model, respectively.

To examine the performance of the network, we defined the coherence spectrum, which represents the correlation at each wavenumber. This has never been intro-

duced in past studies including as Louis *et al.* (2015) and Asensio Ramos, Requerey, and Vitas (2017). The coherence spectrum of distributions of two physical quantities X and Y can be defined as follows. First, we calculate the cross-spectrum of X and Y as follows:

$$S_{XY}(k) = \frac{1}{2\Delta k} \sum_{\sqrt{k_x^2+k_y^2} \in [k-\Delta k/2, k+\Delta k/2)} \langle \hat{X}^* \hat{Y} \rangle (k_x, k_y), \tag{2.5}$$

where asterisk denotes the complex conjugate, and the ensemble average $\langle\rangle$ is calculated over all the 40 frames in the test data. Finally, we defined the coherence spectrum by normalizing the cross-spectrum with the average power spectra as follows:

$$\gamma_{XY}(k) = \frac{S_{XY}(k)}{\sqrt{\langle E_X \rangle (k) \langle E_Y \rangle (k)}}. \tag{2.6}$$

The cross-spectrum $\hat{X}^* \hat{Y}$ is equivalent to the Fourier transform of the cross-correlation function of X and Y. Therefore, the coherence spectrum $\gamma_{XY}(k)$ represents the correlation between the two distributions at each wavenumber. A useful relationship exists among the coherence spectrum, power spectra, and global correlation coefficient as follows:

$$R_{XY}(0,0) = \frac{\sum_k \sqrt{\langle E_X \rangle \langle E_Y \rangle} \gamma_{XY}(k)}{\sqrt{\sum_k \langle E_X \rangle (k) \sum_{k'} \langle E_Y \rangle (k')}} \approx \frac{\sum_k \langle E_X \rangle (k) \gamma_{XY}(k)}{\sum_k \langle E_X \rangle (k)}, \tag{2.7}$$

where $R_{XY}(0,0)$ denotes the global correlation coefficient without any translation (see Appendix C). This equation indicates that the global correlation coefficient is equivalent to the average of the coherence spectrum weighted with the power spectra. Hence, this highlights the importance of the coherence spectrum analysis, shown in this study, in examining the prediction accuracy scale-by-scale, particularly in small-scale structures. As evident in the local model, the power spectrum of the horizontal velocity exhibited high power in large scales. Subsequently, the coherence spectra of large scales exhibited high importance for the global correlation coefficient. Conversely, the power spectrum of the horizontal velocity in the MURaM model exhibited relatively high power in small scales when compared to the non-local and

local models. This indicated higher importance of the coherence spectra of small scales.

The results of the coherence spectra $\gamma_{XY}(k)$ for the three convection models are shown in Figure 2.5. We reconstructed the DeepVel and trained it with the three convection simulations with vertical velocity as the input, while the original DeepVel was trained with the emergent intensity. The performance of our network was similar or better than that of DeepVel for all the simulation data and at all the wavenumbers with the exception of the large scale in the non-local model. However, it was still difficult to reproduce the small-scale structures. In the non-local and local models, the coherence spectra exceeded 0.9 for small wavenumbers and they drastically decreased to 0.3 or less for large wavenumbers. Furthermore, even the global correlation coefficients for both the models exceeded 0.9. The discussion on the small-scale structures should be treated with care even if the global correlation coefficient is high. In the MURaM model, which exhibited lower steep power spectra of the horizontal velocity (Figure 2.2), the performance was limited in a wide range of wavenumbers when compared with those of the non-local and local cases. However, a rough trend and better accuracy in large-scale were observed.

When comparing the results of the three convection models, it can be observed that the different onset of the significant decrease in the coherence spectrum appears on smaller scales as opposed to on energy injection scales where the power spectra of the vertical velocities have their peaks. This signature suggests that the decrease in performance is not simply due to the small size of the spatial patterns, but also due to a reason related to turbulent structures. For example, the energy injection scale of $k \sim 0.7$, which is observed from the power spectrum of the vertical velocity in the non-local case (Figure 2.2), is correlated to the onset wavenumber for degrading the prediction accuracy toward the high wavenumber region. This is attributed to the non-linear cascade of convective eddies. As presented in Table 2.2, the high performance of this network relies on the vertical velocity. This implies that the relationship between the horizontal and vertical flows is rather simple in large scales, whereas it is more complex in small scales probably due to the non-linearity.

The small global correlation coefficient for the MURaM model is related two characteristics of the convection: large energy injection scale and small slope of the power spectra. The energy injection scale is higher than that of the non-local model, which diminishes the coherence spectra in a wide range of spatial scales. In combination with the higher power in the small scales, the resultant global correlation coefficient becomes small for the MURaM model. A large global correlation coefficient was realized for the local model even though the energy injection scale was similar to that in the MURaM model. This was due to the fact that the power spectrum of the horizontal velocity in the local model exhibited a steep slope, which in turn induced large weights on the large-scales.

To improve the accuracy at smaller scales, the optimization of the small kernels should be performed more efficiently. A potential method of realizing this involves improving the loss function. In this study, the network was trained by minimizing the mean-squared-error between the prediction and simulation. Given that the horizontal velocity distribution exhibits high power in large-scales, as shown in Figure 2.2, larger weights are used on the larger scale structures for the loss function. This can promote the learning of the large-scale structures and can inhibit the detection of the small-scale structures. Hence, an appropriate loss function can improve the optimization. An alternative method involves increasing the number of physical quantities to the input. In this study, the spatial distributions of the vertical velocity and temperature were used as the input data. It can be beneficial to use other physical quantities, which are associated with the non-linear process such as the velocities at multiple heights. Furthermore, the spatial distributions with small-scale enhancement obtained via pre-processing can also aid in improving the performance.

2.6 Conclusions

We developed a novel convolutional neural network to estimate the spatial distribution of horizontal velocity by using the spatial distributions of temperature and vertical velocity. This new network was comprised of convolutional layers with vari-

ous sizes of receptive fields. This led to efficient detection of spatially spread features and concentrated features. Given that the velocity distribution driven by the convection exhibited multi-scale structures and broad power spectra, this type of a multi-scale network exhibited an advantage in detecting the solar surface convective motion. Our network exhibited a higher performance on almost all the spatial scales when compared to those reported in previous studies.

In most previous studies, the evaluation of the method was performed solely via the global correlation coefficient between the simulated velocity field and prediction velocity field. This in turn cannot show the accuracy on different spatial scales. To evaluate the accuracy at each scale, we introduced the coherence spectrum, which represents the correlation at each wavenumber. The evaluation with the coherence spectrum revealed the strong scale dependence of the accuracy. The horizontal velocities on large scales were well predicted with our network, while those on small scales were limited. Recently, the small-scale vortical motions in the solar photosphere has attracted significant attention observationally (Bonet *et al.*, 2008; Vargas Domínguez *et al.*, 2011) and theoretically (Shelyag *et al.*, 2011; Moll, Cameron, and Schüssler, 2011). However, given the rapid decrease of the accuracy in estimating the horizontal velocities toward the small scales, we should be careful when discussing them observationally. The accuracy for the small-scale structures is crucial for calculating vorticities via a derivative of horizontal velocities.

By comparing the results of the three convection models, we observed that the rapid decrease in coherence spectrum occurred on the scales that were lower than the energy injection scales, which were characterized by the peaks of the power spectra of the vertical velocities. This implies that the network was not appropriately trained to reproduce the velocity fields in small-scales generated by turbulent cascades. To improve the accuracy on small-scales, it is potentially important to consider improving the loss function in the network. This can be realized by adding more weights on the small-scale structures and inputting other physical quantities, such as the vertical velocities at multiple heights, which can be related to the non-linear process. These challenges can be explored in future studies.

In this study we developed a new model for estimating the horizontal velocity field with numerical simulation data and evaluated its performance with a new measure. By adopting our network to the high-resolution observation data obtained via the SUNRISE-3 balloon-born telescope (Katsukawa *et al.*, 2020; Feller *et al.*, 2020) and Daniel K. Inouye Solar Telescope (Rimmele *et al.*, 2020; Rast *et al.*, 2021), we can estimate the horizontal velocity distributions with a high accuracy in a wide range of wavenumbers.

Chapter 3

Convective dynamics studied with line broadening and asymmetry

3.1 Introduction

Regions of low solar activity, known as quiet regions of the Sun, are dominated by bright cells termed granules, which are surrounded by dark channels called intergranular lanes. Granules are caused by gas convection: hot ascending material makes a granule and cold descending material makes an intergranular lane. The behavior of granules is very dynamic that they undergo a cycle of birth, death, fragmentation, and merger. The physical properties and the temporal evolutions of granules have been reported in numerous studies (Hirzberger *et al.* 1997; Roudier and Muller 1986; Roudier *et al.* 2003; Oba, Iida, and Shimizu 2017; Oba *et al.* 2017). Some small granules fade out without any fragmentation or merger, whereas large granules principally fragment into multiple smaller granules (Hirzberger *et al.*, 1999; Müller *et al.*, 2001; Lemmerer *et al.*, 2017).

Small-scale magnetic fields are ubiquitous in such quiet regions (recent review by Bellot Rubio and Orozco Suárez 2019). Such magnetic fields are the energy source of coronal heating and solar wind acceleration (see Cranmer and Winebarger 2019 and references therein). Several observations have found that the internetwork

magnetic fields have no clear correlation with the solar cycle (Hagenaar, Schrijver, and Title, 2003; Buehler, Lagg, and Solanki, 2013; Lites, Centeno, and McIntosh, 2014), which implies that internetwork fields are probably created by small-scale dynamos driven by surface convection rather than the global dynamo mechanism. Such small-scale dynamos have been found in recent numerical simulations (Shelyag *et al.*, 2011; Rempel, 2014). In addition, small-scale vortex motions in the photosphere (Bonet *et al.*, 2008; Vargas Domínguez *et al.*, 2011) could be a driver of small-scale dynamos. Thus, studying granular- and subgranular-scale flows in the photosphere is important.

Abramenko *et al.* (2012) found that two categories of granules exist: regular-size and *mini*-size granules. They suggested that the mini-granules behave in a turbulent manner compared with their regular-size counterparts. Van Kooten and Cranmer (2017) analyzed the motions of bright points in a numerically simulated photosphere and concluded that mini-granules cause high-frequency motions and regular-size granules cause low-frequency motions. They further suggested that there might be more power observed in small-scale and high-frequency phenomena. However, obtaining the velocity fields at such a small scale is difficult with the current instruments.

One possible approach to derive the velocity fields smaller than the spatial resolution is to use spectral line broadening. Nesis *et al.* (1992) found an anti-correlation between the line width and the continuum intensity, suggesting that shocks are excited by collisions of supersonic horizontal flows. Rybák *et al.* (2004) postulated that the increase in a line-core intensity associated with the transient increase in line width indicates the heating induced by post-shock turbulence. However, Solanki *et al.* (1996) found that such anti-correlations can be created without any shocks by simulating granulation and studying synthesized spectral signatures especially in the disk center observation where the LOS is almost parallel to the vertical direction. Vitas *et al.* (2011) discovered with MHD simulations that supersonic flows can exist in the photosphere and they are preferentially directed to horizontal direction, indicating only the line broadening in limb observation can be a signature of shocks.

Furthermore, a Doppler velocity gradient along the LOS causes spectral line broadening as well. Gadun, Hanslmeier, and Pikalov (1997) performed 2-D hydrodynamic numerical simulations and calculated the spectral line widths of synthesized spectral lines. The simulated photosphere creates velocity gradients along the height direction, especially in the intergranular lanes. Moreover, the synthesized spectral lines exhibit a broad profile. Khomenko *et al.* (2010) measured the spatial distribution of the spectral line widths obtained with a filtergraph onboard a balloon-borne telescope (SUNRISE/IMaX; Barthol *et al.* 2011; Martínez Pillet *et al.* 2011). They found that the spectral line width becomes larger in intergranular downflow lanes and becomes very small at the boundary between a granule and an intergranular lane. They suggested that a LOS velocity gradient is one of the major causes of line broadening, although they did not have a spectral resolution enough to obtain a velocity gradient because of the filtergraph observation.

There has been little observational knowledge on the contribution made to broaden spectral line profiles by LOS velocity gradients, which is critical to investigate the small-scale velocity fields. Our objective is to determine spatial and temporal variations of the line broadening and LOS velocity gradients with spatial and spectral resolutions enough to resolve the granulation dynamics. These quantities can be effectively derived from spectroscopic observations. We analyzed the data obtained with the Solar Optical Telescope (SOT; Tsuneta *et al.* 2008) onboard the *Hinode* satellite (Kosugi *et al.*, 2007); this instrument is advantageous in providing stable spectroscopic observations with a high spatial resolution. In Section **??**, the observational data and the analysis methods are described. The results regarding spatial distributions and temporal evolutions are discussed in Section **??**. Furthermore, the relationship between line broadening and LOS velocity gradients and small-scale turbulent velocities is discussed in Section 3.4.

Table 3.1: Data sets

Data Set	Date	n_x	n_y	n_t	Δt	$(\delta I)_{\rm rms}$	$\delta v_{0.5}$	δFWHM
1	22 Nov. 2006	1024	1024	1	87 min	0.47%	0.03 km/s	1.3 mÅ
2	25 Aug. 2009	30	384	118	1 min	0.96%	0.06 km/s	2.7 mÅ
3	08 Nov. 2018	15	512	283	15 sec	1.0%	0.07 km/s	2.8 mÅ

3.2 Observation and Analysis

3.2.1 Instruments

We examined the spectropolarimetric data obtained with the Hinode-SOT. The SOT has an aperture of 50 cm, thereby attaining a diffraction-limited performance (Suematsu *et al.*, 2008; Shimizu *et al.*, 2008). The spatial resolution at 6300 Å is approximately 0.″3, which is equivalent to a distance of about 200 km on the solar surface. The Spectro-Polarimeter (SP; Lites *et al.* 2013) covers two neutral iron lines, namely, Fe I 6301.5 Å and 6302.5 Å, with a spectral sampling of 21.5 mÅ/pixel. These two lines arise from the same multiplet, and their sensitivities to the Zeeman effect are different. The line-spread function of the SP can be fitted well with a Gaussian shape (Lites *et al.*, 2013), which indicates that the spectral asymmetry caused by the instrumental effects can be neglected.

3.2.2 Data sets

Here, two types of data are examined: normal map, which includes a single slit-scan with a wide field-of-view (FOV), and the dynamic mode data, which repeats slit scans over a narrow FOV with high time cadence ($\lesssim$ 1 min). Because the target regions of all the observations are quiet regions near the disk center, the LOS direction is almost vertical to the surface. The data sets are represented in Table

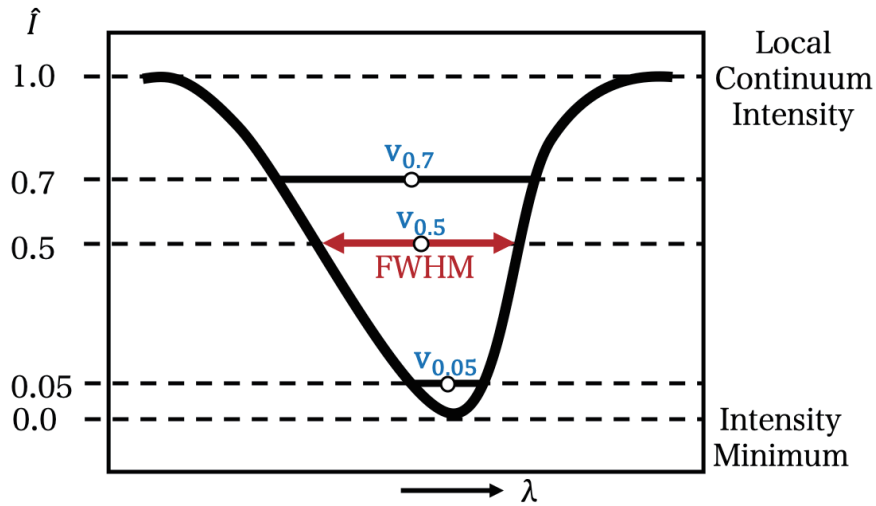

Figure 3.1: Definition of Doppler velocities obtained by bisector analysis. All the Doppler velocities are defined at specific intensity levels $\hat{I} = 0.05$, 0.50, and 0.70, where $\hat{I}$ is the intensity normalized by the local continuum intensity and the local minimum intensity of each spectral profile. FWHM is defined as the full width at the intensity level of $\hat{I} = 0.5$.

3.1.

The average root-mean-square fluctuation of the continuum intensity $(\delta I)_{\rm rms}$ provides a photometric error of the data. The pixel numbers n_x and n_y denote the FOV in the pixel scales, where the x and y axes correspond to the scan direction (East-West) and the slit direction (South-North), with a plate scales of $0''.15$ and $0''.16$, respectively. The number of scans in the dynamic mode is given by n_t, and Δt represents the duration of each scan.

These Stokes profiles are calibrated with the standard calibration routine `sp_prep` (Lites and Ichimoto, 2013). The `sp_prep` routine includes i) dark-field subtraction, ii) flat-field correction, iii) calibration of I, Q, U, and V crosstalk, iv) correction of curved spectral lines, v) removal of orbital variation of wavelength and spatial shifts caused by thermal deformation of instrument optics, and vi) calibration of intensity

variation along the SP slit caused by a small variation in slit width.

The zero-point of the Doppler velocity is adjusted using convective blueshift (Dravins, Lindegren, and Nordlund, 1981) of a spectral line profile averaged in each data set. The Doppler shift of the spatially averaged profile of the Fe I 6301.5 Å line was accurately determined by Löhner-Böttcher *et al.* (2018). They reported that the Doppler shift at the intensity level of $\frac{1}{2}\langle I_{\rm cont}\rangle$ is -290 m/s, where $\langle\cdot\rangle$ denotes the average over the entire FOV and $I_{\rm cont}$ is the continuum intensity at each pixel. We adjust the zero-point to make our Doppler velocity of the spatially and temporally averaged line profile at $\frac{1}{2}\langle I_{\rm cont}\rangle$ be equivalent to -290 m/s.

3.2.3 Definition of Parameters

The parameters studied in this paper are summarized in Table 3.2, where $\langle\cdot\rangle$ denotes the spatial and temporal average over both the entire FOV and the whole duration in each data set. All the parameters are calculated for the 6301.5 Å line, except for $P_{\rm tot}$. $I_{\rm c}$ is the continuum intensity normalized by the mean continuum intensity averaged over both the entire FOV and the whole duration, and $\hat{I}$ represents the intensity normalized by the local continuum and local minimum intensity at each pixel. A LOS dependence of a Doppler velocity can be estimated by applying bisector analysis (e.g. Adam, Ibbetson, and Petford 1976) to the spectroscopic data, by defining three Doppler velocities at $\hat{I} = 0.05$, 0.5, and 0.7, as $v_{0.05}$, $v_{0.5}$, and $v_{0.7}$, respectively (Figure 3.1). Bisector analysis is an appropriate method to extract the LOS velocity gradients from asymmetric line profiles. The bisector is the midpoint of the same intensity points of both sides of an absorption line. The Doppler velocity at different intensity levels defined by this bisector method reflects a LOS velocity at a different height. The Doppler velocities at $\hat{I} = 0.05$ and $\hat{I} = 0.7$ reflect the LOS velocities in the upper photosphere and the lower photosphere, respectively. The velocity difference Δv, which is a representative of a Doppler velocity gradient along the LOS, is defined as $v_{0.05} - v_{0.7}$. A positive Δv indicates strong blueshifts in the lower photosphere, whereas a negative Δv indicates strong redshifts in the lower photosphere. $\delta v_{0.5}$, an error of $v_{0.5}$, is estimated from $(\delta I)_{\rm rms}$ (see Appendix

D). We use the full width at $\hat{I} = 0.5$ (FWHM) as a representative of the spectral line broadening. In addition, we use the equivalent width (EW), which is a simple integration of the residual intensity. Finally, we use the total polarization ($P_{\rm tot}$) calculated by the `sp_prep` routine. $P_{\rm tot}$ reflects the polarization caused by the Zeeman effect (see Appendix E).

Table 3.2: Definitions of the parameters

parameter	definition
$I_{\rm c}$	$I_{\rm c} \equiv \frac{I_{\rm cont}}{\langle I_{\rm cont} \rangle}$
$\hat{I}$	$\hat{I} \equiv \frac{I - \min(I_\lambda)}{I_{\rm cont} - \min(I_\lambda)}$ (Equation [D.1])
$v_{0.05}$	Doppler velocity at $\hat{I} = 0.05$
$v_{0.5}$	Doppler velocity at $\hat{I} = 0.5$
$v_{0.7}$	Doppler velocity at $\hat{I} = 0.7$
Δv	$\Delta v \equiv v_{0.05}$ - $v_{0.7}$
FWHM	Full width at $\hat{I} = 0.5$
EW	$\mathrm{EW} \equiv \int \left(1 - \frac{I_\lambda}{I_{\rm cont}}\right) d\lambda$
$P_{\rm tot}$	$P_{\rm tot} \equiv \int \frac{\sqrt{Q_\lambda^2 + U_\lambda^2 + V_\lambda^2}}{I_{\rm cont}} d\lambda$

3.3 Results

3.3.1 Statistical Analyses of Spectral Line Broadening

Figure 3.2 shows the spatial distributions of $I_{\rm c}$, $v_{0.5}$, Δv, and FWHM. In the spatial distributions of $I_{\rm c}$ and $v_{0.5}$, cellular patterns related to the granulation can be clearly seen. The spatial distribution of Δv shown in Figure 3.2(c) clearly indicates that

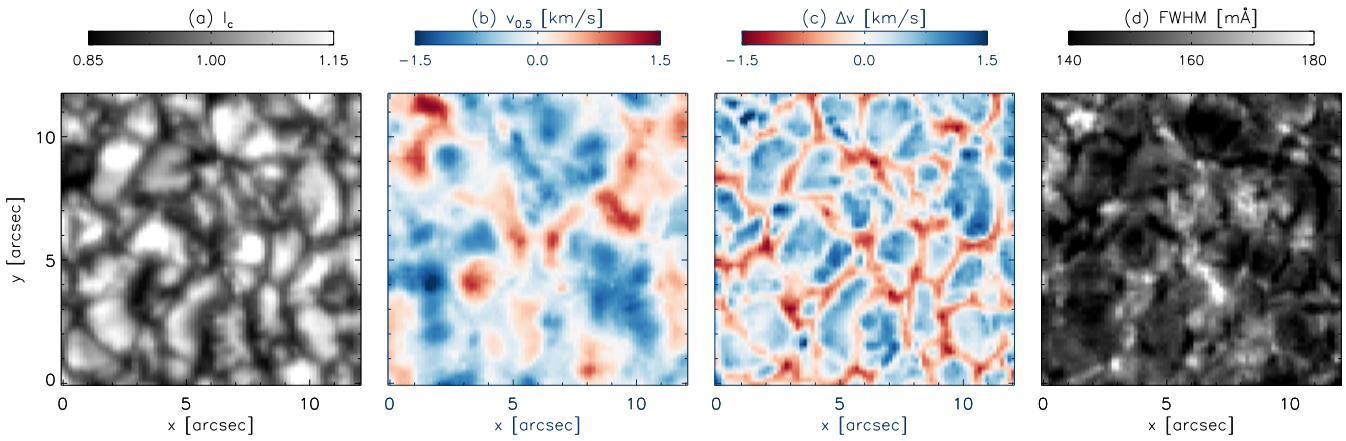

Figure 3.2: Spatial distributions of (a) continuum intensity I_c, (b) Doppler velocity $v_{0.5}$, (c) velocity difference Δv, and (d) FWHM of the Fe I 6301.5 Å line from data set 1.

Δv is positive within the granules, whereas it becomes negative in the surrounding intergranular lanes. On the contrary, the FWHM shown in Figure 3.2(d) exhibits less clear association with the granular structures. For example, large granules around $(x, y) = (2'', 2''.5)$ and $(x, y) = (7''.5, 10'')$ appear to have a small FWHM within the granules, whereas the FWHM are large toward the edges of the granules and in the intergranular lanes. This result is consistent with the results of previous studies (Gadun, Hanslmeier, and Pikalov, 1997; Hanslmeier *et al.*, 2008; Khomenko *et al.*, 2010). However, the relationship is not clear for small granules, e.g., around $(x, y) = (2''.5, 7'')$ and $(x, y) = (8'', 7'')$. Moreover, sporadic enhancements of FWHM are seen throughout the FOV.

Figure 3.3(a) shows a 2-D histogram of I_c versus FWHM for all pixels of the data set 1. The black line in Figure 3.3(a) indicates the average FWHM at each I_c. The trend of the black line indicates that FWHM becomes small in the middle of granules ($I_c > 1.0$), whereas it becomes large in intergranular lanes ($I_c < 1.0$). This trend is consistent with the trend reported by previous studies (Gadun, Hanslmeier, and Pikalov, 1997; Hanslmeier *et al.*, 2008; Khomenko *et al.*, 2010). Furthermore,

some pixels with $I_c \sim 1.0$ have a large FWHM and some with $I_c \sim 0.9$ have a small FWHM. The deviation of FWHM at each I_c is significantly larger than the estimated error of FWHM caused by the photometric noise of data set 1 (see Table 3.1 and Appendix D).

Figure 3.3(c) shows a 2-D histogram of I_c and Δv. Clearly, pixels with negative Δv exist in the intergranular lanes, which are caused by accelerated downflows; where the downward velocity becomes faster in the lower layer, as predicted by the numerical simulations performed by Gadun, Hanslmeier, and Pikalov (1997) and Asplund *et al.* (2000). On the contrary, pixels with positive Δv exist near the center of the granules. These signs of Δv are consistent with the overshooting convection, where deceleration of upflows occurs in the upper photosphere. In addition, pixels with strong positive Δv exist in the region with $I_c \sim 1.0$. Such strong positive Δv has never been indicated by both numerical and observational studies.

Previous studies have suggested that the spectral line broadening is caused by the LOS gradient of Doppler velocity (Gadun, Hanslmeier, and Pikalov, 1997). The relationship between Δv and FWHM is shown in Figure 3.4(a). The figure clearly indicates that large absolute values of Δv induce an increase of FWHM. The relationship shown in Figure 3.4(a) indicates a significant dispersion in FWHM, implying that another factor also causes line broadening.

It must be noted that the FWHM related to positive Δv is slightly larger than that of their negative counterparts, except for the regions where $P_{\rm tot}$ is large. The increase in FWHM related to a positive Δv of 1 km/s is approximately 15 mÅ on average, whereas that related to a negative Δv of -1 km/s is approximately 10 mÅ on average (Figure 3.4[a]).

We focus on the strongly magnetized regions to understand the effect of magnetic fields. Figure 3.3(b) shows the same histogram in panel (a), but for the pixels with strong magnetic flux. The threshold is defined by the total polarization: $P_{\rm tot} > 2.0\%$, which corresponds to magnetic flux larger than the equipartition magnetic flux of approximately 450 Mx/cm^2 (see Appendix E). Although the magnetic fields are likely to be concentrated in the intergranular lanes, the continuum intensity

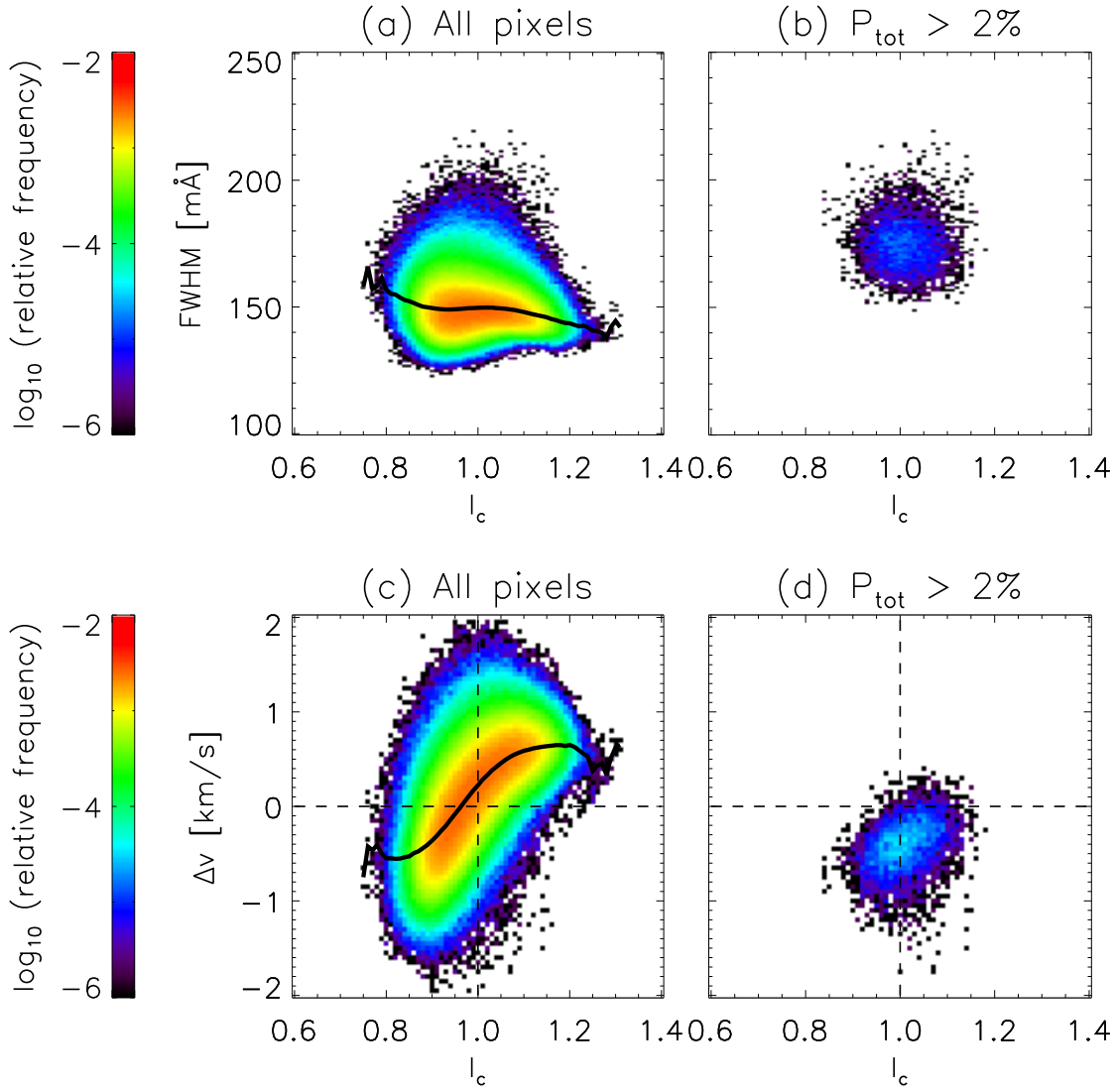

Figure 3.3: 2-D histograms of I_c and FWHM (panels [a] and [b]), and I_c and Δv (panels [c] and [d]), for all pixels in the FOV and the pixels with large P_{tot}. The P_{tot} of 2% corresponds to a magnetic flux of about 450 Mx/cm^2. The black lines in panels (a) and (c) indicate the average FWHM and Δv at each I_c. The color contours show the relative frequency in logarithmic scale. The histograms are obtained from the data set 1.

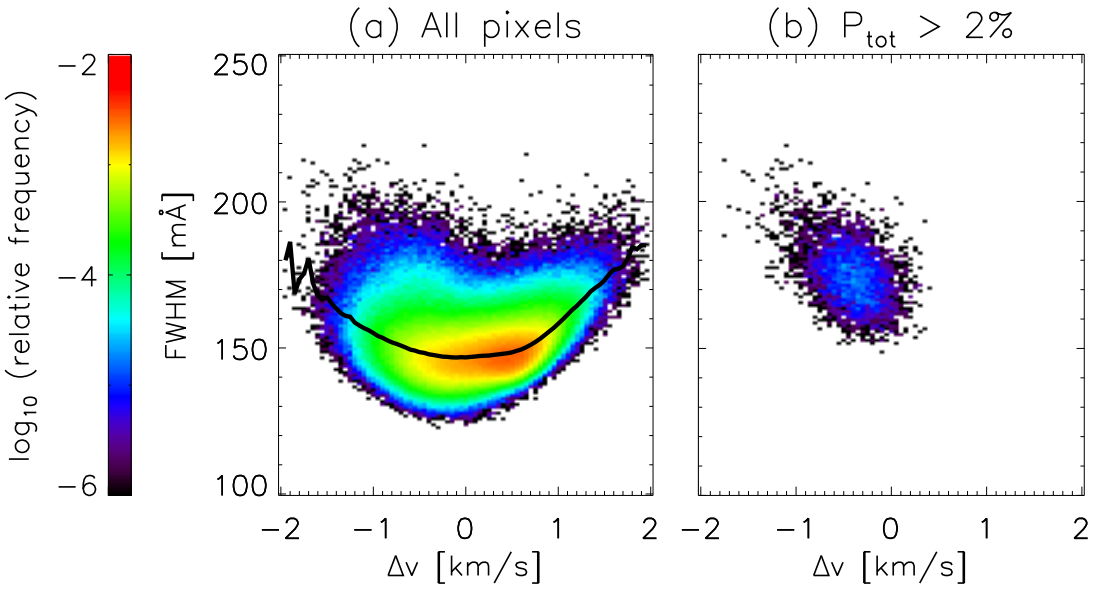

Figure 3.4: 2-D histograms of Δv and FWHM for all the pixels (a) and for those with large total polarization (panel [b]). The black line represents the average FWHM at each Δv. The color contours are the same as those in Figure 3.3. The histograms are obtained from the data set 1.

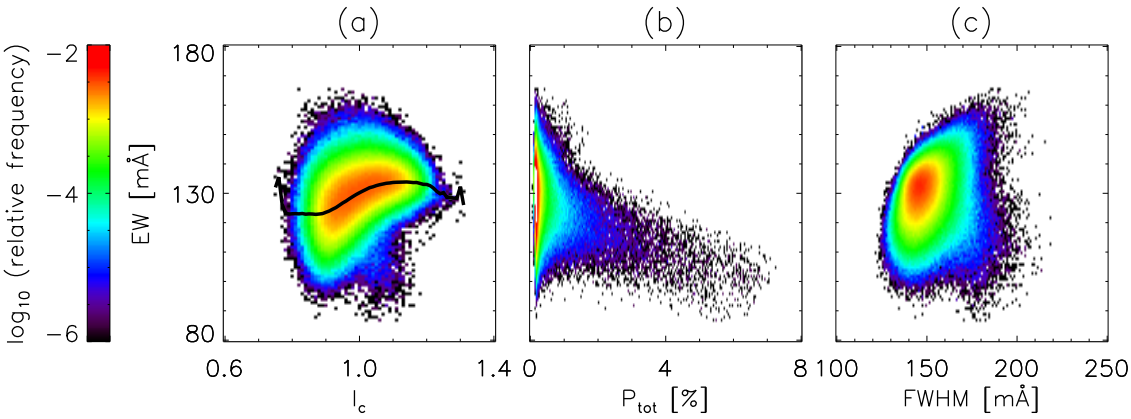

Figure 3.5: (a) Dependence of EW on I_c and (b) total polarization $P_{\rm tot}$, which is an agent of magnetic flux. Panel (c) shows the histogram of EW and FWHM. The color contours are the same as those in Figure 3.3. The histograms are obtained from the data set 1.

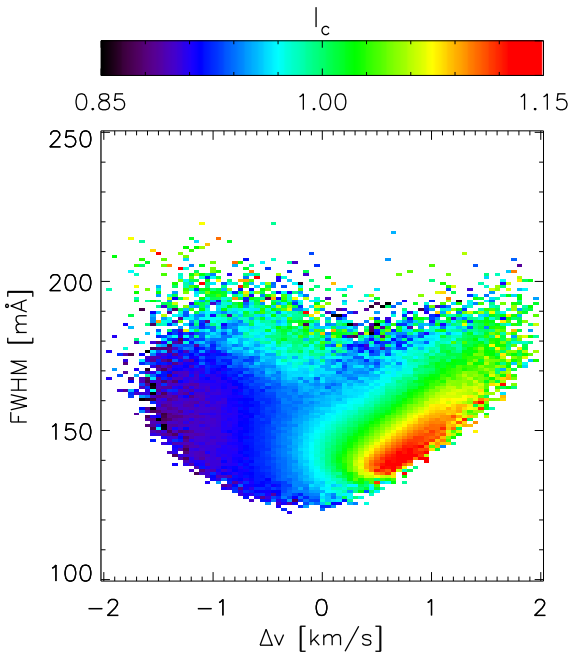

Figure 3.6: Relationship between Δv, FWHM, and I_c from the data set 1.

in the strongly magnetized region is brighter than that in the weakly magnetized intergranular lane (Figure 3.3[d]), because the photospheric surface observed by the continuum intensity moves downward because of the decrease in opacity caused by magnetic fields (Wilson and Maskelyne, 1774; Spruit, 1981). Figure 3.4(b) shows the same histogram in Figure 3.4(a) but for the strongly magnetized pixels ($P_{\rm tot} >$ 2%). The figure clearly indicates that the strongly magnetized pixels have large FWHM for negative Δv, but they are not associated with positive Δv.

The histogram of EW and I_c is shown in Figure 3.5(a). It can be seen that the EW are small in the intergranular lanes relative to those in granules. In addition, in the region of $I_c \sim 1.0$, the deviation of EW is large. Figure 3.5(b) shows the histogram of EW and $P_{\rm tot}$, which indicates that the magnetic flux decreases the EW. We confirmed that the pixels with small EW around $I_c \sim 1.0$ seen in panel (a) are associated with the strongly magnetized pixels. The strongly magnetized pixels

have small EW and large FWHM (Figure 3.5[b] and [c]). The pixels with large EW and $I_c \sim 1.0$ seen in panel (a) have large FWHM, which is clearly different from the properties of the strongly magnetized pixels.

Figure 3.6 shows the relationship between Δv (abscissa), FWHM (ordinate), and I_c (color contour), where the I_c of each bin is obtained by averaging I_c of all the pixels in each bin. Apparently, near the center of a granule ($I_c \gtrsim 1.1$; highlighted in red), Δv is positive at approximately 0.8 km/s, whereas it is negative at approximately -1.0 km/s in the downflow lane ($I_c \lesssim 0.9$; highlighted in dark blue). The strongly magnetized pixels are located in the region with $I_c \sim 1.0$ (highlighted in green) and $\Delta v < 0$, and have very large FWHM. Furthermore, the pixels with $I_c \sim 1.0$ are seen in the region with $\Delta v > 0$ as well. Some of them have large Δv and large FWHM, and some have $\Delta v \sim 0$ and small FWHM. The latter may correspond to the cellular boundary between granules and intergranular lanes, which was found by Khomenko *et al.* (2010).

3.3.2 Case Study

We examine three different samples in Figure 3.7, where the three columns on the left show the spatial distributions of I_c, FWHM, and P_{tot} (left to right). The rightmost column provides the bisectors at each pixel (indicated by cross symbols in the three columns on the left). The green and blue symbols represent samples of intergranular lanes and center of granules, respectively. The red symbols represent samples of pixels with large FWHM for sample 1 and sample 2, and show a pixel with strong magnetic flux for sample 3. The existence of large positive Δv accompanied by large FWHM without strong magnetic field is seen in samples 1 and 2. The pixels with large FWHM have I_c of almost unity, some of which are located at the boundaries between granules and intergranular lanes. The FWHM of such pixels are larger than those of the pixels in the intergranular lanes or near the center of granules by 30 mÅ to 40 mÅ; further, even P_{tot} are small. The velocity differences Δv obtained by the bisectors (red lines in the rightmost column of Figure 3.7) have large positive values compared with those of the other two (green and blue lines in the rightmost

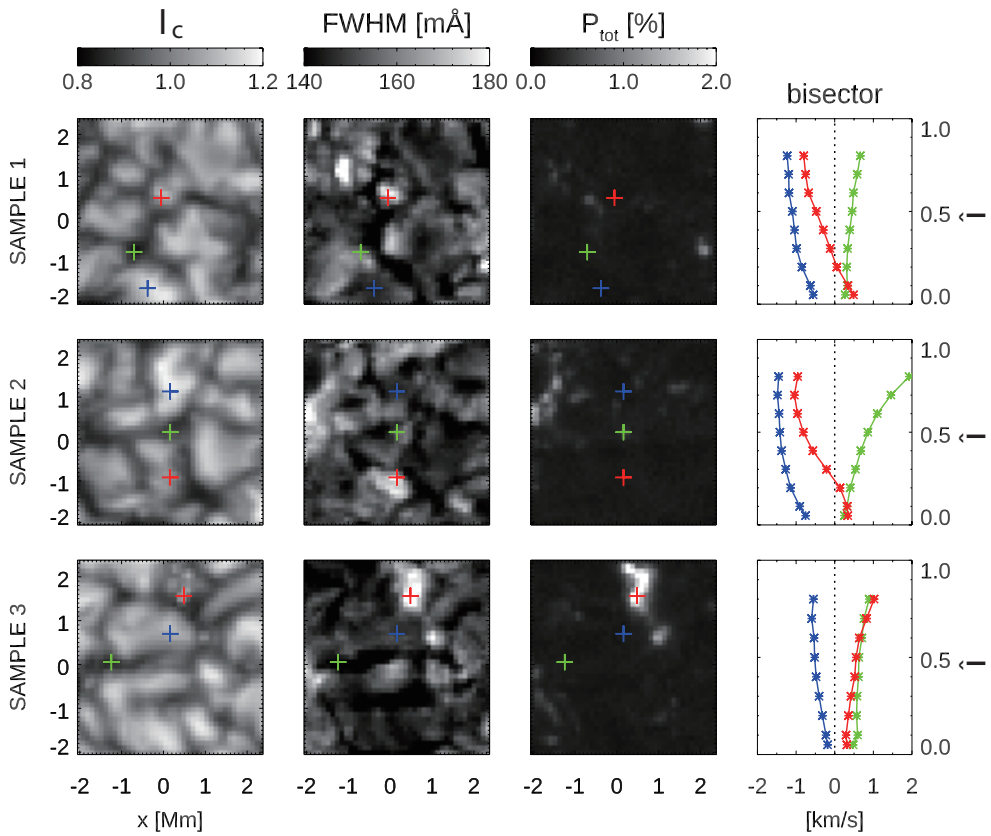

Figure 3.7: Three columns on the left show the spatial distributions of I_c, FWHM, and P_{tot} from left to right. The rightmost column provides the bisectors at each pixel indicated by cross symbols in the spatial distributions. We chose the bisectors in intergranular lanes (green), near the center of granules (blue), and in the region with large FWHM (red). Note that, in sample 3, the pixel denoted by the red cross symbol is in a region with strong magnetic flux. All the samples are extracted from the data set 1.

column).

Sample 3 shows the case of a strong magnetized region with large $P_{\rm tot}$, large FWHM, and large negative Δv. Although this magnetized region is located in an intergranular lane, it has a brighter intensity ($I_{\rm c} \sim 1.0$). This trend is the same as that shown in panels (b) and (d) in Figure 3.3.

In Sections 3.3.1 and 3.3.2, we analyzed the spatial distribution of FWHM and newly found the sporadic enhancements of FWHM with positivie Δv throughout the photosphere. It was also shown that the large dispersion of FWHM cannot be explained only by the LOS velocity gradient. To identify the cause of the sporadic line broadening, we analyze the temporal evolution in Section 3.3.3.

3.3.3 Temporal Evolution

We examine the temporal evolution of the granules in the data sets 2 and 3 to investigate development of positive Δv and broadening of spectral lines. Figures 3.8 and 3.9 show two samples of temporal evolution of granules. In this study, we focus on the fading phase of granules. The four rows on the top provide the temporal evolutions of $I_{\rm c}$, FWHM, Δv, and $P_{\rm tot}$ (top to bottom). The bottom left panel in Figure 3.8 shows the temporal evolutions of FWHM (black), $v_{0.5}$ (orange), $I_{\rm c}$ (red), and Δv (blue) at (x,y)=(0.6,1.1), where the center of the granule is located at t=225 s. This temporal evolution is plotted in the Δv-FWHM diagram (bottom right panel), where the red and blue diamonds denote the first (t=0 sec) and the final (t=420 sec) frames, respectively.

In the earlier phase of the sample shown in Figure 3.8 (from 0 s to 150 s), the continuum intensity does not vary significantly around $I_{\rm c} \sim 1.1$ and the upward flow becomes faster from -0.5 km/s to -1.5 km/s, enhancing the positive Δv and FWHM; subsequently, $I_{\rm c}$ starts decreasing. When Δv reaches the maximum, simultaneously, FWHM and blueshift of $v_{0.5}$ reach their maxima as well. Further, $I_{\rm c}$ starts decreasing from 1.10 to 0.85 within approximately 100 s, which we define as the fading phase. Finally, Δv and FWHM drop, and $v_{0.5}$ changes drastically from -1.5 km/s (blueshift) to +1.0 km/s (redshift). $P_{\rm tot}$ does not change significantly over this period.

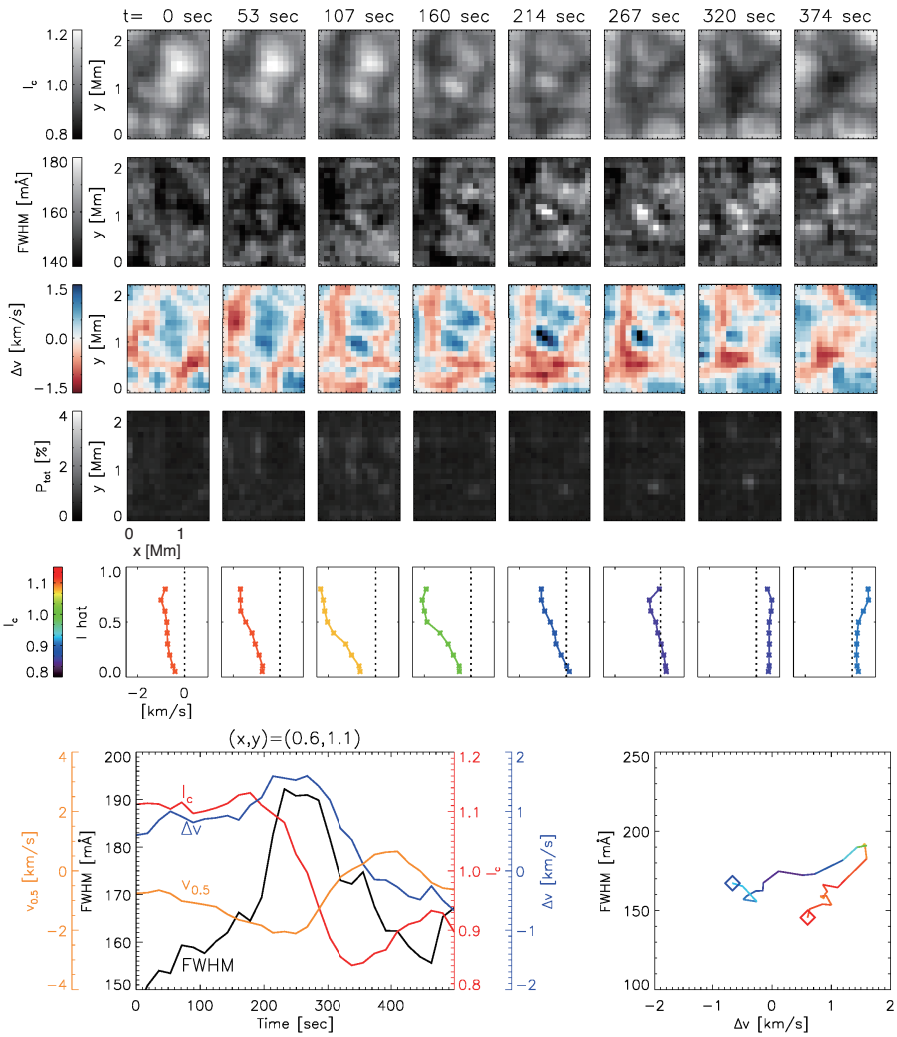

Figure 3.8: A sample of time evolution of a fading granule. Five rows on the top provide the temporal evolutions of I_c, FWHM, Δv, P_{tot}, and bisector velocities (from top to bottom), respectively. The bottom left panel shows the temporal evolutions of FWHM (black), $v_{0.5}$ (orange), I_c (red), and Δv (blue) of the fading granule at (x,y)=(0.6,1.1). This temporal evolution is plotted in the Δv-FWHM diagram (right bottom panel) with color-coding according to the continuum intensity I_c (same as that in Figure 3.6), where the red and blue diamonds denote the first frame ($t = 0$ sec) and the final frame ($t = 420$ sec), respectively. This sample is extracted from the data set 3.

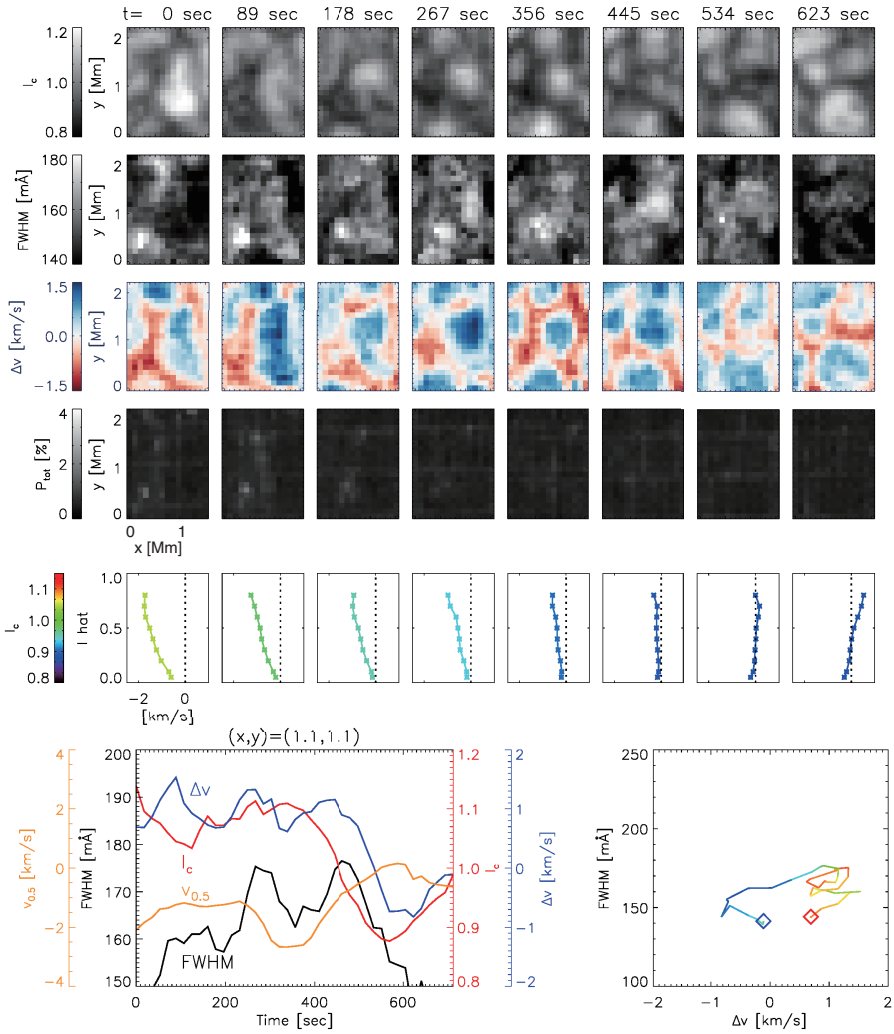

Figure 3.9: Same figure as Figure 3.8 but for another sample. Note that this sample granule takes a longer period to fade out than that in Figure 3.8. This sample is extracted from the data set 3.

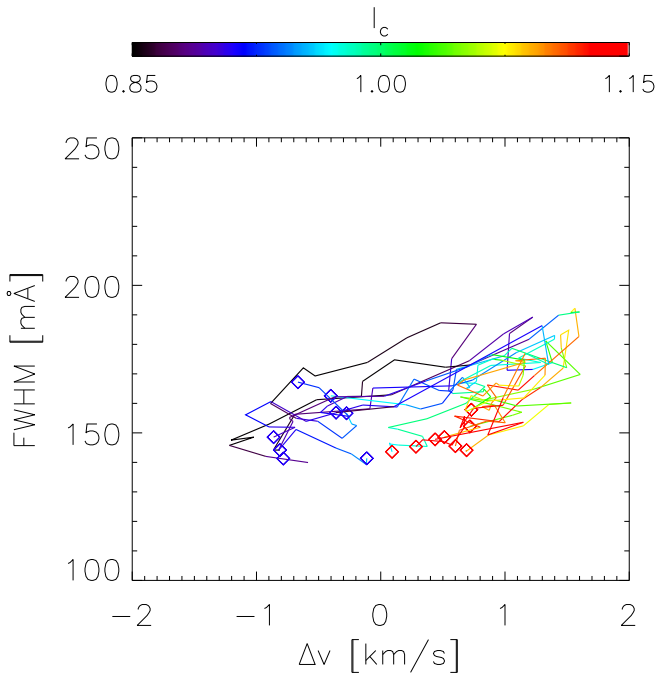

Figure 3.10: Time evolutions of eight sample granules. Comparison with Figure 3.6 is useful. One sample is from the data set 2 and the other samples are from the data set 3. The samples shown in Figures 3.8 and 3.9 are included as well.

Another sample of a fading granule is given in Figure 3.9. The increase in FWHM takes a longer period than that of the sample in Figure 3.8, and the decrease of I_c takes approximately 150 s. In the earlier phase, I_c does not change significantly for approximately 400 s. Although the positive Δv does not increase, the FWHM increases; this increase cannot be explained only by the velocity gradient. Finally, I_c, FWHM, and Δv drop, and $v_{0.5}$ changes its sign; P_{tot} does not vary so much over this period again.

In both the samples, if we plot the temporal evolution in the Δv-FWHM diagram, it begins from bottom right (Δv >0 and small FWHM) and proceeds to top right (Δv >0 and large FWHM), and finally drops to bottom left (Δv <0 and small FWHM). Combining this temporal evolution with Figure 3.6, we can confirm that

the regions with $\Delta v > 0$ and large FWHM (top right domain in the Δv-FWHM diagram in Figures 3.8 and 3.9) are preferentially seen in the fading phase of granules. It is worth to note that the number of pixels that have FWHM larger than 160 mÅ and $\Delta v > 0$ (right top domain) is 6% of the entire FOV of the normal map data, while the number of pixels with FWHM > 160 mÅ is 10%.

Figure 3.10 shows eight samples of fading granules in the Δv-FWHM diagram. It is clearly seen that the FWHM and Δv of all the samples become large, approximately when I_c becomes almost unity in the fading phase of granules. As a granule fades out, Δv decreases and changes its sign. The FWHM is larger than that in the earlier phase even when Δv is almost zero. This demonstrates that the increase in FWHM is caused by another effect rather than the velocity gradient, which is discussed later in Section 3.4.3.

3.4 Summary & Discussion

3.4.1 Summary of the Observation

We examined both the normal map data and the dynamic mode data obtained with Hinode-SOT and investigated the nature of spectral line broadening by analyzing the velocity difference Δv and FWHM of the spectral line profiles. Further, positive Δv exists, indicating strong blueshifts in the lower atmospheric layer; the existence of negative Δv indicates strong redshifts in the lower layer. We confirmed that spectral line broadening is induced by the velocity gradient. As suggested by the numerical simulations, the downward velocity is higher in the lower layer in the intergranular lanes, and this velocity gradient increases the FWHM, whereas the boundaries between granules and intergranular lanes have small FWHM because of small velocity gradients. We confirmed these characteristics observationally, by analyzing the spectroscopic data with a high spatial resolution.

We newly found that the regions with large positive Δv have I_c of almost unity and very large FWHM, some of which are seen in the fading phase of the granules.

Some regions with negative Δv are associated with strong magnetic flux. On the contrary, no clear relationship is observed between positive Δv and magnetic flux.

3.4.2 Spectral Line Broadening caused by Velocity Gradients

The velocity gradient in intergranular lanes, where stronger downward flows occur in the lower atmosphere, have already been studied. In this study, we find the significant velocity gradients associated with fading granules, where gas moves upward in the lower atmosphere and downward in the upper atmosphere. When a granule fades out, the gas in the upper layer could start descending earlier than that in the lower layer because the gas in the upper layer is cooled by radiation earlier than that in the lower layer, giving rise to a large velocity gradient. The velocity gradients in the intergranular lanes and the fading granules have different signs; however, both increase the spectral line widths (Figure 3.4[a]). The fading granules are mostly located in the less-magnetized regions, and the spectral line broadening has no clear association with the magnetic flux. This implies that the line broadening seen in the fading granules is not caused by the Zeeman effect.

3.4.3 Spectral Line Broadening caused by Turbulent Motions

Even when Δv is almost zero, large dispersion is seen in FWHM in Figure 3.4(a). By attributing this dispersion of FWHM to microturbulent velocity, we can estimate the average microturbulent velocity. Given that the spectral line profiles with $\Delta v = 0$ have Gaussian shapes, we can model the line broadening due to the turbulent velocity as follows, since the broaden spectral line profile is equivalent to the convolution of a narrow line profile without turbulent velocity and the Gaussian kernel of turbulence.

$$\sqrt{\overline{\mathrm{FWHM}}^2 - \left(\overline{\mathrm{FWHM}} - \sigma_{\mathrm{FWHM}}\right)^2} = 2\sqrt{2\ln 2}\frac{\overline{v_t}}{c}\lambda \tag{3.1}$$

where σ_{FWHM}, $\overline{\mathrm{FWHM}}$, λ, and c represent the standard deviation of FWHM at $\Delta v =$ 0 km/s in Figure 3.4(a), average FWHM at $\Delta v = 0$ km/s of 147 mÅ, wavelength of 6301.5 Å, and the speed-of-light, respectively. The average turbulent velocity $\overline{v_{\mathrm{t}}}$ is estimated at 0.9 km/s using the equation (3.1).

As mentioned in Section 3.3.1, a difference between the spectral line broadenings exists; positive Δv increases the FWHM by a larger degree than negative Δv. This difference can be attributed to the relationship between turbulent motions and velocity gradients. When I_{c} becomes almost unity in the fading phase of granules, the gas moves downward along with a decrease in its volume, and the surrounding gas converges into the fading granule. In addition, the positive Δv in the fading granules corresponds to upward motions in the lower layer and downward motions in the upper layer, which may cause a strong shear of vertical flows, potentially making the gas more turbulent. As shown in Figure 3.10, when the granules fade out, the FWHM is larger than that in the earlier phase even if Δv is almost zero, which implies that the turbulent motions probably develop in the fading granules.

3.4.4 Remaining Issues

In this chapter, we estimated the approximate Doppler velocity gradient by the bisector analysis. Evaluating the turbulent velocity, considering temperature and velocity gradients, using a spectral line inversion such as SIR (Ruiz Cobo and del Toro Iniesta, 1992) is important to get a more reliable result. A 4-m solar telescope named Daniel K. Inouye Solar Telescope (DKIST;Rimmele *et al.* 2020; Rast *et al.* 2021) is expected to begin its observation soon. The DKIST has an extremely high spatial resolution, which enables us to resolve small-scale complex structures in the photosphere. The line broadening and the turbulent motions reported in this paper should be investigated with such high-resolution observations.

Chapter 4

Origin of the line broadening associated with the fading granule

4.1 Introduction

In chapter 3, we found that the spectral line broadening appears in spatially localized regions with using the Hinode-SOT/SP. Some of them were associated with the fading process of granules. Velocity difference between the upper and lower photosphere was enhanced in the fading phase and simultaneous line broadening was observed, while this excess line broadening was still seen after the velocity difference was resolved. We concluded that these line broadening cannot be explained only by the Doppler velocity gradient obtained with the bisector analysis, which could be attributed to small-scale fluctuations of LOS velocity that is driven by the granulation.

On the other hand, there is a limitation of estimating the Doppler velocity gradient by using the bisector analysis. The Hinode solar optical telescope observes two neutral iron lines 6301.5 Å and 6302.5 Å. The bisector analyses only analyze the 6301.5 Å line and use the two bisector velocities to calculate the velocity difference between the lower and upper photosphere, providing a rough estimation of velocity gradient along the LOS. To discuss the origin of the line broadening quantitively, we

have to evaluate the contribution by the LOS gradients of temperature and velocity to the line broadenin by analyzing the entire profiles of the spectra based on the radiative transfer. Therefore we perform spectral line inversions to determine the detailed atmospheric structures in the granulation.

A key parameter to explain the spectral line broadening is microturbulence. The microturbulence term is a parameter that models the small-scale variation of LOS velocity. The probability density function of such small-scale velocities is assumed to obey Gaussian distribution with an average of zero. Only the standard deviation of this Gaussian is a free parameter for the microturbulence, determining the symmetric Doppler broadening.

It is still an open question if the microturbulence term is necessary for recent observation with a high spatial resolution. Some previous studies inverted photospheric spectral lines without the microturbulence term for the quiet region for the 6302 Å lines Quintero Noda *et al.* (2014) and moat region for the Fe I 6302 Å and 15650 Å and Ti I 6303 Å lines Bellot Rubio and Beck (2005), while some studies used it for the quiet region for the 6302 Å lines López Ariste, Martínez González, and Ramírez Vélez (2007); Quintero Noda, Ruiz Cobo, and Orozco Suárez (2014), and the Fe I 5250 Å line Guglielmino *et al.* (2020). As shown in Figure 3.3, large FWHM can be oberved in magnetic elements. By considering the PSF of the Hinode-SOT/SP, Buehler *et al.* (2015) concluded that these wide line profiles are originated not in the magnetic elements but in the vicinity of them, and microturbulence velocity of about 5 km/s is necessary to explain the wide profiles. By using the microturbulence term, inversion can explain the line broadening caused by turbulent flows which are spatially unresolved, and the line profiles are likely to be fitted better since the number of free parameters increases. However, we have to be careful of the degeneration among the microturbulence and other physical parameters such as temperature and Doppler velocity.

4.2 observation

We analyzed two types of data as listed in table 4.1: the normal map which includes a single slit-scan with a large FOV, and the dynamic mode data which repeats slit scans over a narrow FOV with a time cadence of 17.8 sec. These are the data as data No.1 and 3 investigated in Chapter 3 (see Table 3.1). The average root-mean-square fluctuation of the continuum intensity σ_I in table 4.1 provides an expected photometric error of the data, which was evaluated in the wavelength range from 6301.83 Å to 6302.17 Å, where the continuum spectra between the two iron lines are observed. The pixel numbers n_x and n_y denote the FOV in the pixel scales, where the x and y axes correspond to the scan direction (East-West) and the slit direction (South-North), with plate scales of $0''.15$ and $0''.16$, respectively. The number of scans in the dynamic mode is given by n_t, and Δt represents the duration of each scan.

Table 4.1: Data sets we used. The normal map data is same as the data No.1 in Table 3.1, and the dynamic mode data is same as the data No.3 in Table 3.1.

Obs. mode	Date	n_x	n_y	n_t	Δt	σ_I	δFWHM
Normal map	22 Nov. 2006	1024	1024	1	87 min	0.83%	1.3 mÅ
Dynamic mode	08 Nov. 2018	15	512	283	15 sec	1.0%	2.8 mÅ

4.3 Inversion Method

In this chapter, we perform spectral line inversion by using the SIR code (Stokes Inversion based on Response function; Ruiz Cobo and del Toro Iniesta 1992). SIR code can fit the observed spectra with 1-dimensional atmosphere. Response function $\boldsymbol{R}_\xi$ is based on a first-order perturbative analysis of the radiative transfer equation for polarized light (Landi Degl'Innocenti and Landi Degl'Innocenti, 1985; Sanchez

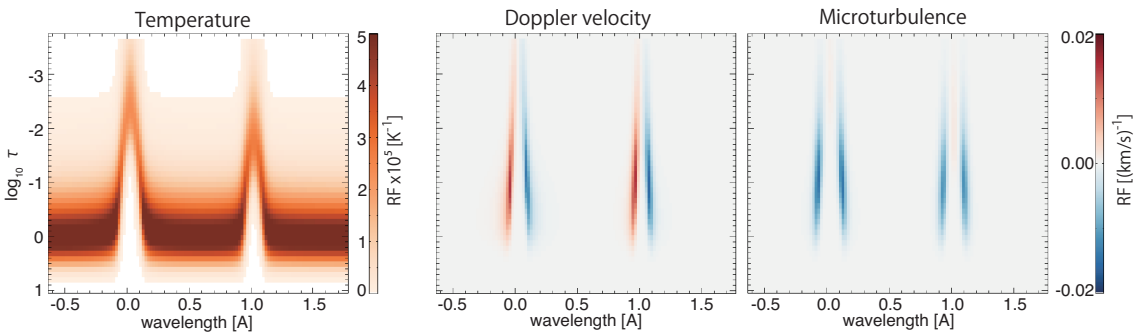

Figure 4.1: Examples of response functions for the temperature (left), Doppler velocity (center), and microturbulence (right) for the Fe I 6301.5 Å and 6302.5 Å lines. The definition is described in Eq (4.1).

Almeida, 1992) and is defined as

$$\delta \boldsymbol{I}(\lambda) = \int_0^\infty \boldsymbol{R}_\xi(\lambda, \tau)\delta\xi(\tau)d\tau, \tag{4.1}$$

where $\delta\xi(\tau)$, τ, and $\boldsymbol{I}$ are a perturbation of a physical quantity, optical depth at 5000 Å, and the stokes profiles normalized with the average continuum intensity, respectively (Landi Degl'Innocenti and Landi Degl'Innocenti, 1977). As described in Appendix A, the response function represents the linear relationship between the perturbation and corresponding small change of the emergent Stokes spectra $\boldsymbol{I}(\lambda)$. Figure 4.1 shows examples of response functions for the temperature, Doppler velocity, and microturbulence for the Fe I 6301.5 Å and 6302.5 Å lines. The continuum intensity reflects the temperature at around $\log\tau = 0$, and the lines have a sensitivity to the temperature from $\log\tau = 0$ to $\log\tau = -3$. The lines are also sensitive to the Doppler velocity and microturbulence at around $\log\tau = -1$.

In order to investigate the existence of small-scale turbulent motions, we invert the observed line profiles both with and without microturbulence and compare the results. The number of nodes of the inversions is listed in Table 4.2. The optical depths at which perturbations are sought are determined only by the number of nodes, and nodes are logarithmically equally spaced. In this study, we

Table 4.2: Number of nodes for the inversions

	With microturbulence	Without microturbulence
Temperature	5	5
Doppler Vel.	5	5
microturbulence	0	1
N_n	10	11

consider the atmosphere from $\log\tau = 1.0$ to $\log\tau = -3.8$, putting the nodes at $\log\tau = 1.0, -0.2, -1.4, -2.6, -3.8$ for the temperature and the Doppler velocity. After the perturbations are introduced to the parameters at each node, they are interpolated with cubic-spline functions. In the inversion without microturbulence, the microturbulence term is fixed with 0 km/s, while it is a free parameter but assumed to be constant along the LOS in the inversion with microturbulence. The line-spread-function of the Hinode-SOT/SP (Lites *et al.*, 2013) is considered.

The inversion is done only for the Stokes I spectra and the magnetic field strength is assumed to be zero, since the region we focus on has small total polarization $P_{\rm tot} < 1.6\%$ that is evaluated by the `sp_prep` routine (Lites and Ichimoto, 2013). Goodness of the fitting is evaluated with a reduced χ^2 defined as

$$\chi^2 \equiv \frac{1}{N_\lambda - N_n} \sum_{\lambda_i=1}^{N_\lambda} \left| \frac{I_{\rm obs}(\lambda_i) - I_{\rm fit}(\lambda_i)}{I_{\rm c}\sigma_I} \right|^2 . \tag{4.2}$$

Here N_λ, N_n, and σ_I indicate the number of pixels for the wavelength, the number of the free parameters, and the photometric error of the observed spectra, respectively.

The SIR code performs the Levenberg-Marquardt algorithm to find the solution that minimize the χ^2, by calculating the derivative of χ^2 with the response function. However it still have a dependence of the inversion results on the initial parameters and the solution is trapped in a local mininum. To avoid such dependence, we invert each spectrum 2500 times with different random initial guesses and

adopt the inversion result which achieves the minimum χ^2. The initial values of temperature range ±1500 K from the Harvard-Smithsonian reference atmosphere (HSRA;Gingerich *et al.* 1971) at each node, those of Doppler velocity from -2 km/s to 2 km/s at each node, and those of microturbulence from 0 km/s to 2 km/s.

4.4 Inversion Results

4.4.1 Narrow spectra

Figures 4.2 and 4.3 show the invertion results for a granule and an intergranular lane with and without the microturbulence. Both cases are extracted from the normal map data. Near the center of granules and the intergranular lanes, both the inversion with and without microturbulence can reproduce the observed spectral line profiles, and the estimated atmospheres and corresponding χ^2 values are quite similar. The inverted microturbulent velocities are zero for both cases. The microturbulence term is not necessary for the atmosphere in granules and intergranular lanes.

4.4.2 Wide spectra

To reveal the line broadening mechanism related to the granulation, we analyze two fading granules observed in the dynamic mode data. Observed spectra in both fading granules have wide spectral line profiles and small $P_{\rm tot} < 1.6\%$. Owing to the small polarization, the line broadening of these spectra should not be caused by the magnetic flux.

Figure 4.4 shows the first case we analyze, which is the same event shown in Figure 3.8. The top three rows show the temporal evolution of the bisector parameters during the fading process of the granule: normalized continuum intensity ($I_{\rm c}$), spectral line widths (FWHM), and the velocity difference between upper and lower photosphere (δv) defined in table 3.2. Line broadening is seen near the center of the FOV. Lower panels in Figure 4.4 show the inversion results for the center of the fading granule at $(x, y) = (0.6, 1.1)$ Mm at $t = 231$ sec. The Fe I 6301.5 Å

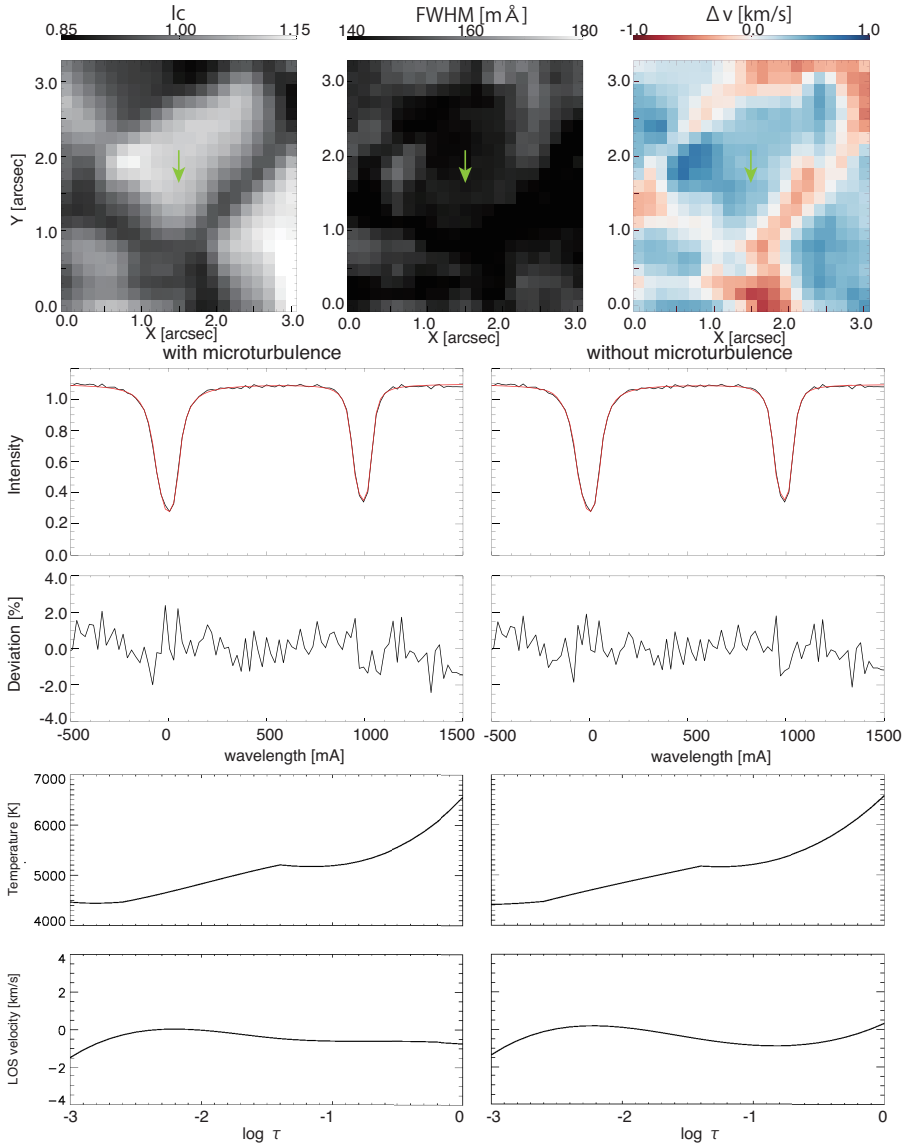

Figure 4.2: Granule and the inversion results with and without micro-turbulence term. Top: The spatial distributions of the continuum intensity, FWHM, and Δv. Bottom: The inversion results at $(x, y) = (1.5, 1.6)$ arcsec with (left) and without (right) microturbulence: (from top to bottom) observed (black) and fitted (red) spectra, the deviation between the observed and fitted spectra, the inferred temperature, and the inferred LOS velocity. The reduced χ^2 values are 1.00 with microturbulence and 1.13 without microturbulence.

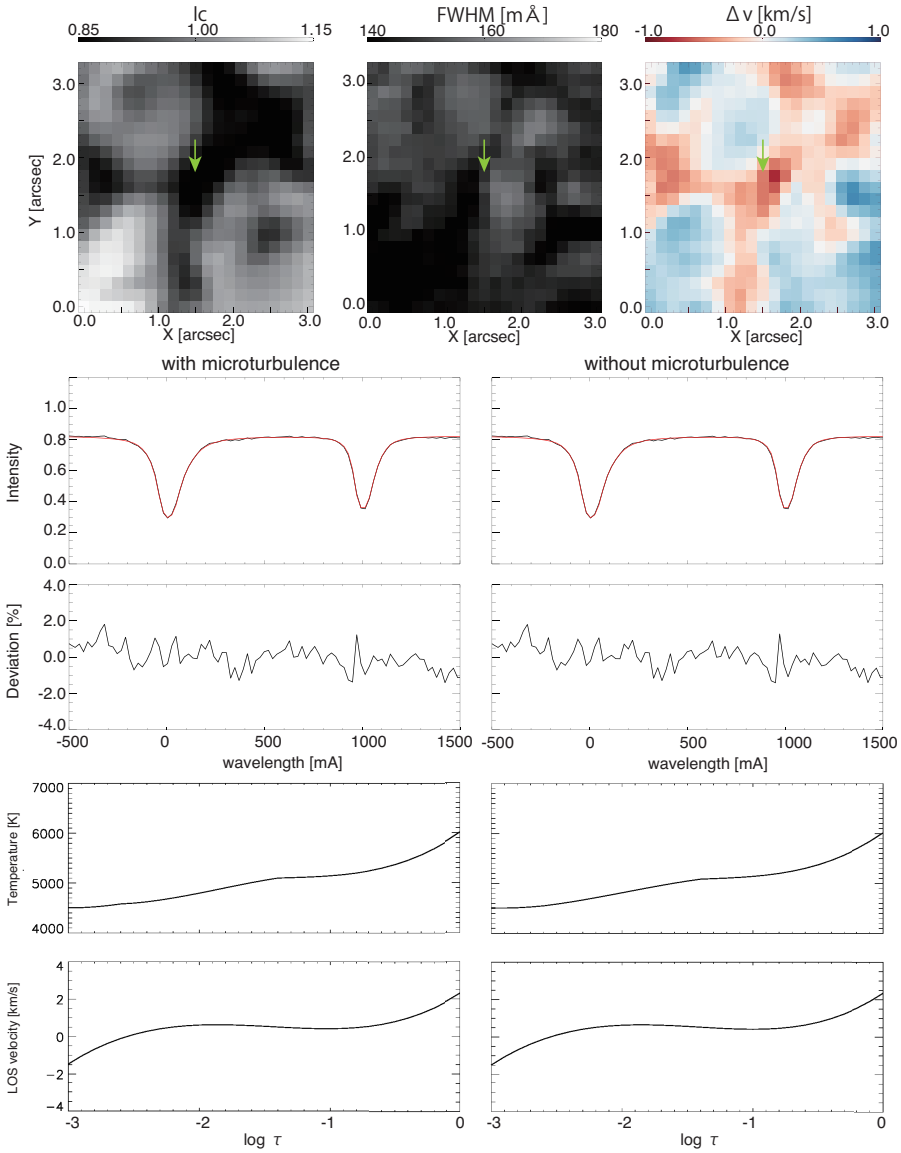

Figure 4.3: Intergranular lane and the inversion results with and without microturbulence term. Top: The spatial distributions of the continuum intensity, FWHM, and Δv. Bottom: The inversion results at $(x, y) = (1.5, 1.8)$ arcsec with (left) and without (right) microturbulence. The reduced χ^2 values are 0.79 with microturbulence and 0.78 without microturbulence.

line profile at this pixel has FWHM of 192 mÅ and Δv of 1.56 km/s. Both the inversions with and without microturbulence successfully reproduce the observed spectral line profiles with the χ^2 of 1.34 with microturbulence and 1.42 without microturbulence. However, the estimated atmospheres are completely different. The inversion with microturbulence obtains the atmosphere with the microturbulent velocity of 1.3 km/s, while the result without microturbulence needs large gradients of the temperature and Doppler velocity to reproduce the wide spectral line width.

Figure 4.5 shows the spatio-temporal variations of the bisector parameters around a fading granule and those of the inversion results both with and without the microturbulence term. The standard deviation of Doppler velocity is calculated from $\log \tau = -0.5$ to -2.5. This standard deviation represents the velocity gradient on large scales. This is because that the small-scale velocity variation cannot be detected due to the interval of the locations of nodes of $\Delta(\log \tau) = 1.2$ in the inversion.

The spatial distributions of inversion results seem not to be smooth. One reason is that the broad spectra are observed in a local region, which is indicative of small-scale variations of physical quantities. In addition, the χ^2 values fitted with and without microturbulence are similar to each other: even with microturbulence, the inversion sometimes adopts the large-gradient scenario to explain the line broadening with a small microturbulence. Buehler *et al.* (2015) executed an iterative method with spatially smoothing and obtained smooth results. However, this method is not justified in such localized events.

Another line broadening event associated with a fading granule is shown in Figure 4.6 detected in the dynamic mode data. Also in this event, both the inversion scenario can reproduce the observed spectra, estimating largely different atmospheric structures. The inversion with microturbulence obtains the atmosphere with the microturbulent velocity of about 1.4 km/s, while the result without microturbulence needs large gradients of the temperature and Doppler velocity to reproduce the wide spectral line width.

Figure 4.7 shows the scatter plot of the FWHM and the inferred microturbulent velocities in the regions near the fading granules shown in Figures 4.5 and 4.6. Color

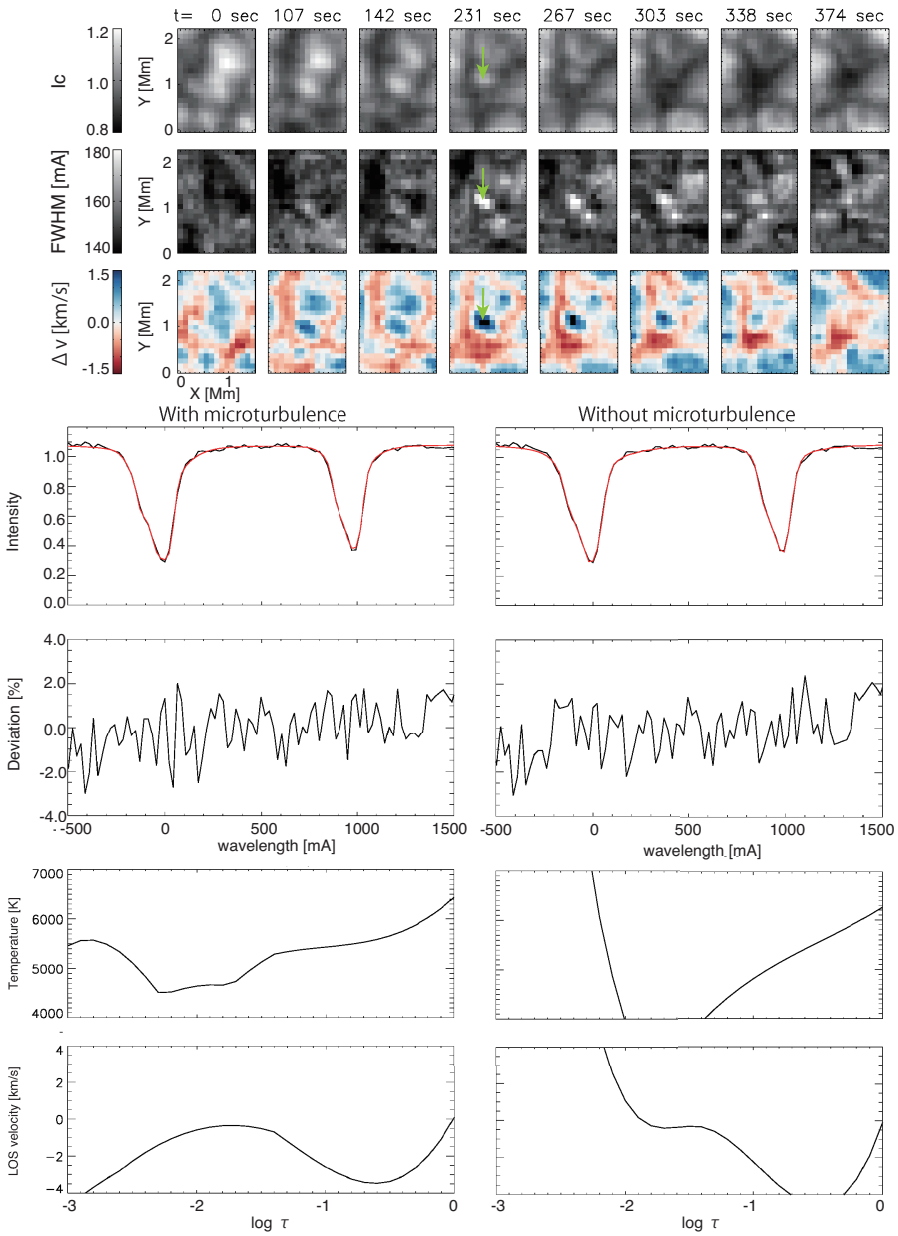

Figure 4.4: The temporal evolution of a fading granule (same as Figure 3.8). The observed spectrum and the inversion results at (x,y)=(0.6, 1.1) Mm at t=231 sec are also shown. The observed Fe I 6301.5 Å spectrum has FWHM of 192 mÅ and Δv of 1.56 km/s. Bottom left panels show the inversion results with microturbulent velocity, inferring the microturbulent velocity of 1.3 km/s. Bottom right panels show the results without microturbulent velocity. The reduced χ^2 values are 1.34 with microturbulence and 1.42 without microturbulence.

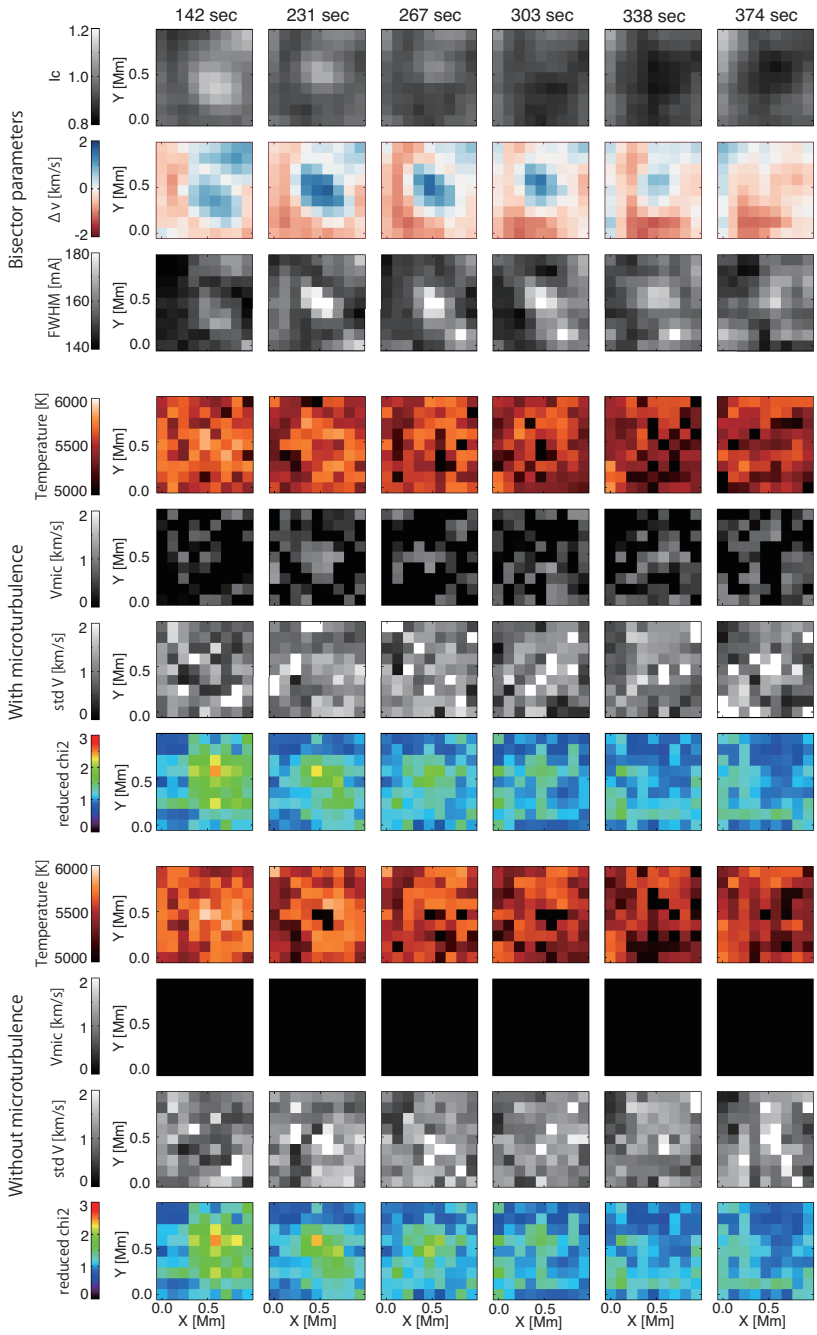

Figure 4.5: The temporal evolution of a fading granule same one as shown in Figure 4.4 but the FOV is small. Top three rows show the spatio-temporal variations of the normalized continuum intensity I_c (top row), bisector velocity difference Δv (middle row), and the FWHM of Fe I 6301.5 Å line (bottom row). Middle four rows show the inversion results with the microturbulence term. Bottom eight rows show the inversion results with and without microturbulence term. Temperature at $\log \tau = -1$, the microturbulence velocity, standard deviation of LOS velocity, and the reduced χ^2 are shown from top to bottom.

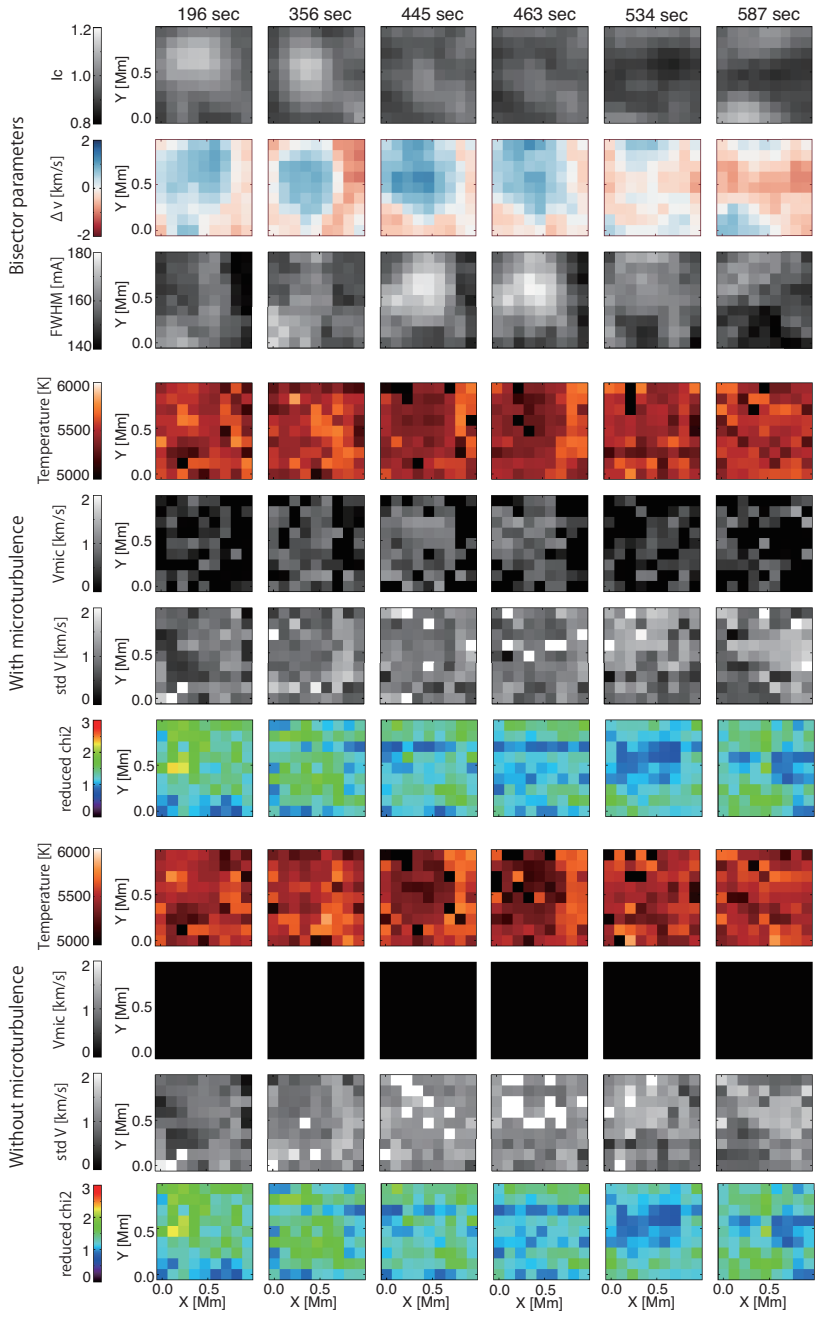

Figure 4.6: The temporal evolution of a fading granule (same as Figure 3.9). Top three rows show the spatio-temporal variations of the normalized continuum intensity I_c (top row), bisector velocity difference Δv (middle row), and the FWHM of Fe I 6301.5 Å line (bottom row). Bottom eight rows show the inversion results with and without microturbulence term.

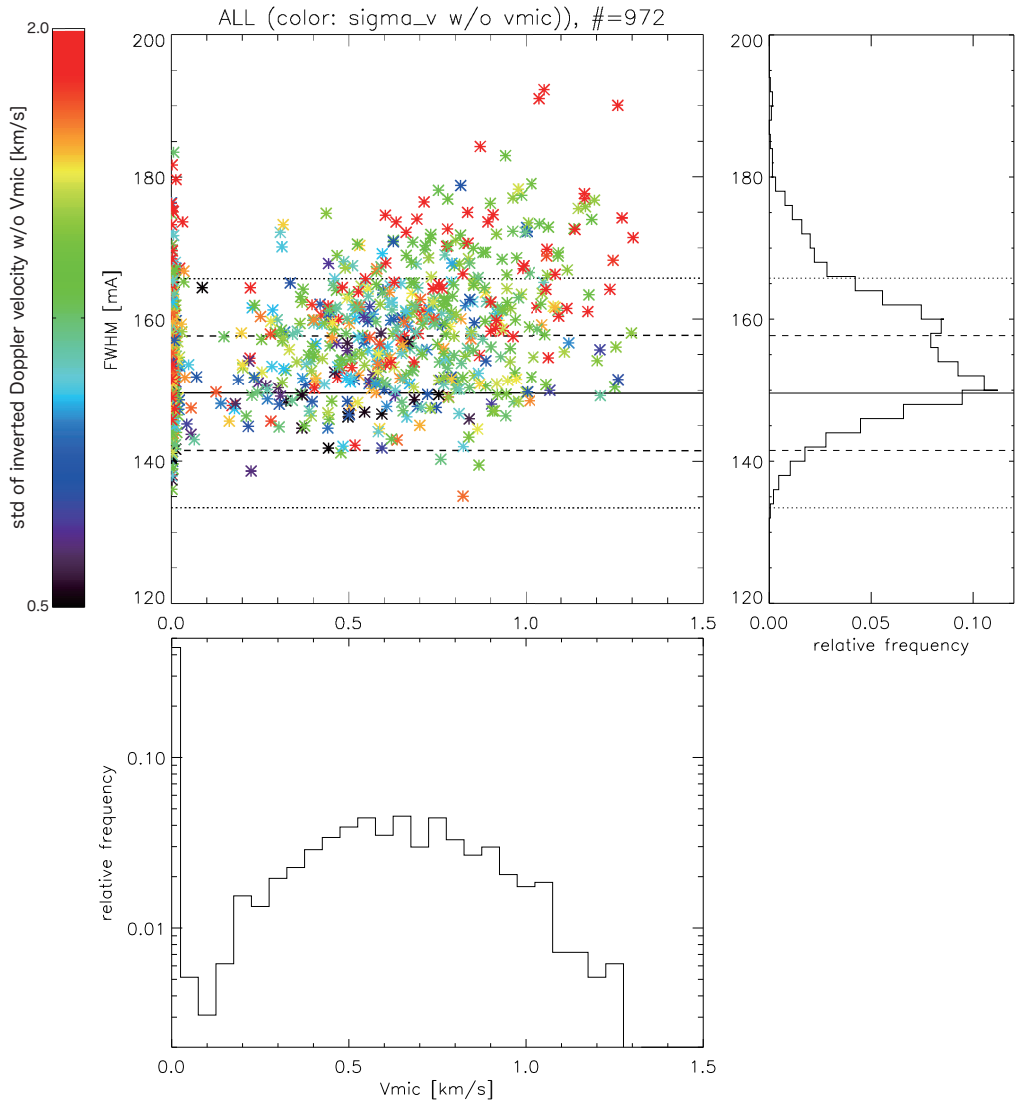

Figure 4.7: Scatter plot of FWHM and the inverted microturbulent velocity of the local regions around fading granules shown in Figures 4.5 and 4.6. The color shows the standard deviation of the Doppler velocity at each pixel inferred by the inversion without microturbulence. The solid line shows the average FWHM measured with the normal map data. Dashed and dotted lines indicate the FWHM $\pm 1\sigma$ and $\pm 2\sigma$, respectively. The histogram of the FWHM in the two regions inverted is also shown in the right panel, emphasizing that most of the inverted spectra have large FWHM since broaden spectral line profiles are observed around fading granules. Bottom panel shows the histogram of inferred microturbulence velocity.

denotes the standard deviation of the Doppler velocity at each pixel inferred by the inversion without microturbulence. We emphasize that these standard deviations indicate the velocity gradient on scales larger than $\Delta(\log\tau) \gtrsim 1.2$ that is the interval of the locations of the nodes. On the other hand, the microturbulence term stands for the velocity variation on scales smaller than $\Delta(\log\tau) \lesssim 1.2$. Although there is a large scatter, the microturbulence velocities of about 1 km/s are estimated from the wide spectra with FWHM larger than 165.8 mÅ. The large variation of the Doppler velocity along the LOS is required to reproduce such wide spectral line profiles without mictoturbulence. The average of the standard deviations of Doppler velocity with FWHM from 141.5 mÅ to 157.7 mÅ is 1.3 km/s, while that with FWHM larger than 165.8 mÅ is 3.2 km/s. Note that the average FWHM obtained with the entire FOV of the normal map data is 150 mÅ. The inversion is performed in local regions in the vicinity of fading granules, preferentially showing the larger FWHM than the average. These results demonstrate that the variation of the Doppler velocity along the LOS can explain the spectral line broadening without the microturbulence. In the inversion with microturbulence, some results have small microturbulence velocity for large FWHM. These results also explain the large FWHM by including the variaion of the Doppler velocity along the LOS. Therefore, we cannot distinguish the two scenarios only with the two neutral iron lines observed with Hinode-SOT/SP.

The inverted microturbulence velocities have two components: one is the solution with microturbulence larger than 0.2 km/s and the other is that with microturbulence near zero as shown in the bottom panel in Figure 4.7. Only a little inversion results have microturbulence of about 0.1 km/s. This implies that the degeneration of the two scenarios are not consecutively connected, which leads to the spatially non-smooth results of the inversions as shown in Figures 4.5 and 4.6.

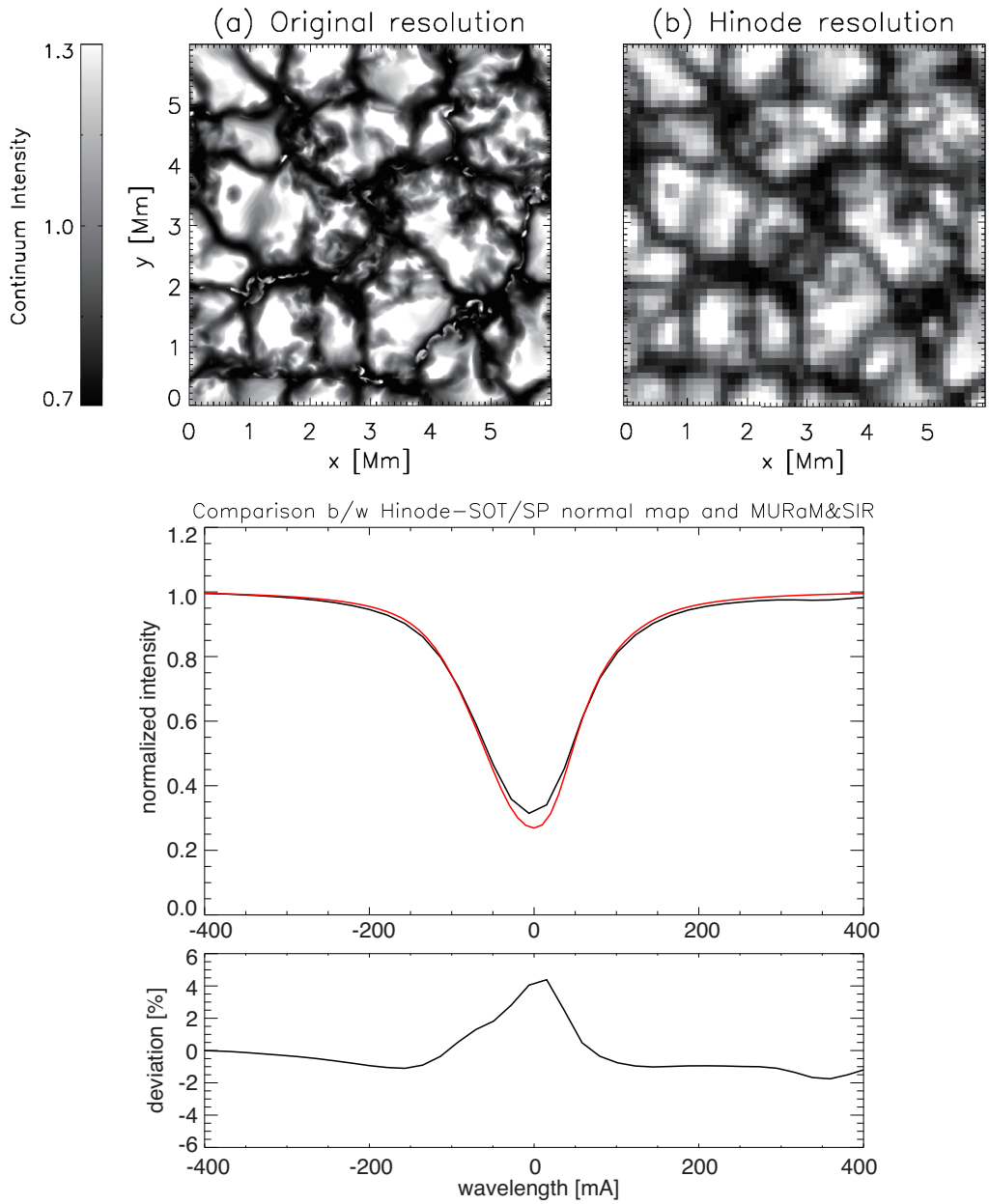

Figure 4.8: Emergent continuum intensity synthesized with the MURaM simulation data with the original resolution (left top), and convolved with the PSF of Hinode-SOT/SP and downsampled to 115 km/pixel (right top). The spatially averaged spectra of the Fe I 6301.5 Å line observed with Hinode-SOT/SP (black) and synthesized with SIR (red) are shown in the middle panel. The difference between them is plotted in the bottom panel.

4.5 Comparison with simulation

To interpret the inversion result carefully, we also check the atmosphere simulated by MURaM code (Vögler *et al.* 2005; Figure 4.8). The simulation data we used here is the same as the data used in chapter 2. In the code, the radiative energy exchange was solved via a non-gray radiative transfer under the assumption of local thermal equilibrium (LTE) to reproduce more realistic granular scale flows in the photosphere. The original simulation data has the grid size of 10.4 km $\times$ 10.4 $\times$ 14 km, covering 6 Mm $\times$ 6 Mm $\times$ 1.4 Mm (Riethmüller *et al.*, 2014). A unipolar homogeneous vertical magnetic field of $B_z = 30$ G was introduced as an initial condition. The simulation used a fully-developed hydro-dynamical simulation as the initial condition and additional calculation for 3 hour of solar time that is enough to reach a statistically stationary state. The temporal casense of the data cube is 35 seconds.

The emergent spectral line profiles of Fe I 6301.5 Å and 6302.5 Å are synthesized with the SIR code that calculates a LTE radiative transfer. To compare with the observation, we convolve the synthesized spectra with the PSF and the line-spread-function of the Hinode-SOT/SP (Figure 4.8). Note that the spatial resolution of the Hinode-SOT/SP is 0.32 arcsec which corresponds to 230 km on the solar surface for the 6302 Å lines. The comparison of the spatially averaged spectral line profiles is also shown in Figure 4.8. The error is small in the wing of the line profile, while the noticable discrepancy appears near the line core. Due to the difference of the line core intensity, FWHM of the averaged profiles are slightly different: 142 mÅ for the synthesized one and 150 mÅ for the observed one. The FWHM of each synthesized spectral line profile is calculated by the bisector analysis in the same way described in Chapter 3.

4.5.1 Evaluation of turbulent velocity

To quantify the small-scale velocity fields that cannot be resolved by the Hinode-SOT/SP, we define two velocity dispersions with using the PSF of the Hinode-

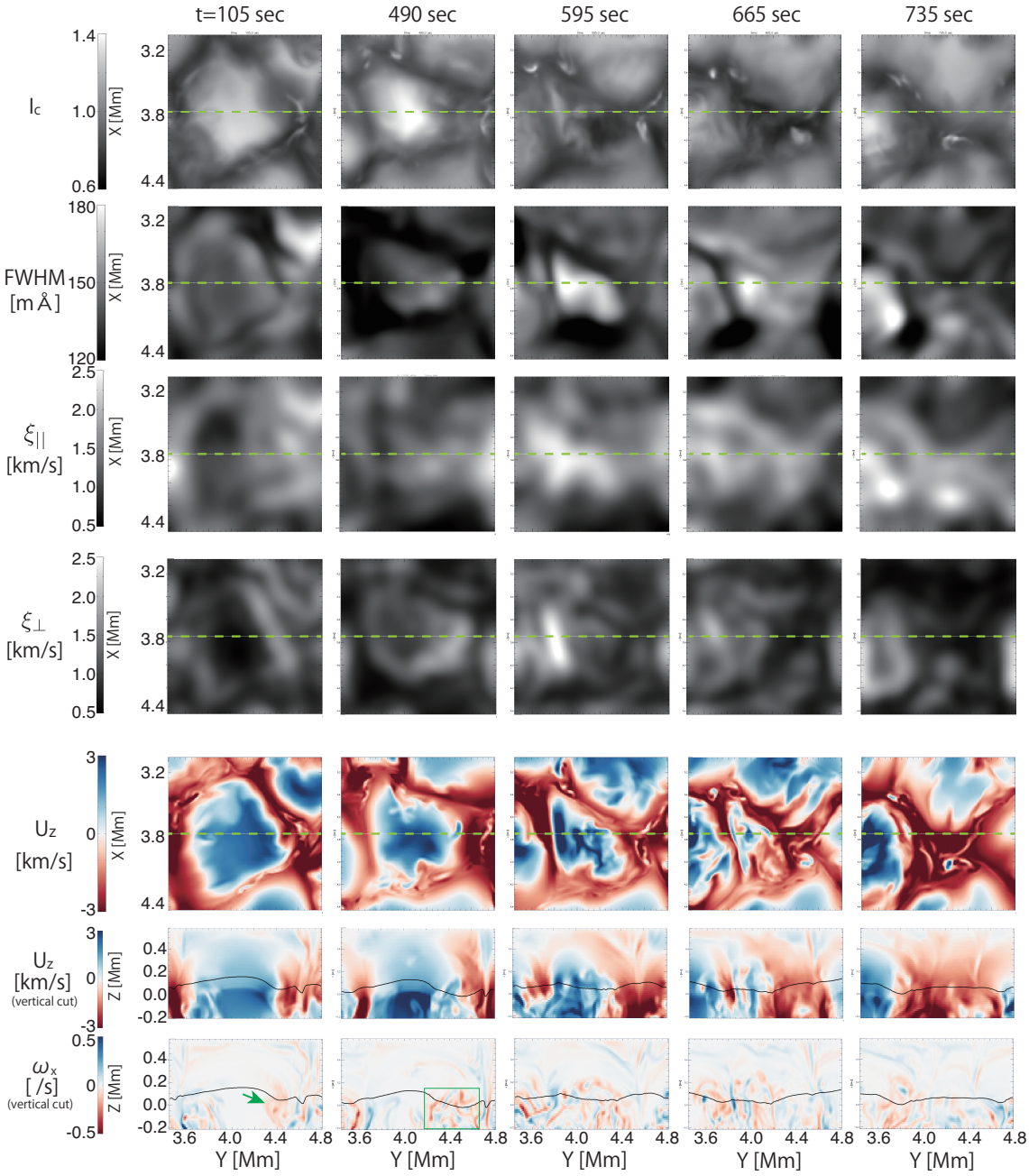

Figure 4.9: Temporal evolution of a fading granule observed in the MURaM data. The horizontal distributions of continuum intensity, FWHM with PSF convolution, the velocity dispersions $\xi_{||}$ and $\xi_{\perp}$, and the vertical velocity at z=112 km (994 km height from the bottom boundary) are shown in upper rows. The vertical cuts at x=4.0 Mm (indicated by the green dashed lines) of vertical velocity and the $x-$component of vorticity are shown in bottom rows. The black solid lines represent the iso-τ surfaces of $\log \tau = 0$.

SOT/SP (P) and the response function for the FWHM. The response function for the FWHM associated with the velocity perturbations $R_v^{\rm FWHM}$ is calculated at each grid by means of the generalized response function (Ruiz Cobo and del Toro Iniesta, 1994) as described in Appendix B.1. It should be noted that $R_v^{\rm FWHM}$ is always zero if it is calculated with the model atmosphere such as HSRA that does not include any LOS velocity variation along the LOS. The small perturbation of the LOS velocity only causes the small shift or asymmetry of the spectral line profile and does not lead to the line broadening (Appendix B.2).

The response function $R_v^{\rm FWHM}$ describes the layer in which the FWHM has a sensitivity of the LOS (vertical) velocity. The vertical average of vertical velocity of each grid is written as

$$\overline{u_z} = \frac{\int u_z |R_v^{\rm FWHM}| d\tau}{\int |R_v^{\rm FWHM}| d\tau}. \tag{4.3}$$

and the horizontal average of $\overline{u_z}$ is defined with the PSF:

$$\langle \overline{u_z} \rangle = \overline{u_z} * P. \tag{4.4}$$

Then, the dispersions of vertical velocities on the LOS and horizontal direction are calculated as

$$\xi_{||}^2 = 2 \left\langle \overline{(u_z - \overline{u_z})^2} \right\rangle, \tag{4.5}$$

$$\xi_{\perp}^2 = 2 \left\langle (\overline{u_z} - \langle \overline{u_z} \rangle)^2 \right\rangle. \tag{4.6}$$

These definitions are similar to those of Steffen, Caffau, and Ludwig (2013) who discussed stellar spectra (observed as a point source), but considering the PSF of the spatially resolving observation and the response function of the 6301.5 Å line. The LOS dispersion $\xi_{||}^2$ is defined as the dispersion of the vertical velocity on the LOS direction with an average over the PSF, and the horizontal dispersion $\xi_{\perp}^2$ is the dispersion of the average vertical velocity within the PSF. Qualitatively, $\xi_{||}$ roughly corresponds to the microturbulence term and $\xi_{\perp}$ to the macroturbulence term. We note that the factors of 2 in $\xi_{||}^2$ and $\xi_{\perp}^2$ come from the definitions of the

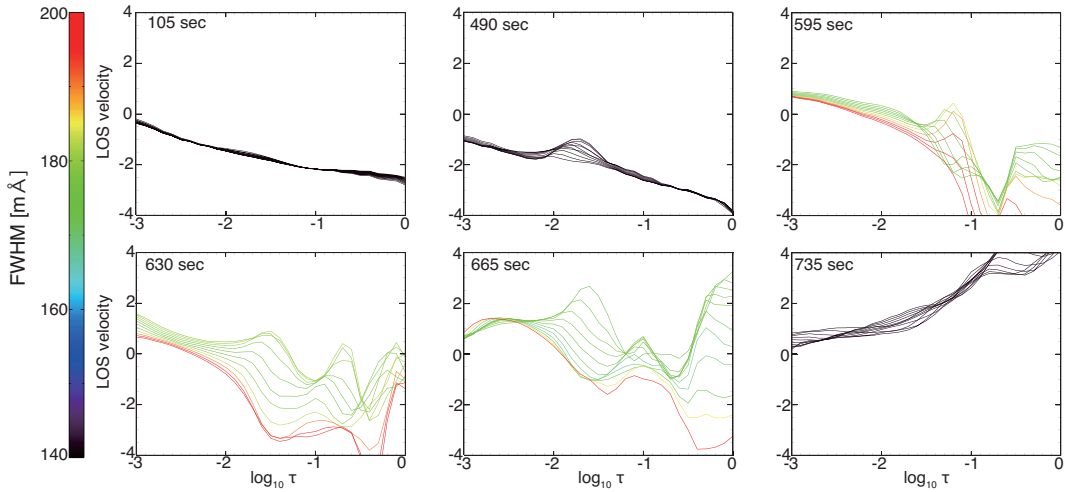

Figure 4.10: The temporal evolutions of the LOS velocities in the fading granule shown in Figure 4.9. LOS velocities at 11 grids around $Y \in [4.02, 4.12]$ Mm along the green line in upper panels in Figure 4.9 are presented. The color shows the FWHM of the original resolution, i.e. without the convolution of the Hinode PSF.

microturbulence and macroturbulence in Equations (1.6) and (1.9): the factor of 2 for the standard deviation in the Gaussian function is included in the micro-/macro-turbulence terms. Here $\xi_{||}$ indicates the velocity dispersion along the LOS direction on scales smaller or similar to the height range where the response function has some sensitivity averaged over the horizontal scale of PSF. On the other hand, $\xi_{\perp}$ shows the velocity dispersion on the horizontal direction on scales smaller than the PSF.

4.5.2 Fading granule in MHD simulation

Figure 4.9 shows an example of a fading granule observed in the simulation. In this fading granule, the decrease of the continuum intensity and change of the vertical velocity from upward to downward are observed and related broad line widths of about 180 mÅ are reproduced. The line broadening appears within the spatial scale of 500 km and lasts for about 100 sec. These features are consistent with the nature

of the observed fading granules described in Chapter 3.

In the former phase before $t = 490$ sec, laminar upflows near the center of the granule are observed. Vorticity distributions are vertically elongated at around the boundary between the granule and the intergranular lane, which indicates the existnece of velocity shears around the boundary. After that, the emergent continuum intensity rapidly decreases. In this fading phase at around 595 sec, a significant line broadening occurs. In this phase, small-scale vorticities appear inside this fading granule and the vertical distributions of vertical velocity have small-scale variations. The enhanced dispersion of vertical velocity can also be seen in the spatial distribution of $\xi_{||}$. The spatial distributions of large FWHM and large $\xi_{||}$ in the fading granule are good agreement with each other. Finally, the fading granule becomes an intergranular lane dominated by strong downflows. The correlation coefficient between FWHM and $\xi_{||}$ calculated with all the five frames is 0.54, while that between FWHM and $\xi_{\perp}$ is 0.25. The FWHM observed with the Hinode resolution reflects the LOS velocity dispersion on the LOS direction rather than the horizontal dispersion.

Figure 4.10 shows the temporal evolutions of the LOS velocity profiles in the fading granule without the PSF convolution. LOS velocity profiles at 11 simulation grids that covers the horizontal scale of 100 km are presented. Here, the scale of 100 km is comparable to the pressure scale height at the solar surface and the photon mean free path. At $t = 105$ sec, the LOS velocities are similar to those in neighboring simulation grids within the scale of 100 km. The LOS velocities have a velocity gradient that is almost constant along the LOS. At $t = 595$ sec, small-scale variations of the velocity gradient exist in the lower photosphere from $\tau = 0$ to -2. These small-scale fluctuations correspond to the LOS velocity variation at around $y = 4.0$ Mm and $z = 0.1$ Mm shown in the vertical cut in Figure 4.9, changing the sings of vorticities within 50 km. These turbulent motions and corresponding line broadenings exist until $t = 665$ sec as shwon in Figure 4.10. The horizontal scale of these fluctuations is also so small that the LOS velocity profiles differ from the neighboring simulation grids. At $t = 735$ sec, the velocity fluctuations are still seen but the amplitude is small, consequently, the FWHM is small.

At $t = 595$ sec, the localized gradient of vertical velocity appears in a few grids on the vertical direction in the simulation, which corresponds to a few 10 km that is smaller than the scale height and the mean free path of photons. Therefore this localized gradient can work similarly to the microturbulence term.

4.5.3 Discussion: driving of turbulent flows

In the MURaM simulation data, spectral line broadening in a fading granule is associated with the turbulent motions in the lower photosphere. In a typical granule with a bright continuum intensity consists of hot and less turbulent upflow plumes in this numerical simulation. At the edge of such a typical granule, because of the presence of an intergranular lane, there inherently exists a horizontal gradient of the vertical velocity. Nesis *et al.* (1993) concluded that line broadening can occur in concentrated regions with a large horizontal gradient of vertical velocity. Solanki *et al.* (1996) suggested that such a horizontal gradient of vertical velocity can broaden the spectral line width due to a kind of macroturbulence effect. As Solanki *et al.* (1996) suggested, the macroturbulent velocity $\xi_\perp$ is large at the boundary where the horizontal gradient of vertical velocity exists. However, the resultant spectral line profile at the boundary does not have a large FWHM at around $y = 3.8$ Mm at t=595 sec in Figure 4.9, even though we consider the PSF of the Hinode-SOT/SP that can cover the strong shear flow structure. Khomenko *et al.* (2010) found both observationally and numerically that the spectral line profiles with small FWHM are preferentially observed at the boundary between a granule and an intergranular lane since the vertical gradient of LOS velocity is small.

Small-scale velocity variations along the LOS can broaden the spectral line widths. During the fading process of a granule, small-scale turbulent motions are developed as shown in Figure 4.9. Small-scale vorticies emphasize the turbulent nature in the fading granule. These turbulent motions result in the small-scale variations of LOS velocity gradient (Figure 4.10) which can cause the spectral line broadening. Both the vertical and horizontal fluctuations of LOS velocity potentially can broaden the spectral line profiles. As demonstrated in Figure 4.10, the

small-scale vertical structures can cause the line broadening. But the contribution of the horizontal structures are not so obvious. Since the region with large FWHM (or developed turbulent motions) are localized, the large FWHM and neighboring small FWHM can be averaged by the PSF. The macroturbulence model (equation 1.9) assumes that the line profiles do not vary within the spatial scale of the PSF, while this assumption may not be valid in such localized event.

These turbulent motions seem to be triggered by the shear flow or vorticity at the boundary between the granule and the intergranular lane indicated by the green arrow in Figure 4.9. Formation of vortex tube at the edges of granules are found observationally (Steiner *et al.*, 2010) and numerically (Kitiashvili *et al.*, 2012). Such vortical flows can excite turbulent motions (green rectangle in Figure 4.9) via the Kelvin-Helmholtz instability. During the fading process of granules, the turbulent motions grow and intrude into the granules.

After the fading process of a granule, converging flows appear probably due to decrease of the gas pressure. Although the fading process are not always associated with the magnetic fields as shown in Chapter 3, magnetic flux can be advected and amplified by these converging flows if there is weak magnetic flux around a fading site. Such amplification of magnetic fields are found by Rempel (2018) in newly formed downflow lanes that causes converging flows and subsequent turbulent flows. Since the turbulent motions are already developed when the magnetic field are advected into the fading site, the small-scale interaction and energy conversion can occur immediately.

In intergranular lanes, the spatial distribution of vorticity shows elongated structures stretched vertically. This demostrates that the horizontal gradients of vertical velocities can be formed but vertical fluctuations of vertical velocities are not ubiquitous in intergranular lanes. The strong downward motions can stabilize the flows near the surface: small perturbations that can be a seed of turbulence should be advected into the convection zone by the strong downflow (Rast, 1998). The original vorticity is seen at $y = 4.4$ Mm at $t = 105$ sec in Figure 4.9. Even though the turbulent motions driven by this shear flow intrude into the granule, the straight

downflow structure still survives in the intergranular lane at $t = 490$ and 595 sec. This can emphasize the less turbulent nature of intergranular lanes.

4.6 Summary

We estimate the atmospheric structure associated with the wide spectral line by performing spectral line inversion with the SIR code. Two inversion scenarios are considered: with and without microturbulence term. Microturbulent velocity of about 1 km/s can explain the wide spectral line width, while the line width is also reproduced without microturbulence by including large gradients of temperature and Doppler velocity. On the other hand, the narrow line profiles in granule and intergranular lanes can be fitted without the microturbulence term, which shows the average microturbulence term in the quiet region is smaller than 1 km/s. This value is much smaller than the average microturbulent velocity of 3.1 km/s at the solar surface obtained by Buehler *et al.* (2015).

We also analyze the MHD simulation data obtained with the MURaM code. Turbulent motions are excited in the vicinity of a fading granule, which broadens the emergent spectral line width. Since the spatial scales of the velocity variation in the lower photosphere are $\sim$ 10 km that is smaller than $\Delta(\log \tau) \lesssim 1$, which demonstrates that the MHD simulation supports the inversion scenario with the microturbulence term. The large gradient of LOS velocity scenario suggested by the inversion without microturbulence is not consistent with the MURaM simulation, since the large downward velocity in the upper photosphere does not appear even during the fading process of a granule. We show that small-scale velocity variations along the LOS direction in the lower photosphere is thought to be the dominant source of the excess broadening, which indicates that the line broadening can be a good tracer of turbulent motions in the photosphere.

The turbulent motions contributing to the line broadening in the fading granule could be driven by the shear flows of upward and downward velocities at the boundary between the granule and the intergranular lane. This implies that some

of the excess line broadening found by Nesis *et al.* (1993) and Hanslmeier, Nesis, and Mattig (1994) may be related to these turbulent motions. The fact that the significant line broadening appears in regions with $I_c \sim 1$ (Figure 3.3) also supports it.

To evaluate such small-scale velocity fields by the spectral line inversion, a large number of nodes for LOS velocity in the lower photosphere is required or else the microturbulence term is necessary in the lower layer. Observing other lines that are sensitive to the lower photosphere is also important. Because of the low continuum opacity, Fe I 15650 Å lines are good candidates to assess the LOS velocity in the lower photosphere, which can be observed with Daniel K. Inouye Solar Telescope (DKIST; Rimmele *et al.* 2020; Rast *et al.* 2021). DKIST has a 4-m aperture and the Diffraction-Limmited Near-IR SpectroPolarimeter has a spatial resolution of 0.1 arcsec at 15650 Å, which corresponds to 70 km on the solar surface. This can spatially resolve the local region with wide spectral line profile in a fading phase of granule. The simultaneous spatial and spectral coverage and the high temporal cadense observation enable us to capture the rapid change of the small-scale flow fields and corresponding line profiles. In addition, it is also worth to observe Fe I 8468 Å and 8514 Å lines via the SUNRISE Chromospheric Infared spectroPolarimeter (Katsukawa *et al.*, 2020) onboard SUNRISE-3 balloon-borne telescope (Feller *et al.*, 2020), which enable us to determine the LOS velocity in the upper photosphere.

Chapter 5

Summary and future prospects

5.1 Summary

The small-scale flows in the solar photosphere are the major ingredients driving the various dynamics such as the atmospheric heating and the local dynamo. Because of the limited instrument resolution and the methodological problem, it was difficult to evaluate the small-scale flows observationally. In this thesis, we investigate both the horizontal and vertical velocity fields on small spatial scales close to the resolution limit by developing a new technique and analyzing the spectral line profiles.

In Chapter 2, we developed a convolutional neural network model with a multi-scale deep learning architecture. This multi-scale deep learning architecture can detect both large-scale structures and small-scale ones simultaneously, which realized the higher accuracy compared to the model previously suggested. The new method is evaluated with the coherence spectrum which is newly introduced in this study, which reveals a strong dependence of the correlation coefficient on the spatial scales. By comparing the results of the three different convection simulations, we found that the decrease of accuracy occurs around the energy injection scales.

In Chapter 3, We investigated the spectral line broadening related to the granulation to reveal the spatial distribution and temporal evolution of FWHM of the spectrum line profiles formed in the photosphere and its association with the gran-

ulation by performing spectropolarimetric observations with Hinode-SOT/SP. As found in the previous studies, FWHMs of the spectral lines are slightly larger in intergranular lanes than in granules. The narrowest spectral lines are observed near the boundary between the granules and intergranular lanes. Thanks to the high spatial, spectral, and temporal resolutions of our observations, we clearly demonstrated that significant line broadening is observed in the regions with $I_{\rm c} \sim 1$. Moreover, the observation that tracks the temporal evolution of the spectral line profiles discovered that both the large positive velocity gradient along LOS, Δv, and large FWHM are observed in fading granules. We found that the line broadening in fading granule cannot be explained only by velocity gradient, which implies another line broadening mechanism such as turbulent motions. Since the relationship between the line broadening and granulation with high spatial and temporal resolutions has not been investigated, our results give new insights into the granular dynamics.

For a quantitative understanding of excessive line broadening associated with the fading granules, we performed spectral line inversion and comparison with the MHD simulation in Chapter 4. We found that microturbulent velocity of about 1 km/s can explain the wide spectral line width, while the line width is also reproduced without microturbulence by including large gradients of temperature and Doppler velocity along LOS. On the other hand, the narrow line profiles in granule and intergranular lanes can be fitted without the microturbulence term, which shows the average microturbulence term in the quiet region is smaller than 1 km/s. Spectral line synthesis with the MHD simulation data suggested that the spectral line broadening in fading granules is caused by the velocity dispersion along the LOS associated with turbulent flows in the lower photosphere. Velocity shears at the boundary between a granule and an intergranular lane could drive the turbulent flows. Our result indicates that the spectral line widths can potentially be a tracer of small-scale velocity variation.

5.2 Future prospects

In this thesis, we investigated the line broadening in the quiet region on the solar surface and constrained the velocity fields on scales close to the instrument resolution. However, there is the ambiguity of the line broadening mechanism in fading granules. In addition, the line widths in strongly magnetized regions are not investigated in this thesis. Therefore, there are remaining issues: (1) observational distinction of between the velocity gradient and the microturbulence not only in the weakly magnetized region but also in the strongly magnetized region, (2) direct detection of temporal evolutions of magnetic flux associated with the small-scale velocities.

Observing with the DKIST will enable us to conduct multi-line observations with high spatial resolutions. We can observe Fe I lines at 6302 Å with the spatial resolution of 30 km and 15650 Å of 70 km. Since the opacity of the continuum is low at wavelength of 16000 Å, Fe I 15650 Å line is useful to infer the velocity fields in the lower photosphere. It is also worth observing infared lines such as Si I 10827 Å and Ca II 8542 Å. The former has a sensitivity to the upper photosphere and the latter is formed in the chromosphere. This multi-line observation can determine the LOS velocity variation on large scales along the optical depth, which potentially provides a distinction of the two scenarios of line broadening we obtained in this thesis.

The high spatial resolution of the DKIST observation is also helpful to investigate the flow fields in the vicinity of magnetic elements. Because of the limited instrument resolution, these small-scale magnetic elements cannot be resolved by Hinode-SOT/SP, which causes a miss detection of small-scale magnetic fields and associated flow fields. In our MURaM simulation, the broad line profiles around the magnetic elements are predicted. Such small-scale velocity fields near the magnetic structures are important for driving high-frequency MHD waves producing upward Poynting flux. Simultaneous observations of photospheric and chromospheric lines can measure the Poynting flux related to this process. Given that the efficient small-

scale dynamo works near the solar surface, the growth of small-scale flows is followed by magnetic field amplification and subsequent suppression of the turbulent velocity due to the Lorentz force feedback. The methods we newly introduced in this thesis with the upcoming observations will lead us to the direct detection of such small-scale physical processes.

Appendix A

Response Function

The introduction of the response function is given in this chapter. The radiative transfer equation under the LTE condition is

$$\frac{dI_\lambda}{d\tau_\mathrm{c}} = \kappa_\lambda (I_\lambda - S_\lambda), \tag{A.1}$$

and the formal solution is

$$I_\lambda = \int_0^\infty \kappa_\lambda S_\lambda \exp\left[-\tau_\lambda\right] d\tau_\mathrm{c}. \tag{A.2}$$

Here, $\kappa_\lambda = 1 + \eta_\lambda$ is the absorption coefficient at a wavelength λ normalized by the absorption coefficient of the continuum α_c, and the optical depth at a wavelength λ is

$$\tau_\lambda(\tau_\mathrm{c}) = \int_0^{\tau_\mathrm{c}} \kappa_\lambda(\tau'_\mathrm{c}) d\tau'_\mathrm{c}. \tag{A.3}$$

Let $\boldsymbol{x}(\tau_\mathrm{c})$ represent physical quantities (such as temperature, velocities, and density) of the atmosphere at each height. We discuss the emergent intensity from the unperturbed atmosphere described as $\overline{\boldsymbol{x}}$ and that from the different atmosphere $\overline{\boldsymbol{x}} + \delta\boldsymbol{x}$. We assume that the source function, the normalized absorption coefficient,

and the optical depth corresponding to these atmospheres are written as follows:

$$\overline{S_\lambda} = S_\lambda(\tau_\mathrm{c}|\overline{\boldsymbol{x}}), \tag{A.4}$$

$$\overline{\kappa_\lambda} = \kappa_\lambda(\tau_\mathrm{c}|\overline{\boldsymbol{x}}), \tag{A.5}$$

$$\overline{\tau_\lambda} = \int_0^{\tau_\mathrm{c}} \overline{\kappa_\lambda}(\tau_\mathrm{c}')d\tau_\mathrm{c}', \tag{A.6}$$

$$\delta S_\lambda = \frac{\partial S_\lambda}{\partial \boldsymbol{x}} \cdot \delta \boldsymbol{x}, \tag{A.7}$$

$$\delta \kappa_\lambda = \frac{\partial \kappa_\lambda}{\partial \boldsymbol{x}} \cdot \delta \boldsymbol{x}, \tag{A.8}$$

$$\delta \tau_\lambda = \int_0^{\tau_\mathrm{c}} \delta\kappa_\lambda(\tau_\mathrm{c}')d\tau_\mathrm{c}'. \tag{A.9}$$

Consequently, the difference of the emergent intensities δI_λ is written as

$$\delta I_\lambda = \int_0^\infty (\overline{\kappa_\lambda} + \delta\kappa_\lambda)(\overline{S_\lambda} + \delta S_\lambda)\exp[-(\overline{\tau_\lambda} + \delta\tau_\lambda)]d\tau_\mathrm{c} - \int_0^\infty \overline{\kappa_\lambda}\,\overline{S_\lambda}\exp[-\overline{\tau_\lambda}]d\tau_\mathrm{c}. \tag{A.10}$$

The first-order term is

$$\delta I_\lambda^{(1)} = \int_0^\infty (\overline{\kappa_\lambda}\delta S_\lambda + \overline{S_\lambda}\delta\kappa_\lambda - \overline{\kappa_\lambda}\,\overline{S_\lambda}\delta\tau_\lambda)\exp[-\overline{\tau_\lambda}]d\tau_\mathrm{c}, \tag{A.11}$$

$$\begin{aligned} &= \int_0^\infty \left(\overline{S_\lambda}\frac{\partial\kappa_\lambda}{\partial\boldsymbol{x}} + \overline{\kappa_\lambda}\frac{\partial S_\lambda}{\partial\boldsymbol{x}}\right) e^{-\overline{\tau_\lambda}} \cdot \delta\boldsymbol{x}d\tau_\mathrm{c} \\ &\quad - \int_0^\infty \overline{S_\lambda}\,\overline{\kappa_\lambda}e^{-\overline{\tau_\lambda}}\left\{\int_0^{\tau_\mathrm{c}} \frac{\partial\kappa}{\partial\boldsymbol{x}}(\tau_\mathrm{c}')\cdot\delta\boldsymbol{x}(\tau_\mathrm{c}')d\tau_\mathrm{c}'\right\}d\tau_\mathrm{c} \end{aligned} \tag{A.12}$$

$$\begin{aligned} &= \int_0^\infty \left(\overline{S_\lambda}\frac{\partial\kappa_\lambda}{\partial\boldsymbol{x}} + \overline{\kappa_\lambda}\frac{\partial S_\lambda}{\partial\boldsymbol{x}}\right) e^{-\overline{\tau_\lambda}} \cdot \delta\boldsymbol{x}d\tau_\mathrm{c} \\ &\quad - \int_0^\infty d\tau_\mathrm{c}'\delta\kappa_\lambda(\tau_\mathrm{c}')\exp\left[-\int_0^{\tau_\mathrm{c}'}\kappa_\lambda(\tau_\mathrm{c}'')d\tau_\mathrm{c}''\right]\left\{\int_{\tau_\mathrm{c}'}^\infty d\tau_\mathrm{c}\overline{S_\lambda}(\tau_\mathrm{c})\overline{\kappa_\lambda}(\tau_\mathrm{c})\exp\left[-\int_{\tau_\mathrm{c}'}^{\tau_\mathrm{c}}\kappa_\lambda(\tau_\mathrm{c}'')d\tau_\mathrm{c}''\right]\right\} \end{aligned} \tag{A.13}$$

$$= \int_0^\infty \left(\overline{S_\lambda}\frac{\partial\kappa_\lambda}{\partial\boldsymbol{x}} + \overline{\kappa_\lambda}\frac{\partial S_\lambda}{\partial\boldsymbol{x}}\right) e^{-\overline{\tau_\lambda}} \cdot \delta\boldsymbol{x}d\tau_\mathrm{c} - \int_0^\infty \frac{\partial\kappa_\lambda}{\partial\boldsymbol{x}}\cdot\delta\boldsymbol{x}e^{-\overline{\tau_\lambda}}I_\lambda(\tau_\mathrm{c})d\tau_\mathrm{c} \tag{A.14}$$

$$\therefore \delta I_\lambda^{(1)} = \int_0^\infty \left(\overline{S_\lambda}\frac{\partial\kappa_\lambda}{\partial\boldsymbol{x}} + \overline{\kappa_\lambda}\frac{\partial S_\lambda}{\partial\boldsymbol{x}} - \frac{\partial\kappa_\lambda}{\partial\boldsymbol{x}}I_\lambda\right)\exp\left[-\int_0^{\tau_\mathrm{c}}\overline{\kappa_\lambda}(\tau_\mathrm{c}')d\tau_\mathrm{c}'\right]\cdot\delta\boldsymbol{x}(\tau_\mathrm{c})d\tau_\mathrm{c}. \tag{A.15}$$

According to the definition of the response function (Equation 1.10), we obtain the response function as

$$R_x(\lambda, \tau_\mathrm{c}) = -\left\{ \frac{\partial \kappa_\lambda}{\partial x} \left(I_\lambda - \overline{S_\lambda} \right) - \overline{\kappa_\lambda} \frac{\partial S_\lambda}{\partial x} \right\} \exp\left[-\int_0^{\tau_\mathrm{c}} \overline{\kappa_\lambda}(\tau_\mathrm{c}') d\tau_\mathrm{c}' \right], \tag{A.16}$$

$$= -\left\{ \frac{\partial \kappa_\lambda}{\partial x} \int_{\tau_\mathrm{c}}^{\infty} \frac{d\overline{S_\lambda}}{d\tau_\mathrm{c}'} \exp\left[-(\tau_\mathrm{c}' - \tau_\mathrm{c}) \right] d\tau_\mathrm{c}' - \overline{\kappa_\lambda} \frac{\partial S_\lambda}{\partial x} \right\} \exp\left[-\int_0^{\tau_\mathrm{c}} \overline{\kappa_\lambda}(\tau_\mathrm{c}') d\tau_\mathrm{c}' \right]. \tag{A.17}$$

This is the formal solution of the response function (Sanchez Almeida, 1992). Since the source function is equivalent to the Planck function under the LTE condition and the absorption coefficient is described by a Voigt function (Equation 1.5), we can calculate the response function only with the initial atmosphere $\overline{\boldsymbol{x}}$.

Appendix B

Response function and the bisector analyses

B.1 Response function for the FWHM

The idea of generalized response function is introduced by Ruiz Cobo and del Toro Iniesta (1994). In this chapter, we applied it to the FWHM in the same manner that González Manrique *et al.* (2020) performed for the bisector velocities. The response function for the FWHM related to velocity perturbations is defined with the same manner of the response function for the intensity:

$$\delta\mathrm{FWHM} = \int_0^\infty R_v^{\mathrm{FWHM}}(\tau)\delta v(\tau)d\tau. \tag{B.1}$$

Here, we demonstrate that the reponse function R_v^{FWHM} can be described with $R_v(\lambda, \tau)$ at four wavelength positions λ_i $(i = 1, 2, 3, 4)$, given $\lambda_1 < \lambda_2 < \lambda_3 < \lambda_4$. The FWHM is determined by the intensities at these wavelengths like

$$\mathrm{FWHM} \equiv \lambda_+ - \lambda_-, \tag{B.2}$$

$$= \sum_{i=1}^{4} \alpha_i I(\lambda_i), \tag{B.3}$$

where λ_+ and λ_- are the wavelength that satisfy $\hat{I} = 0.5$ and the coefficients α_i corresponds to the linear interpolation (Appendix D). They are written as follows:

$$\alpha_1 = -\frac{(\lambda_1 - \lambda_2)(I_2 - I_{\rm HM})}{(I_1 - I_2)^2}, \tag{B.4}$$

$$\alpha_2 = -\frac{(\lambda_2 - \lambda_1)(I_1 - I_{\rm HM})}{(I_1 - I_2)^2}, \tag{B.5}$$

$$\alpha_3 = \frac{(\lambda_3 - \lambda_4)(I_4 - I_{\rm HM})}{(I_3 - I_4)^2}, \tag{B.6}$$

$$\alpha_4 = \frac{(\lambda_4 - \lambda_3)(I_3 - I_{\rm HM})}{(I_3 - I_4)^2}. \tag{B.7}$$

Here, $I_{\rm HM}$ represents the intensity that corresponds to $\hat{I} = 0.5$ where the FWHM is measured. Consequently, by applying the chain rule, the response function for the FWHM associated with velocity perturbations is obtained by the following equations:

$$\delta{\rm FWHM} = \sum_i \alpha_i \delta I(\lambda_i) \tag{B.8}$$

$$= \sum_i \alpha_i \int R_v(\lambda_i, \tau)\delta v(\tau) d\tau \tag{B.9}$$

$$= \int \left\{ \sum_i \alpha_i R_v(\lambda_i, \tau) \right\} \delta v(\tau) d\tau \tag{B.10}$$

$$\therefore R_v^{\rm FWHM}(\tau) = \sum_i \alpha_i R_v(\lambda_i, \tau). \tag{B.11}$$

B.2 Response function with a model atmosphere

Given a model atmosphere that does not include any LOS veolcity, then the response function for FWHM associated with the LOS velocity perturbation yields to zero. It is because that the spectral line profile have to be shifted and have not to be broadened by a constant Doppler velocity. Due to the absence of LOS velocity, the spectral line profile is symmetric with the line core wavelength of λ_0, and we can

obtain following relations:

$$\lambda_0 - \lambda_1 = \lambda_4 - \lambda_0, \quad I_1 = I_4, \tag{B.12}$$

$$\lambda_0 - \lambda_2 = \lambda_3 - \lambda_0, \quad I_2 = I_3, \tag{B.13}$$

$$\alpha_1 = \alpha_4, \tag{B.14}$$

$$\alpha_2 = \alpha_3. \tag{B.15}$$

Since the response function for the intensity $R_v(\lambda, \tau)$ has an anti-symmetric profile ($R_v(\lambda_0 - \delta\lambda, \tau) = -R_v(\lambda_0 + \delta\lambda, \tau)$) as shown in Figure 1.7, the resultant response function R_v^{FWHM} is always zero.

The response function for the bisector velocity associated with the velocity perturbation is investigated by González Manrique *et al.* (2020). The bisector velocity at $\hat{I} = 0.5$ is obtained as

$$v_{0.5} \equiv \frac{c}{\lambda_0}\left\{\frac{1}{2}(\lambda_+ + \lambda_-) - \lambda_0\right\}, \tag{B.16}$$

$$= \frac{c}{2\lambda_0}\sum_i \beta_i I(\lambda_i) - c, \tag{B.17}$$

$$\beta_1 = \frac{(\lambda_1 - \lambda_2)(I_2 - I_{\mathrm{HM}})}{(I_1 - I_2)^2} = -\alpha_1, \tag{B.18}$$

$$\beta_2 = \frac{(\lambda_2 - \lambda_1)(I_1 - I_{\mathrm{HM}})}{(I_1 - I_2)^2} = -\alpha_2, \tag{B.19}$$

$$\beta_3 = \frac{(\lambda_3 - \lambda_4)(I_4 - I_{\mathrm{HM}})}{(I_3 - I_4)^2} = \alpha_3, \tag{B.20}$$

$$\beta_4 = \frac{(\lambda_4 - \lambda_3)(I_3 - I_{\mathrm{HM}})}{(I_3 - I_4)^2} = \alpha_4. \tag{B.21}$$

Then, the response function for bisector velocity $R_v^{\mathrm{bis},0.5}$ can be written as

$$R_v^{\mathrm{bis},0.5}(\tau) = \frac{c}{2\lambda_0}\sum_i \beta_i R_v(\lambda_i, \tau). \tag{B.22}$$

Since the signs of β_1 and β_2 are different from those of α_1 and α_2, the response function does not yield to zero for the model atmosphere, which means the velocity perturbation can cause a shift of line profile and an asymmetric profile.

Appendix C

Coherence Spectrum Analysis

We introduce a new measure *coherence spectrum* for evaluating the network. In this section, we describe the definition of the coherence spectrum and provide a proof of Equation (2.7). When we have the spatial distributions of physical quantities X and Y, we can define the 2-dimensional cross-spectrum by using the Fourier transform as follows:

$$S_{XY}(k_x, k_y) = \hat{X}^* \hat{Y}, \tag{C.1}$$

$$\hat{X}(k_x, k_y) = \frac{1}{N^2} \sum_{x,y} X(x, y) \exp[-i(k_x x + k_y y)]. \tag{C.2}$$

The power spectrum is as follows:

$$E_X(k) = \frac{1}{2\Delta k} \sum_{\sqrt{k_x^2+k_y^2} \in [k-\Delta k/2, k+\Delta k/2)} |\hat{X}(k_x, k_y)|^2, \tag{C.3}$$

where Δk is the sampling interval of the wavenumber. Furthermore, the cross-spectrum is equivalent to the Fourier transform of the correlation function between X and Y, which corresponds to the Wiener–Khinchin theorem.

$$C_{XY}(\xi, \eta) = \sum_{k_x, k_y} S_{XY}(k_x, k_y) \exp[i(k_x \xi + k_y \eta)]. \tag{C.4}$$

Then, we obtain the relationship between the global-correlation-coefficient R_{XY} and 2-dimensional cross-spectrum:

$$R_{XY}(0,0) = \frac{1}{\sqrt{C_{XX}(0,0)C_{YY}(0,0)}} \sum_{k_x,k_y} S_{XY}(k_x,k_y). \tag{C.5}$$

Here, we define the cross-spectrum by calculating the ensemble average $\langle\rangle$ and integrating the 2-dimensional cross-spectrum as follows:

$$S_{XY}(k) = \frac{1}{2\Delta k} \sum_{\sqrt{k_x^2+k_y^2}\in[k-\Delta k/2,k+\Delta k/2)} \langle S_{XY}\rangle(k_x,k_y). \tag{C.6}$$

The phase of the averaged 2-dimensional cross-spectrum corresponds to the 'average' phase difference between the two Fourier components. Given the contour integration, the imaginary part of the cross-spectrum converges to zero because $S_{XY}(-k_x,-k_y) = S^*_{XY}(k_x,k_y)$ is always satisfied. This integration is justified when the statistical isotropy is assumed or else the resultant coherence spectrum can be misleading. Consequently, the coherence spectrum defined below is a real number.

$$\gamma_{XY}(k) = \frac{S_{XY}(k)}{\sqrt{\langle E_X\rangle(k)\langle E_Y\rangle(k)}}, \tag{C.7}$$

Hence, we obtain the following.

$$R_{XY}(0,0) = \frac{\sum_k \sqrt{\langle E_X\rangle\langle E_Y\rangle}\gamma_{XY}(k)}{\sqrt{\sum_k \langle E_X\rangle(k) \sum_{k'} \langle E_Y\rangle(k')}}, \tag{C.8}$$

where we use equation $C_{XX}(0,0) = \overline{X^2} = 2\sum_k E_X(k)\Delta k$ and condition of the statistical steady state $\overline{X^2} = \langle\overline{X^2}\rangle$.

Appendix D

Error Estimation of Bisector Analysis

Here, we describe the error estimation of the bisector analysis. We define the normalized intensity $\hat{I}$ as,

$$\hat{I} \equiv \frac{I - \min(I_\lambda)}{I_{\rm cont} - \min(I_\lambda)}. \tag{D.1}$$

We define i_c as the target spectral position in the pixel unit as follows:

$$i_c \equiv i_2 - \Delta i. \tag{D.2}$$

By interpolating with a linear function (Figure D.1), we obtain,

$$\Delta i : (i_2 - i_1) = (\hat{I}_c - \hat{I}_2) : (\hat{I}_1 - \hat{I}_2), \tag{D.3}$$

$$\therefore \Delta i = \frac{\hat{I}_c - \hat{I}_2}{\hat{I}_1 - \hat{I}_2}. \tag{D.4}$$

If we assume that the error is chiefly caused by the random intensity fluctuation ($|\delta I|/I \equiv \alpha$), the average fluctuation of $\hat{I}$ can be approximately written as follows:

$$|\delta \hat{I}| = \frac{|\delta I|}{I_{\rm cont} - \min(I_\lambda)} \tag{D.5}$$

$$= \frac{\alpha I}{I_{\rm cont} - \min(I_\lambda)} \tag{D.6}$$

$$= \alpha \left(\hat{I} + \frac{\min(I_\lambda)}{I_{\rm cont} - \min(I_\lambda)} \right) \sim (\hat{I} + 0.46)\alpha, \tag{D.7}$$

Then, we obtain,

$$\delta(\Delta i) = \sqrt{\left(\frac{\partial(\Delta i)}{\partial \hat{I}_2}\right)^2 |\delta \hat{I}_2|^2 + \left(\frac{\partial(\Delta i)}{\partial \hat{I}_1}\right)^2 |\delta \hat{I}_1|^2} \tag{D.8}$$

$$< \frac{1}{|\hat{I}_1 - \hat{I}_2|}\sqrt{|\delta \hat{I}_1|^2 + |\delta \hat{I}_2|^2} = \frac{\sqrt{2}}{|\hat{I}_1 - \hat{I}_2|}|\delta \hat{I}|. \tag{D.9}$$

The difference $|\hat{I}_1 - \hat{I}_2|$ varies based on $\hat{I}$: $|\hat{I}_1 - \hat{I}_2| \sim 0.15$ for $\hat{I} = 0.5$, and $|\hat{I}_1 - \hat{I}_2| \sim 0.06$ for $\hat{I} = 0.05$.

The Doppler velocity is calculated as,

$$v_{\hat{I}} = \frac{\left\{\frac{1}{2}(i_{\mathrm{c,left}} + i_{\mathrm{c,right}}) - i_0\right\}\Delta\lambda}{\lambda_0}\, c, \tag{D.10}$$

and the full width is given by,

$$\mathrm{FW}_{\hat{I}} = (i_{\mathrm{c,right}} - i_{\mathrm{c,left}})\Delta\lambda, \tag{D.11}$$

where i_0 and $\Delta\lambda$ represent the pixel index of the line center of Fe I 6301.5 Å and the spectral sampling (21.5 mÅ/pixel) of Hinode-SOT SP, respectively.

For the data set 1, which has an intensity fluctuation of $\alpha = 0.47\%$, the errors in Doppler velocities and FWHM are defined as follows:

$$\delta\left(v_{0.5}\right) = \frac{\delta(\Delta i)}{\sqrt{2}}\left(\frac{\Delta\lambda}{\lambda_0}\right) c\Big|_{\hat{I}=0.50} = 0.03 \text{ km/s} \tag{D.12}$$

$$\delta\left(\mathrm{FWHM}\right) = \sqrt{2}\delta(\Delta i)\Delta\lambda\Big|_{\hat{I}=0.50} = 1.3 \text{ mÅ} \tag{D.13}$$

$$\delta\left(v_{0.05}\right) = \frac{\delta(\Delta i)}{\sqrt{2}}\left(\frac{\Delta\lambda}{\lambda_0}\right) c\Big|_{\hat{I}=0.05} = 0.04 \text{ km/s} \tag{D.14}$$

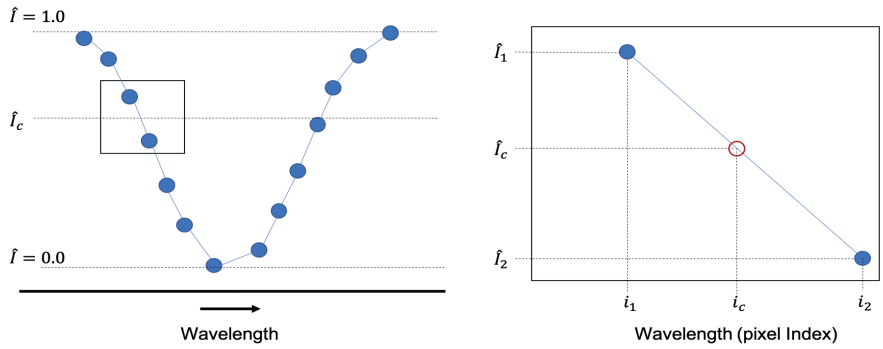

Figure D.1: Schematic of bisector analysis: blue circles indicate the observed intensity. To derive the spectral line profile at a specific intensity $\hat{I}_c$, we interpolate the observational data with the linear functions. The errors transported into the final results originate from the intensity fluctuation at both sides of the fitting region, $(i_1, \hat{I}_1)$ and $(i_2, \hat{I}_2)$, where $i_2 = i_1 + 1$ in the pixel unit.

Appendix E

Behavior of Total Polarization

We use the total polarization $P_{\rm tot}$ derived by the `sp_prep` routine (Lites and Ichimoto, 2013) as the agent of unsigned magnetic flux $|B|$. In Figure E.1, we compare the $P_{\rm tot}$ with $|B|$ of the Hinode level 2 data, which is derived using the Milne-Eddington approximation. Then, we obtain a linear relation as follows:

$$P_{\rm tot}\ [\%] = 0.004|B| + 0.09. \tag{E.1}$$

The equipartition magnetic flux of approximately 450 Mx/cm^2 corresponds to $P_{\rm tot} = 2\%$.

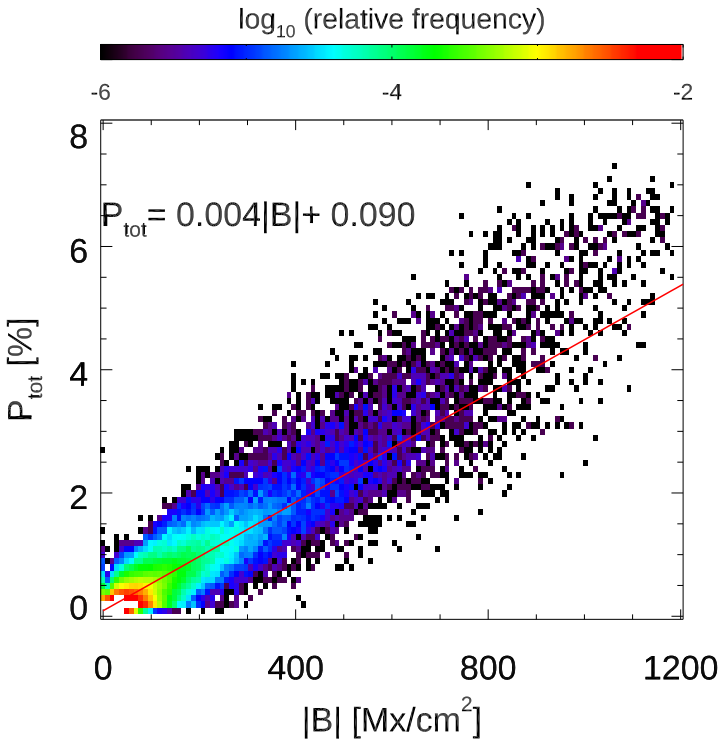

Figure E.1: Relationship between total polarization $P_{\rm tot}$ and magnetic flux of the Hinode level 2 data. The result of linear regression is indicated by the red line.

References

Abramenko, V.I., Yurchyshyn, V.B., Goode, P.R., Kitiashvili, I.N., Kosovichev, A.G.: 2012, Detection of Small-scale Granular Structures in the Quiet Sun with the New Solar Telescope. *Astrophys. J. Lett.* **756**, L27.

Adam, M.G., Ibbetson, P.A., Petford, A.D.: 1976, The solar limb effect: observations of line contours and line shifts. *Mon. Not. Roy. Astron. Soc.* **177**, 687. DOI.

Antolin, P., Shibata, K.: 2010, The Role Of Torsional Alfvén Waves in Coronal Heating. *Astrophys. J.* **712**, 494.

Antolin, P., Okamoto, T.J., De Pontieu, B., Uitenbroek, H., Van Doorsselaere, T., Yokoyama, T.: 2015, Resonant Absorption of Transverse Oscillations and Associated Heating in a Solar Prominence. II. Numerical Aspects. *Astrophys. J.* **809**, 72.

Asensio Ramos, A., Requerey, I.S., Vitas, N.: 2017, DeepVel: Deep learning for the estimation of horizontal velocities at the solar surface. *Astron. Astrophys.* **604**, A11. DOI.

Asplund, M., Nordlund, Å., Trampedach, R., Allende Prieto, C., Stein, R.F.: 2000, Line formation in solar granulation. I. Fe line shapes, shifts and asymmetries. *Astron. Astrophys.* **359**, 729.

Barthol, P., Gandorfer, A., Solanki, S.K., Schüssler, M., Chares, B., Curdt, W., Deutsch, W., Feller, A., Germerott, D., Grauf, B., Heerlein, K., Hirzberger, J.,

Kolleck, M., Meller, R., Müller, R., Riethmüller, T.L., Tomasch, G., Knölker, M., Lites, B.W., Card, G., Elmore, D., Fox, J., Lecinski, A., Nelson, P., Summers, R., Watt, A., Martínez Pillet, V., Bonet, J.A., Schmidt, W., Berkefeld, T., Title, A.M., Domingo, V., Gasent Blesa, J.L., Del Toro Iniesta, J.C., López Jiménez, A., Álvarez-Herrero, A., Sabau-Graziati, L., Widani, C., Haberler, P., Härtel, K., Kampf, D., Levin, T., Pérez Grande, I., Sanz-Andrés, A., Schmidt, E.: 2011, The Sunrise Mission. *Solar Phys.* **268**, 1.

Bellot Rubio, L., Orozco Suárez, D.: 2019, Quiet Sun magnetic fields: an observational view. *Living Reviews in Solar Physics* **16**, 1.

Bellot Rubio, L.R.: 2009, Detection of Supersonic Horizontal Flows in the Solar Granulation. *Astrophys. J.* **700**(1), 284. DOI.

Bellot Rubio, L.R., Beck, C.: 2005, Magnetic Flux Cancellation in the Moat of Sunspots: Results from Simultaneous Vector Spectropolarimetry in the Visible and the Infrared. *Astrophys. J. Lett.* **626**(2), L125. DOI.

Berger, T.E., Löfdahl, M.G., Shine, R.S., Title, A.M.: 1998, Measurements of Solar Magnetic Element Motion from High-Resolution Filtergrams. *Astrophys. J.* **495**(2), 973. DOI.

Bolgiano, J. R.: 1959, Turbulent spectra in a stably stratified atmosphere. *J. Geophys. Res.* **64**(12), 2226. DOI.

Bonet, J.A., Márquez, I., Sánchez Almeida, J., Cabello, I., Domingo, V.: 2008, Convectively Driven Vortex Flows in the Sun. *Astrophys. J. Lett.* **687**, L131.

Brandt, P.N., Scharmer, G.B., Ferguson, S., Shine, R.A., Tarbell, T.D., Title, A.M.: 1988, Vortex flow in the solar photosphere. *Nature* **335**, 238.

Bray, R.J., Loughhead, R.E., Durrant, C.J.: 1984, *The solar granulation (2nd edition).*

Buehler, D., Lagg, A., Solanki, S.K.: 2013, Quiet Sun magnetic fields observed by Hinode: Support for a local dynamo. *Astron. Astrophys.* **555**, A33.

Buehler, D., Lagg, A., Solanki, S.K., van Noort, M.: 2015, Properties of solar plage from a spatially coupled inversion of Hinode SP data. *Astron. Astrophys.* **576**, A27. DOI.

Cossette, J.-F., Rast, M.P.: 2016, Supergranulation as the Largest Buoyantly Driven Convective Scale of the Sun. *Astrophys. J. Lett.* **829**, L17.

Cranmer, S.R., Winebarger, A.R.: 2019, The Properties of the Solar Corona and Its Connection to the Solar Wind. *ARA&A* **57**, 157. DOI.

Danilovic, S., Schüssler, M., Solanki, S.K.: 2010, Probing quiet Sun magnetism using MURaM simulations and Hinode/SP results: support for a local dynamo. *Astron. Astrophys.* **513**, A1. DOI.

Danilovic, S., van Noort, M., Rempel, M.: 2016, Internetwork magnetic field as revealed by two-dimensional inversions. *Astron. Astrophys.* **593**, A93. DOI.

De Pontieu, B., McIntosh, S.W., Carlsson, M., Hansteen, V.H., Tarbell, T.D., Schrijver, C.J., Title, A.M., Shine, R.A., Tsuneta, S., Katsukawa, Y., Ichimoto, K., Suematsu, Y., Shimizu, T., Nagata, S.: 2007, Chromospheric Alfvénic Waves Strong Enough to Power the Solar Wind. *Science* **318**, 1574.

De Pontieu, B., Carlsson, M., Rouppe van der Voort, L.H.M., Rutten, R.J., Hansteen, V.H., Watanabe, H.: 2012, Ubiquitous Torsional Motions in Type II Spicules. *Astrophys. J. Lett.* **752**(1), L12. DOI.

Dorotovič, I., Erdélyi, R., Karlovský, V.: 2008, Identification of linear slow sausage waves in magnetic pores. In: Erdélyi, R., Mendoza-Briceno, C.A. (eds.) *Waves & Oscillations in the Solar Atmosphere: Heating and Magneto-Seismology* **247**, 351. DOI. ADS.

Dravins, D., Lindegren, L., Nordlund, A.: 1981, Solar granulation - Influence of convection on spectral line asymmetries and wavelength shifts. *Astron. Astrophys.* **96**(1-2), 345.

Edlén, B.: 1943, Die Deutung der Emissionslinien im Spektrum der Sonnenkorona. Mit 6 Abbildungen. *Zeitschrift für Astrophysik* **22**, 30.

Feller, A., Gandorfer, A., Iglesias, F.A., Lagg, A., Riethmüller, T.L., Solanki, S.K., Katsukawa, Y., Kubo, M.: 2020, The SUNRISE UV Spectropolarimeter and imager for SUNRISE III. In: *Society of Photo-Optical Instrumentation Engineers (SPIE) Conference Series*, *Society of Photo-Optical Instrumentation Engineers (SPIE) Conference Series* **11447**, 11447AK. DOI.

Fujimura, D., Tsuneta, S.: 2009, Properties of Magnetohydrodynamic Waves in the Solar Photosphere Obtained with Hinode. *Astrophys. J.* **702**, 1443.

Gadun, A.S., Hanslmeier, A., Pikalov, K.N.: 1997, Bisectors and line-parameter variations over granular and intergranular regions in 2-D artificial granulation. *Astron. Astrophys.* **320**, 1001.

Gingerich, O., Noyes, R.W., Kalkofen, W., Cuny, Y.: 1971, The Harvard-Smithsonian reference atmosphere. *Solar Phys.* **18**(3), 347. DOI.

González Manrique, S.J., Quintero Noda, C., Kuckein, C., Ruiz Cobo, B., Carlsson, M.: 2020, Capabilities of bisector analysis of the Si I 10 827 Å line for estimating line-of-sight velocities in the quiet Sun. *Astron. Astrophys.* **634**, A19. DOI.

Goode, P.R., Yurchyshyn, V., Cao, W., Abramenko, V., Andic, A., Ahn, K., Chae, J.: 2010, Highest Resolution Observations of the Quietest Sun. *Astrophys. J. Lett.* **714**(1), L31. DOI.

Gošić, M., Bellot Rubio, L.R., Orozco Suárez, D., Katsukawa, Y., del Toro Iniesta, J.C.: 2014, The Solar Internetwork. I. Contribution to the Network Magnetic Flux. *Astrophys. J.* **797**(1), 49. DOI. ADS.

Grotrian, W.: 1939, Zur Frage der Deutung der Linien im Spektrum der Sonnenkorona. *Naturwissenschaften* **27**(13), 214. DOI.

Guglielmino, S.L., Martínez Pillet, V., Ruiz Cobo, B., Bellot Rubio, L.R., del Toro Iniesta, J.C., Solanki, S.K., Riethmüller, T.L., Zuccarello, F.: 2020, On the Magnetic Nature of an Exploding Granule as Revealed by Sunrise/IMaX. *Astrophys. J.* **896**(1), 62. DOI.

Hagenaar, H.J., Schrijver, C.J., Title, A.M.: 2003, The Properties of Small Magnetic Regions on the Solar Surface and the Implications for the Solar Dynamo(s). *Astrophys. J.* **584**, 1107.

Hanslmeier, A., Nesis, A., Mattig, W.: 1994, Dynamics of the solar granulation: bisector analysis. *Astron. Astrophys.* **288**, 960.

Hanslmeier, A., Kučera, A., Rybák, J., Wöhl, H.: 2008, Observation of Turbulence in Solar Surface Convection: I. Line Parameter Correlations. *Solar Phys.* **249**(2), 293. DOI.

He, K., Zhang, X., Ren, S., Sun, J.: 2015a, Deep residual learning for image recognition. *CoRR* **abs/1512.03385**.

He, K., Zhang, X., Ren, S., Sun, J.: 2015b, Delving deep into rectifiers: Surpassing human-level performance on imagenet classification. *CoRR* **abs/1502.01852**.

Hirzberger, J.: 2002, On the brightness and velocity structure of solar granulation. *Astron. Astrophys.* **392**, 1105.

Hirzberger, J., Vázquez, M., Bonet, J.A., Hanslmeier, A., Sobotka, M.: 1997, Time Series of Solar Granulation Images. I. Differences between Small and Large Granules in Quiet Regions. *Astrophys. J.* **480**, 406.

Hirzberger, J., Bonet, J.A., Vázquez, M., Hanslmeier, A.: 1999, Time Series of Solar Granulation Images. II. Evolution of Individual Granules. *Astrophys. J.* **515**, 441.

Hirzberger, J., Gizon, L., Solanki, S.K., Duvall, T.L.: 2008, Structure and Evolution of Supergranulation from Local Helioseismology. *Solar Phys.* **251**(1-2), 417. DOI.

Hollweg, J.V., Jackson, S., Galloway, D.: 1982, Alfven Waves in the Solar Atmospheres - Part Three - Nonlinear Waves on Open Flux Tubes. *Solar Phys.* **75**(1-2), 35. DOI.

Holweger, H., Kneer, F.: 1989, Spatially Resolved Spectra of Solar Granules. In: Rutten, R.J., Severino, G. (eds.) *Solar and Stellar Granulation*, *NATO Advanced Study Institute (ASI) Series C* **263**, 173.

Hotta, H., Rempel, M., Yokoyama, T.: 2016, Large-scale magnetic fields at high Reynolds numbers in magnetohydrodynamic simulations. *Science* **351**(6280), 1427. DOI.

Hu, J., Shen, L., Sun, G.: 2017, Squeeze-and-excitation networks. *CoRR* **abs/1709.01507**.

Hubeny, I., Mihalas, D.: 2014, *Theory of Stellar Atmospheres.*

Iijima, H., Yokoyama, T.: 2017, A Three-dimensional Magnetohydrodynamic Simulation of the Formation of Solar Chromospheric Jets with Twisted Magnetic Field Lines. *Astrophys. J.* **848**(1), 38. DOI.

Ioffe, S., Szegedy, C.: 2015, Batch normalization: Accelerating deep network training by reducing internal covariate shift. *CoRR* **abs/1502.03167**.

Ishikawa, R., Tsuneta, S., Ichimoto, K., Isobe, H., Katsukawa, Y., Lites, B.W., Nagata, S., Shimizu, T., Shine, R.A., Suematsu, Y., Tarbell, T.D., Title, A.M.: 2008, Transient horizontal magnetic fields in solar plage regions. *Astron. Astrophys.* **481**(1), L25. DOI.

Ishikawa, R., Trujillo Bueno, J., Uitenbroek, H., Kubo, M., Tsuneta, S., Goto, M., Kano, R., Narukage, N., Bando, T., Katsukawa, Y., Ishikawa, S., Giono, G., Suematsu, Y., Hara, H., Shimizu, T., Sakao, T., Winebarger, A., Kobayashi, K.,

Cirtain, J., Champey, P., Auchère, F., Štěpán, J., Belluzzi, L., Asensio Ramos, A., Manso Sainz, R., De Pontieu, B., Ichimoto, K., Carlsson, M., Casini, R.: 2017, Indication of the Hanle Effect by Comparing the Scattering Polarization Observed by CLASP in the Lyα and Si III 120.65 nm Lines. *Astrophys. J.* **841**(1), 31. DOI.

Janssen, K., Cauzzi, G.: 2006, Dynamics of the solar photosphere with IBIS. I. Reversed intensity structure in the mid-photosphere. *Astron. Astrophys.* **450**, 365.

Jess, D.B., Mathioudakis, M., Erdélyi, R., Crockett, P.J., Keenan, F.P., Christian, D.J.: 2009, Alfvén Waves in the Lower Solar Atmosphere. *Science* **323**(5921), 1582. DOI.

Jin, C., Wang, J., Zhao, M.: 2009, Vector Magnetic Fields of Solar Granulation. *Astrophys. J.* **690**, 279.

Judge, P.G., Kleint, L., Uitenbroek, H., Rempel, M., Suematsu, Y., Tsuneta, S.: 2015, Photon Mean Free Paths, Scattering, and Ever-Increasing Telescope Resolution. *Solar Phys.* **290**(3), 979. DOI.

Kanoh, R., Shimizu, T., Imada, S.: 2016, Hinode and IRIS Observations of the Magnetohydrodynamic Waves Propagating from the Photosphere to the Chromosphere in a Sunspot. *Astrophys. J.* **831**, 24.

Katsukawa, Y., Orozco Suárez, D.: 2012, Power Spectra of Velocities and Magnetic Fields on the Solar Surface and their Dependence on the Unsigned Magnetic Flux Density. *Astrophys. J.* **758**, 139.

Katsukawa, Y., del Toro Iniesta, J.C., Solanki, S.K., Kubo, M., Hara, H., Shimizu, T., Oba, T., Kawabata, Y., Tsuzuki, T., Uraguchi, F., Nodomi, Y., Shinoda, K., Tamura, T., Suematsu, Y., Ishikawa, R., Kano, R., Matsumoto, T., Ichimoto, K., Nagata, S., Quintero Noda, C., Anan, T., Orozco Suárez, D., Balaguer Jiménez, M., López Jiménez, A.C., Cobos Carrascosa, J.P., Feller, A., Riethmueller, T.,

Gandorfer, A., Lagg, A.: 2020, Sunrise Chromospheric Infrared SpectroPolarimeter (SCIP) for sunrise III: system design and capability. In: *Society of Photo-Optical Instrumentation Engineers (SPIE) Conference Series*, *Society of Photo-Optical Instrumentation Engineers (SPIE) Conference Series* **11447**, 114470Y. DOI.

Khomenko, E., Martínez Pillet, V., Solanki, S.K., del Toro Iniesta, J.C., Gandorfer, A., Bonet, J.A., Domingo, V., Schmidt, W., Barthol, P., Knölker, M.: 2010, Where the Granular Flows Bend. *Astrophys. J. Lett.* **723**, L159.

Kingma, D.P., Ba, J.: 2014, Adam: A Method for Stochastic Optimization. *arXiv e-prints*, arXiv:1412.6980. ADS.

Kitiashvili, I.N., Kosovichev, A.G., Mansour, N.N., Lele, S.K., Wray, A.A.: 2012, Vortex tubes of turbulent solar convection. *Physica Scripta* **86**(1), 018403. DOI.

Klimchuk, J.A.: 2006, On Solving the Coronal Heating Problem. *Solar Phys.* **234**(1), 41. DOI.

Kosugi, T., Matsuzaki, K., Sakao, T., Shimizu, T., Sone, Y., Tachikawa, S., Hashimoto, T., Minesugi, K., Ohnishi, A., Yamada, T., Tsuneta, S., Hara, H., Ichimoto, K., Suematsu, Y., Shimojo, M., Watanabe, T., Shimada, S., Davis, J.M., Hill, L.D., Owens, J.K., Title, A.M., Culhane, J.L., Harra, L.K., Doschek, G.A., Golub, L.: 2007, The Hinode (Solar-B) Mission: An Overview. *Solar Phys.* **243**, 3.

Landi Degl'Innocenti, E., Landi Degl'Innocenti, M.: 1977, Response function for magnetic lines. *Astron. Astrophys.* **56**, 111.

Landi Degl'Innocenti, E., Landi Degl'Innocenti, M.: 1985, On the solution of the radiative transfer equations for polarized radiation. *Solar Phys.* **97**, 239. DOI.

Lemmerer, B., Hanslmeier, A., Muthsam, H., Piantschitsch, I.: 2017, Dynamics of small-scale convective motions. *Astron. Astrophys.* **598**, A126.

Lites, B.W., Ichimoto, K.: 2013, The SP_PREP Data Preparation Package for the Hinode Spectro-Polarimeter. *Solar Phys.* **283**, 601.

Lites, B.W., Centeno, R., McIntosh, S.W.: 2014, The solar cycle dependence of the weak internetwork flux. *Pub. Astron. Soc. Japan* **66**, S4.

Lites, B.W., Kubo, M., Socas-Navarro, H., Berger, T., Frank, Z., Shine, R., Tarbell, T., Title, A., Ichimoto, K., Katsukawa, Y., Tsuneta, S., Suematsu, Y., Shimizu, T., Nagata, S.: 2008, The Horizontal Magnetic Flux of the Quiet-Sun Internetwork as Observed with the Hinode Spectro-Polarimeter. *Astrophys. J.* **672**(2), 1237. DOI.

Lites, B.W., Akin, D.L., Card, G., Cruz, T., Duncan, D.W., Edwards, C.G., Elmore, D.F., Hoffmann, C., Katsukawa, Y., Katz, N., Kubo, M., Ichimoto, K., Shimizu, T., Shine, R.A., Streander, K.V., Suematsu, A., Tarbell, T.D., Title, A.M., Tsuneta, S.: 2013, The Hinode Spectro-Polarimeter. *Solar Phys.* **283**, 579.

Löhner-Böttcher, J., Schmidt, W., Stief, F., Steinmetz, T., Holzwarth, R.: 2018, Convective blueshifts in the solar atmosphere. I. Absolute measurements with LARS of the spectral lines at 6302 Å. *Astron. Astrophys.* **611**, A4.

López Ariste, A., Martínez González, M.J., Ramírez Vélez, J.C.: 2007, Determination of field strengths in the quiet Sun. *Astron. Astrophys.* **464**(1), 351. DOI.

Louis, R.E., Ravindra, B., Georgoulis, M.K., Küker, M.: 2015, Analysing the Effects of Apodizing Windows on Local Correlation Tracking Using Nirvana Simulations of Convection. *Solar Phys.* **290**(4), 1135. DOI.

Malherbe, J.-M., Roudier, T., Stein, R., Frank, Z.: 2018, Dynamics of Trees of Fragmenting Granules in the Quiet Sun: Hinode/SOT Observations Compared to Numerical Simulation. *Solar Phys.* **293**(1), 4. DOI.

Martínez Pillet, V., Del Toro Iniesta, J.C., Álvarez-Herrero, A., Domingo, V., Bonet, J.A., González Fernández, L., López Jiménez, A., Pastor, C., Gasent Blesa, J.L.,

Mellado, P., Piqueras, J., Aparicio, B., Balaguer, M., Ballesteros, E., Belenguer, T., Bellot Rubio, L.R., Berkefeld, T., Collados, M., Deutsch, W., Feller, A., Girela, F., Grauf, B., Heredero, R.L., Herranz, M., Jerónimo, J.M., Laguna, H., Meller, R., Menéndez, M., Morales, R., Orozco Suárez, D., Ramos, G., Reina, M., Ramos, J.L., Rodríguez, P., Sánchez, A., Uribe-Patarroyo, N., Barthol, P., Gandorfer, A., Knoelker, M., Schmidt, W., Solanki, S.K., Vargas Domínguez, S.: 2011, The Imaging Magnetograph eXperiment (IMaX) for the Sunrise Balloon-Borne Solar Observatory. *Solar Phys.* **268**, 57.

Masada, Y., Sano, T.: 2016, Spontaneous Formation of Surface Magnetic Structure from Large-scale Dynamo in Strongly Stratified Convection. *Astrophys. J. Lett.* **822**(2), L22. DOI.

Matsumoto, T., Kitai, R.: 2010, Temporal Power Spectra of the Horizontal Velocity of the Solar Photosphere. *Astrophys. J. Lett.* **716**(1), L19. DOI.

Moll, R., Cameron, R.H., Schüssler, M.: 2011, Vortices in simulations of solar surface convection. *Astron. Astrophys.* **533**, A126. DOI.

Morton, R.J., Erdélyi, R., Jess, D.B., Mathioudakis, M.: 2011, Observations of Sausage Modes in Magnetic Pores. *Astrophys. J. Lett.* **729**(2), L18. DOI.

Müller, D.A.N., Steiner, O., Schlichenmaier, R., Brandt, P.N.: 2001, Time-slice diagrams of solar granulation. *Solar Phys.* **203**(2), 211. DOI.

Nesis, A., Bogdan, T.J., Cattaneo, F., Hanslmeier, A., Knoelker, M., Malagoli, A.: 1992, Evidence for Transonic Flows in the Solar Granulation. *Astrophys. J. Lett.* **399**, L99. DOI.

Nesis, A., Hanslmeier, A., Hammer, R., Komm, R., Mattig, W., Staiger, J.: 1993, Dynamics of the solar granulation. *Astron. Astrophys.* **279**, 599.

Nesis, A., Hammer, R., Roth, M., Schleicher, H.: 2001, Dynamics of the solar granulation. VII. A nonlinear approach. *Astron. Astrophys.* **373**, 307.

Nordlund, Å., Stein, R.F., Asplund, M.: 2009, Solar Surface Convection. *Living Reviews in Solar Physics* **6**, 2.

Nordlund, A., Spruit, H.C., Ludwig, H.-G., Trampedach, R.: 1997, Is stellar granulation turbulence? *Astron. Astrophys.* **328**, 229.

November, L.J., Simon, G.W.: 1988, Precise Proper-Motion Measurement of Solar Granulation. *Astrophys. J.* **333**, 427. DOI.

Oba, T., Iida, Y., Shimizu, T.: 2017, Height-dependent Velocity Structure of Photospheric Convection in Granules and Intergranular Lanes with Hinode/SOT. *Astrophys. J.* **836**, 40.

Oba, T., Iida, Y., Shimizu, T.: 2020, Average Radial Structures of Gas Convection in the Solar Granulation. *Astrophys. J.* **890**(2), 141. DOI. ADS.

Oba, T., Riethmüller, T.L., Solanki, S.K., Iida, Y., Quintero Noda, C., Shimizu, T.: 2017, The Small-scale Structure of Photospheric Convection Retrieved by a Deconvolution Technique Applied to Hinode/SP Data. *Astrophys. J.* **849**, 7.

Obukhov, A.M.: 1959, On the influence of hydrostatic forces on the structure of the temperature field in turbulent flow. *Dokl. Akad. Nauk. SSR* **125**, 1246.

Okamoto, T.J., De Pontieu, B.: 2011, Propagating Waves Along Spicules. *Astrophys. J. Lett.* **736**, L24.

Okamoto, T.J., Antolin, P., De Pontieu, B., Uitenbroek, H., Van Doorsselaere, T., Yokoyama, T.: 2015, Resonant Absorption of Transverse Oscillations and Associated Heating in a Solar Prominence. I. Observational Aspects. *Astrophys. J.* **809**, 71.

Parnell, C.E.: 2002, Nature of the magnetic carpet - I. Distribution of magnetic fluxes. *Mon. Not. Roy. Astron. Soc.* **335**(2), 389. DOI.

Petrovay, K., Szakaly, G.: 1993, The origin of intranetwork fields: a small-scale solar dynamo. *Astron. Astrophys.* **274**, 543.

Quintero Noda, C., Ruiz Cobo, B., Orozco Suárez, D.: 2014, Photospheric downward plasma motions in the quiet Sun. *Astron. Astrophys.* **566**, A139. DOI.

Quintero Noda, C., Borrero, J.M., Orozco Suárez, D., Ruiz Cobo, B.: 2014, High speed magnetized flows in the quiet Sun. *Astron. Astrophys.* **569**, A73. DOI.

Rast, M.P.: 1998, Compressible plume dynamics and stability. *Journal of Fluid Mechanics* **369**(1), 125. DOI.

Rast, M.P., Bello González, N., Bellot Rubio, L., Cao, W., Cauzzi, G., Deluca, E., de Pontieu, B., Fletcher, L., Gibson, S.E., Judge, P.G., Katsukawa, Y., Kazachenko, M.D., Khomenko, E., Landi, E., Martínez Pillet, V., Petrie, G.J.D., Qiu, J., Rachmeler, L.A., Rempel, M., Schmidt, W., Scullion, E., Sun, X., Welsch, B.T., Andretta, V., Antolin, P., Ayres, T.R., Balasubramaniam, K.S., Ballai, I., Berger, T.E., Bradshaw, S.J., Campbell, R.J., Carlsson, M., Casini, R., Centeno, R., Cranmer, S.R., Criscuoli, S., Deforest, C., Deng, Y., Erdélyi, R., Fedun, V., Fischer, C.E., González Manrique, S.J., Hahn, M., Harra, L., Henriques, V.M.J., Hurlburt, N.E., Jaeggli, S., Jafarzadeh, S., Jain, R., Jefferies, S.M., Keys, P.H., Kowalski, A.F., Kuckein, C., Kuhn, J.R., Kuridze, D., Liu, J., Liu, W., Longcope, D., Mathioudakis, M., McAteer, R.T.J., McIntosh, S.W., McKenzie, D.E., Miralles, M.P., Morton, R.J., Muglach, K., Nelson, C.J., Panesar, N.K., Parenti, S., Parnell, C.E., Poduval, B., Reardon, K.P., Reep, J.W., Schad, T.A., Schmit, D., Sharma, R., Socas-Navarro, H., Srivastava, A.K., Sterling, A.C., Suematsu, Y., Tarr, L.A., Tiwari, S., Tritschler, A., Verth, G., Vourlidas, A., Wang, H., Wang, Y.-M., NSO and DKIST Project, DKIST Instrument Scientists, DKIST Science Working Group, DKIST Critical Science Plan Community: 2021, Critical Science Plan for the Daniel K. Inouye Solar Telescope (DKIST). *Solar Phys.* **296**(4), 70. DOI.

Rempel, M.: 2014, Numerical Simulations of Quiet Sun Magnetism: On the Contribution from a Small-scale Dynamo. *Astrophys. J.* **789**, 132.

Rempel, M.: 2018, Small-scale Dynamo Simulations: Magnetic Field Amplification in Exploding Granules and the Role of Deep and Shallow Recirculation. *Astrophys. J.* **859**(2), 161. DOI.

Requerey, I.S., Cobo, B.R., Gošić, M., Bellot Rubio, L.R.: 2018, Persistent magnetic vortex flow at a supergranular vertex. *Astron. Astrophys.* **610**, A84. DOI.

Riethmüller, T.L., Solanki, S.K., Berdyugina, S.V., Schüssler, M., Martínez Pillet, V., Feller, A., Gandorfer, A., Hirzberger, J.: 2014, Comparison of solar photospheric bright points between Sunrise observations and MHD simulations. *Astron. Astrophys.* **568**, A13. DOI.

Rieutord, M., Rincon, F.: 2010, The Sun's Supergranulation. *Living Reviews in Solar Physics* **7**(1), 2. DOI.

Rieutord, M., Roudier, T., Rincon, F., Malherbe, J.-M., Meunier, N., Berger, T., Frank, Z.: 2010, On the power spectrum of solar surface flows. *Astron. Astrophys.* **512**, A4. DOI.

Rimmele, T.R., Warner, M., Keil, S.L., Goode, P.R., Knölker, M., Kuhn, J.R., Rosner, R.R., McMullin, J.P., Casini, R., Lin, H., Wöger, F., von der Lühe, O., Tritschler, A., Davey, A., de Wijn, A., Elmore, D.F., Fehlmann, A., Harrington, D.M., Jaeggli, S.A., Rast, M.P., Schad, T.A., Schmidt, W., Mathioudakis, M., Mickey, D.L., Anan, T., Beck, C., Marshall, H.K., Jeffers, P.F., Oschmann, J.M., Beard, A., Berst, D.C., Cowan, B.A., Craig, S.C., Cross, E., Cummings, B.K., Donnelly, C., de Vanssay, J.-B., Eigenbrot, A.D., Ferayorni, A., Foster, C., Galapon, C.A., Gedrites, C., Gonzales, K., Goodrich, B.D., Gregory, B.S., Guzman, S.S., Guzzo, S., Hegwer, S., Hubbard, R.P., Hubbard, J.R., Johansson, E.M., Johnson, L.C., Liang, C., Liang, M., McQuillen, I., Mayer, C., Newman, K., Onodera, B., Phelps, L., Puentes, M.M., Richards, C., Rimmele, L.M., Sekulic, P., Shimko, S.R., Simison, B.E., Smith, B., Starman, E., Sueoka, S.R., Summers, R.T., Szabo, A., Szabo, L., Wampler, S.B., Williams, T.R., White, C.: 2020, The

Daniel K. Inouye Solar Telescope - Observatory Overview. *Solar Phys.* **295**(12), 172. DOI.

Rincon, F.: 2007, Theories of convection and the spectrum of turbulence in the solar photosphere. In: Kupka, F., Roxburgh, I., Chan, K.L. (eds.) *Convection in Astrophysics* **239**, 58. DOI.

Roudier, T., Muller, R.: 1986, Structure of the solar granulation. *Solar Phys.* **107**(1), 11. DOI.

Roudier, T., Lignières, F., Rieutord, M., Brandt, P.N., Malherbe, J.M.: 2003, Families of fragmenting granules and their relation to meso- and supergranular flow fields. *Astron. Astrophys.* **409**, 299. DOI.

Ruiz Cobo, B., del Toro Iniesta, J.C.: 1992, Inversion of Stokes profiles. *Astrophys. J.* **398**, 375.

Ruiz Cobo, B., del Toro Iniesta, J.C.: 1994, On the sensitivity of Stokes profiles to physical quantities. *Astron. Astrophys.* **283**, 129.

Rybák, J., Wöhl, H., Kučera, A., Hanslmeier, A., Steiner, O.: 2004, Indications of shock waves in the solar photosphere. *Astron. Astrophys.* **420**, 1141. DOI.

Sanchez Almeida, J.: 1992, Radiative transfer for polarized light: Equivalence between Stokes parameters and coherency matrix formalisms. *Solar Phys.* **137**(1), 1. DOI.

Shelyag, S., Keys, P., Mathioudakis, M., Keenan, F.P.: 2011, Vorticity in the solar photosphere. *Astron. Astrophys.* **526**, A5.

Shetye, J., Verwichte, E., Stangalini, M., Doyle, J.G.: 2021, The Nature of High-frequency Oscillations Associated with Short-lived Spicule-type Events. *Astrophys. J.* **921**(1), 30. DOI.

Shibata, K., Nakamura, T., Matsumoto, T., Otsuji, K., Okamoto, T.J., Nishizuka, N., Kawate, T., Watanabe, H., Nagata, S., UeNo, S., Kitai, R., Nozawa, S., Tsuneta, S., Suematsu, Y., Ichimoto, K., Shimizu, T., Katsukawa, Y., Tarbell, T.D., Berger, T.E., Lites, B.W., Shine, R.A., Title, A.M.: 2007, Chromospheric Anemone Jets as Evidence of Ubiquitous Reconnection. *Science* **318**(5856), 1591. DOI.

Shimizu, T., Nagata, S., Tsuneta, S., Tarbell, T., Edwards, C., Shine, R., Hoffmann, C., Thomas, E., Sour, S., Rehse, R., Ito, O., Kashiwagi, Y., Tabata, M., Kodeki, K., Nagase, M., Matsuzaki, K., Kobayashi, K., Ichimoto, K., Suematsu, Y.: 2008, Image Stabilization System for Hinode (Solar-B) Solar Optical Telescope. *Solar Phys.* **249**(2), 221. DOI.

Socas-Navarro, H.: 2011, A high-resolution three-dimensional model of the solar photosphere derived from Hinode observations. *Astron. Astrophys.* **529**, A37. DOI.

Solanki, S.K., Rueedi, I., Bianda, M., Steffen, M.: 1996, On the detection of shocks in the solar granulation. *Astron. Astrophys.* **308**, 623.

Solanki, S.K., Barthol, P., Danilovic, S., Feller, A., Gandorfer, A., Hirzberger, J., Riethmüller, T.L., Schüssler, M., Bonet, J.A., Martínez Pillet, V., del Toro Iniesta, J.C., Domingo, V., Palacios, J., Knölker, M., Bello González, N., Berkefeld, T., Franz, M., Schmidt, W., Title, A.M.: 2010, SUNRISE: Instrument, Mission, Data, and First Results. *Astrophys. J. Lett.* **723**, L127.

Spruit, H.C.: 1981, Motion of magnetic flux tubes in the solar convection zone and chromosphere. *Astron. Astrophys.* **98**, 155.

Srivastava, A.K., Shetye, J., Murawski, K., Doyle, J.G., Stangalini, M., Scullion, E., Ray, T., Wójcik, D.P., Dwivedi, B.N.: 2017, High-frequency torsional Alfvén waves as an energy source for coronal heating. *Scientific Reports* **7**, 43147. DOI.

Steffen, M., Caffau, E., Ludwig, H.-G.: 2013, Micro- and macroturbulence predictions from CO5BOLD 3D stellar atmospheres . *Memorie della Societa Astronomica Italiana Supplementi* **24**, 37.

Stein, R.F., Nordlund, Å.: 1998, Simulations of Solar Granulation. I. General Properties. *Astrophys. J.* **499**, 914.

Steiner, O., Franz, M., Bello González, N., Nutto, C., Rezaei, R., Martínez Pillet, V., Bonet Navarro, J.A., del Toro Iniesta, J.C., Domingo, V., Solanki, S.K., Knölker, M., Schmidt, W., Barthol, P., Gandorfer, A.: 2010, Detection of Vortex Tubes in Solar Granulation from Observations with SUNRISE. *Astrophys. J. Lett.* **723**(2), L180. DOI.

Suematsu, Y., Tsuneta, S., Ichimoto, K., Shimizu, T., Otsubo, M., Katsukawa, Y., Nakagiri, M., Noguchi, M., Tamura, T., Kato, Y., Hara, H., Kubo, M., Mikami, I., Saito, H., Matsushita, T., Kawaguchi, N., Nakaoji, T., Nagae, K., Shimada, S., Takeyama, N., Yamamuro, T.: 2008, The Solar Optical Telescope of Solar-B (Hinode): The Optical Telescope Assembly. *Solar Phys.* **249**(2), 197. DOI.

Szegedy, C., Liu, W., Jia, Y., Sermanet, P., Reed, S., Anguelov, D., Erhan, D., Vanhoucke, V., Rabinovich, A.: 2014, Going Deeper with Convolutions. *arXiv e-prints*, arXiv:1409.4842. ADS.

Tomczyk, S., McIntosh, S.W., Keil, S.L., Judge, P.G., Schad, T., Seeley, D.H., Edmondson, J.: 2007, Alfvén Waves in the Solar Corona. *Science* **317**, 1192.

Toriumi, S., Katsukawa, Y., Cheung, M.C.M.: 2017, Various Local Heating Events in the Earliest Phase of Flux Emergence. *Astrophys. J.* **836**(1), 63. DOI.

Tremblay, B., Attie, R.: 2020, Inferring Plasma Flows at Granular and Supergranular Scales with a New Architecture for the DeepVel Neural Network. *Frontiers in Astronomy and Space Sciences* **7**, 25. DOI.

Tremblay, B., Roudier, T., Rieutord, M., Vincent, A.: 2018, Reconstruction of Horizontal Plasma Motions at the Photosphere from Intensitygrams: A Comparison Between DeepVel, LCT, FLCT, and CST. *Solar Phys.* **293**(4), 57. DOI.

Tremblay, B., Cossette, J.-F., Kazachenko, M.D., Charbonneau, P., Vincent, A.: 2021a, Inferring depth-dependent plasma motions from surface observations using the DeepVel neural network. *Journal of Space Weather and Space Climate* **11**, 9. DOI.

Tremblay, B., Reardon, K., Attié, R., Kazachenko, M., Asensio Ramos, A., Tilipman, D.: 2021b, Inferring Plasma Flows in the Solar Photosphere & Chromosphere using Deep Learning and Surface Observations. In: *The 20.5th Cambridge Workshop on Cool Stars, Stellar Systems, and the Sun (CS20.5)*, *Cambridge Workshop on Cool Stars, Stellar Systems, and the Sun*, 204. DOI.

Trujillo Bueno, J., Shchukina, N., Asensio Ramos, A.: 2004, A substantial amount of hidden magnetic energy in the quiet Sun. *Nature* **430**(6997), 326. DOI.

Trujillo Bueno, J., Štěpán, J., Casini, R.: 2011, The Hanle Effect of the Hydrogen Lyα Line for Probing the Magnetism of the Solar Transition Region. *Astrophys. J. Lett.* **738**(1), L11. DOI.

Tsuneta, S., Ichimoto, K., Katsukawa, Y., Nagata, S., Otsubo, M., Shimizu, T., Suematsu, Y., Nakagiri, M., Noguchi, M., Tarbell, T., Title, A., Shine, R., Rosenberg, W., Hoffmann, C., Jurcevich, B., Kushner, G., Levay, M., Lites, B., Elmore, D., Matsushita, T., Kawaguchi, N., Saito, H., Mikami, I., Hill, L.D., Owens, J.K.: 2008, The Solar Optical Telescope for the Hinode Mission: An Overview. *Solar Phys.* **249**, 167.

Utz, D., Hanslmeier, A., Muller, R., Veronig, A., Rybák, J., Muthsam, H.: 2010, Dynamics of isolated magnetic bright points derived from Hinode/SOT G-band observations. *Astron. Astrophys.* **511**, A39. DOI.

van Ballegooijen, A.A., Asgari-Targhi, M., Cranmer, S.R., DeLuca, E.E.: 2011, Heating of the Solar Chromosphere and Corona by Alfvén Wave Turbulence. *Astrophys. J.* **736**(1), 3. DOI.

Van Doorsselaere, T., Srivastava, A.K., Antolin, P., Magyar, N., Vasheghani Farahani, S., Tian, H., Kolotkov, D., Ofman, L., Guo, M., Arregui, I., De Moortel, I., Pascoe, D.: 2020, Coronal Heating by MHD Waves. *Space Sci. Rev.* **216**(8), 140. DOI.

Van Kooten, S.J., Cranmer, S.R.: 2017, Characterizing the Motion of Solar Magnetic Bright Points at High Resolution. *Astrophys. J.* **850**(1), 64. DOI.

Vargas Domínguez, S., Palacios, J., Balmaceda, L., Cabello, I., Domingo, V.: 2011, Spatial distribution and statistical properties of small-scale convective vortex-like motions in a quiet-Sun region. *Mon. Not. Roy. Astron. Soc.* **416**(1), 148. DOI.

Verma, M., Steffen, M., Denker, C.: 2013, Evaluating local correlation tracking using CO5BOLD simulations of solar granulation. *Astron. Astrophys.* **555**, A136. DOI.

Vernazza, J.E., Avrett, E.H., Loeser, R.: 1981, Structure of the solar chromosphere. III - Models of the EUV brightness components of the quiet-sun. *Astrophys. J. Supplement Series* **45**, 635.

Vitas, N., Fischer, C.E., Vögler, A., Keller, C.U.: 2011, Fast horizontal flows in a quiet sun MHD simulation and their spectroscopic signatures. *Astron. Astrophys.* **532**, A110. DOI.

Vögler, A., Shelyag, S., Schüssler, M., Cattaneo, F., Emonet, T., Linde, T.: 2005, Simulations of magneto-convection in the solar photosphere. Equations, methods, and results of the MURaM code. *Astron. Astrophys.* **429**, 335.

Wallace, L., Hinkle, K., Livingston, W.: 1998, *An atlas of the spectrum of the solar photosphere from 13,500 to 28,000 cm-1 (3570 to 7405 A).*

Wedemeyer-Böhm, S.: 2010, Small-scale structure and dynamics of the chromospheric magnetic field. *Mem. Societa Astronomica Italiana* **81**, 693.

Wedemeyer-Böhm, S., Rouppe van der Voort, L.: 2009, Small-scale swirl events in the quiet Sun chromosphere. *Astron. Astrophys.* **507**, L9.

Wilson, A., Maskelyne, N.: 1774, Observations on the Solar Spots. By Alexander Wilson, M. D. Professor of Practical Astronomy in the University of Glasgow. Communicated by the Rev. Nevil Maskelyne, Astronomer Royal. *Philosophical Transactions of the Royal Society of London Series I* **64**, 1.

Yadav, N., Cameron, R.H., Solanki, S.K.: 2021, Vortex flow properties in simulations of solar plage region: Evidence for their role in chromospheric heating. *Astron. Astrophys.* **645**, A3. DOI.

Yelles Chaouche, L., Moreno-Insertis, F., Bonet, J.A.: 2014, The power spectrum of solar convection flows from high-resolution observations and 3D simulations. *Astron. Astrophys.* **563**, A93. DOI.

Yokoi, N., Masada, Y., Takiwaki, T.: 2021, Modelling stellar convective transport with plumes: I. Non-equilibrium turbulence effect in double-averaging formulation. *arXiv e-prints*, arXiv:2111.08921. ADS.

Yu, D., Xie, Z., Hu, Q., Yang, S., Jin, C.: 2011, Properties of Granules in Upflows and Downflows. *Solar Phys.* **273**, 1.